

Hydrocarbons in interstellar ice analogues

UV-vis spectroscopy
and
VUV photochemistry

Hydrocarbons in interstellar ice analogues

UV-vis spectroscopy
and
VUV photochemistry

Proefschrift

ter verkrijging van
de graad van Doctor aan de Universiteit Leiden,
op gezag van de Rector Magnificus Prof. mr. C.J.J.M. Stolker,
volgens besluit van het College voor Promoties
te verdedigen op donderdag 29 januari 2015
klokke 11.15 uur

door

Steven Hendrik Cuyllé

geboren te Oostende, België
in 1983

Promotiecommissie

Promotor: Prof. dr. H. V. J. Linnartz
Overige leden: Prof. dr. H. Röttgering
Prof. dr. G. Strazzulla
Prof. dr. A. G. G. M. Tielens
Dr. J. Bouwman
Dr. C. Jäger

Voor de Fanclub

	Page
Chapter 1. Introduction	1
1.1 Carbon and the universe	1
1.2 Many carbonaceous molecules	4
1.2.1 Linear carbon molecules	4
1.2.2 Polycyclic aromatic hydrocarbons	4
1.2.3 Fullerenes	5
1.2.4 Amorphous carbon	5
1.2.5 Aminoacids	5
1.3 Interstellar ice	6
1.3.1 Stellar evolution and interstellar ice	6
1.3.2 Identification of molecules in space	7
1.3.3 Solid state molecules	9
1.4 Astrochemistry	10
1.4.1 Laboratory astrochemistry	11
1.4.2 Observations	11
1.4.3 Astrochemical modelling	11
1.4.4 The astrochemical triangle	11
1.5 This study	12
Chapter 2. OASIS: optical absorption setup for ice spectroscopy	15
2.1 Experimental details	16
2.2 Results	19
Chapter 3. A straightforward method for vacuum–UV flux measurements	23
3.1 Introduction	24
3.2 Experimental Setup	25
3.3 Method and verification	28
3.4 Verification	30
3.5 Conclusions	31
Chapter 4. UV-vis spectroscopy of C₆₀ embedded in water ice	33
4.1 Introduction	34
4.2 Experiment	36
4.3 Results	36
4.4 Assignments	41
4.5 Astrophysical considerations	42
Chapter 5. Lyman-α induced charge effects of PAHs	45
5.1 Introduction	46

5.2	Experimental	47
5.3	Results	47
5.3.1	PAH:NH ₃ Ly- α photolysis	47
5.3.2	PAH:H ₂ O/NH ₃ UV photolysis	51
5.3.3	Reaction products	51
5.4	Discussion	53
5.4.1	NH ₃ ice chemical process	53
5.4.2	Ammonia vs. Water Ice	56
5.4.3	Astrophysical Implications	57
Chapter 6. Photochemistry of PAHs in cosmic water ice		59
6.1	Introduction	60
6.2	Experimental method	62
6.2.1	Controlling PAH concentration	64
6.3	Results	67
6.3.1	Coronene	67
6.3.2	Pyrene	72
6.3.3	Ionization efficiency	72
6.4	Discussion	74
6.4.1	Low concentration regime (PAH:H ₂ O < 1:1 000)	75
6.4.2	High concentration regime (PAH:H ₂ O > 1:1 000)	76
6.5	Astrophysical implications	76
6.6	Conclusions	78
Chapter 7. VUV photochemistry of solid acetylene: a multispectral approach		81
7.1	Introduction	82
7.2	Experimental	83
7.2.1	OASIS	84
7.2.2	The FTIR HV setup	85
7.2.3	C ₂ H ₂ matrix material	85
7.3	Results and discussion	86
7.3.1	Ar:C ₂ H ₂ results	87
7.3.2	Pure C ₂ H ₂ results	87
7.3.3	C ₂ H ₂ :H ₂ O results	95
7.3.4	Discussion	98
7.4	Astrophysical implications	99
7.5	Conclusions	100
Bibliography		103
Samenvatting		112
Curriculum vitae		117
Nawoord		119

Chapter 1

Introduction

1.1 Carbon and the universe

At the beginning of the universe, just after the big bang, temperatures were so high that no matter existed. However, the fast expansion of the universe caused a rapid drop in temperature allowing atomic nuclei to appear after about 3 minutes. The dominant atomic species in the early days of the universe were the three lightest elements of the periodic table: Hydrogen, Helium and a lesser amount of Lithium and their isotopes such as deuterium and helium 3. Many thousands of years later, the first chemical reactions were very restricted and only small molecules, simple di- and triatomics - H_2 , HD, H_2^+ , HeH^+ , HD^+ , H_3^+ , LiH, and H_2D^+ - formed. Heavier elements were lacking and only came into play after they formed in nuclear fusion processes in stars. Once such a star reached the end of its lifetime, a catastrophic event resulted in enrichment of the interstellar medium with heavier elements (comprising carbon).

Carbon is expected to play a vital chemical role in the universe (Henning & Salama 1998; Tielens 2013), as it can form four chemical bonds resulting in both linear molecules (e.g. polyynes, alkanes, aminoacids), aromatic molecules (e.g. graphene, polycyclic aromatic hydrocarbons (PAHs)) and 3D molecular structures (e.g. fullerenes, nanotubes). This versatility is confirmed by the detection of many of the aforementioned examples in the interstellar medium, as a species, or as a class. From the 185 molecular species identified in the interstellar medium at the time of writing (2014), 137 are carbon-bearing species (Table 1.3), moreover, all identified species with 6 or more atoms are carbon-bearing species.

Most of these detections are from the gas phase spectra although this does not exclude the enrichment with molecules formed in interstellar ices and subsequently evaporated (Modica & Palumbo 2010; Palumbo et al. 2008b). In dark cold clouds, molecules condense and form ice mantles around dust grains providing a molecule reservoir that mainly consists of small volatile molecules (Boogert et al. 2008, 2011), but also of complex carbonaceous molecules (Keane et al. 2001). External triggers (e.g. UV photons, particle bombardment) can induce a very complex solid state chemistry that is fundamentally different from the gas phase. Moreover, scientists like Mayo Greenberg (Williams 2002) were convinced that life or at least the carbonaceous molecules that form the building blocks of life have been brought to earth on icy bodies (e.g. comets, planetoids) during the period of late heavy bombardment 3.8 - 4 billion years ago and provided a jump-start for the appearance of life.

Interestingly, when comparing the atomic composition of our galaxy (Croswell 1996, Table 1.1) to the atomic composition inside the human body (Emsley 1998, Table 1.2),

remarkable parallels appear. When ignoring the noble gases, the dominant species in both cases are oxygen, carbon and hydrogen. In our galaxy, oxygen is mainly present under small volatiles (O_2 , H_2O , CO , CO_2). In the human body, liquid water provides with the environment where the vital chemical reactions of life can take place. The 18.5 % by mass of carbon appears as the backbone of the organic molecules in every living organism (e.g. aminoacids, DNA, lipids). Tracking the formation and destruction of carbonaceous molecules in interstellar ices and other prebiotic environments (e.g. comets, icy dust mantles, icy moons) is a critical requisite to understand the chemical formation and destruction of complex organic molecules and provides us with vital clues on the question of how life started.

Table 1.1 — Top ten most abundant atomic species in our galaxy, from Crowell (1996)

	Element	mass fraction ppm
1	Hydrogen	739 000
2	Helium	240 000
3	Oxygen	10 400
4	Carbon	4 600
5	Neon	1 340
6	Iron	1 090
7	Nitrogen	960
8	Silicon	650
9	Magnesium	580
10	Sulphur	440

Table 1.2 — Top ten most abundant atomic species in the human body, from Emsley (1998)

	Element	mass fraction %
1	Oxygen	65.0
2	Carbon	18.5
3	Hydrogen	9.5
4	Nitrogen	3.2
5	Calcium	1.5
6	Phosphor	1.0
7	Potassium	0.4
8	Sulfur	0.3
9	Natrium	0.2
10	Chlorine	0.2

1.2 Many carbonaceous molecules

With about 0.5 % of the galaxy consisting of carbon (Table 1.1), it is the 4th most abundant element in our galaxy after hydrogen, helium and oxygen. A significant amount of carbon is stored in small, volatile molecules (e.g. CO and CO₂ Boogert et al. 2008). 10-20 % of the cosmic carbon abundance is stored in PAHs, with substantial amounts stored in fullerenes, aliphatic carbon molecules and amorphous carbon (Snow & Witt 1995). Below is an overview of the types of carbonaceous molecules discussed in this thesis and where they appear.

1.2.1 Linear carbon molecules

Gas phase linear carbonaceous molecules have been identified in active galactic nuclei, carbon-rich protostellar objects, interstellar clouds and in the solar system on Titan. Acetylene (C₂H₂) is considered a vital precursor to these molecules both in the gas phase and in the solid state. See Chapter 7 for a study concerning VUV photochemistry of solid state C₂H₂.

Most of the identifications are cyanopolyynes (HC_nN), which have a significant dipole moment and are therefore conveniently identified through their transitions in the radio spectrum. Polyynes (H-(C≡C)_n-H) lack due to their symmetry a permanent dipole moment hampering their identification at radio wavelengths. However, Cernicharo et al. (2001) identified some of them through their IR emissions. Chapter 7 treats the formation of polyynes in the solid state.

1.2.2 Polycyclic aromatic hydrocarbons

PAHs consist of multiple aromatic rings fused together. The formation mechanism of PAHs is elaborated by Parker et al. (2012) and considers acetylene (C₂H₂) as a starting point. The addition of a second acetylene forms vinylacetylene (C₄H₄), a non-linear molecule and an important precursor to aromatics. The addition of a vinyl group (-CH=CH₂) to vinylacetylene closes the ring and forms benzene. In a similar way, by adding vinyl groups, the amount of rings is increased and the PAH is enlarged. This process is very similar to the formation of soot on earth.

In space, this process is thought to take place in the atmospheres of carbon-rich AGB stars although they are only detected in the next stages of stellar evolution (e.g. post-AGB carbon-rich stars and planetary nebulae) through their typical IR emission features at 3.3, 6.2, 7.7, 8.6 and 11.2 μm (Allamandola et al. 1989; Gillett et al. 1973). Extensive IR observational studies concluded these bands to be ubiquitous in the interstellar medium as well as other galaxies.

The observations are from environments where the local temperature does not allow for IR emissions, therefore, a non-thermal excitation mechanism is required. This mechanism can be found in the strong local UV field. When a UV photon is absorbed by a gas phase PAH molecule, the repetitive molecular structure of PAHs allows for an effective redistribution of the absorbed energy over the chemical bonds. This vibrational energy is subsequently emitted at the aforementioned wavelengths in the IR.

Although no individual identification is possible from the IR spectra, recent observations in combination with a database of PAH spectra allowed for the determination of

the spatial distribution of some PAH properties, such as ionization state, PAH size and hydrogenation (Boersma et al. 2013).

Interestingly, PAH IR emission features are lacking where molecules freeze onto dust grains suggesting they have become part of the interstellar ice mantles (Geers et al. 2009). This thesis studies VUV photochemistry of PAHs in an interstellar ice environment in Chapters 5 and 6.

1.2.3 Fullerenes

Fullerenes consist of carbon organized in a spherical shape and are amongst the most stable forms of carbon in the universe. They are typically a result of chemical reactions in a carbon-rich hydrogen-poor environment, such as in the hot dense envelope of evolved stars, but also as a result of UV photochemistry of graphene (Berné & Tielens 2012). C_{60} and C_{70} are identified through their gas phase IR emission spectra and are the largest molecules currently identified in the interstellar medium (Cami et al. 2010). Chapter 4 of this study is an example of UV-vis spectroscopy of C_{60} in an interstellar ice environment.

1.2.4 Amorphous carbon

When carbon is present in bulk structure (e.g. coal, charcoal), it is called amorphous carbon. The core of interstellar dust grains is, beside silicates, considered to be amorphous carbon. It consists of carbon present in all of the above forms similar to graphite and coal (Jäger et al. 1998). The presence of amorphous carbon is evidenced through its strong and wide absorption band around 217.5 nm, known as the UV bump (Henning & Salama 1998).

1.2.5 Aminoacids

Aminoacids are vital building blocks of life. They consist of a carbonaceous molecule with an acid and an amino group group attached on adjacent carbons ($R-CHNH_2-COOH$). VUV photochemistry of ammonia-containing interstellar ices results in the formation of a multitude of aminoacid species (Nuevo et al. 2008) and there is a tentative identification of glycine (NH_2-CH_2-COOH), the simplest aminoacid, in the samples collected by the stardust spaceprobe (Elsila et al. 2009). Only 22 aminoacid species are found in living organisms and interestingly, only left hand enantiomers found in all life. The production of non-racemic abundances of amino-acids is a vital unanswered question to the emergence of life, although using circularly polarized UV photons in the photochemistry is known to produce an enantiomeric excess (Williams 2002; Nuevo et al. 2007).

1.3 Interstellar ice

1.3.1 Stellar evolution and interstellar ice

The solar system was formed about 4.6 billion years ago from matter that originates from the debris from older stars. The sun, a low-mass star, will also reach the end of its life and, over about 5 billion years, eject its outer layers into the universe (Bizzarro 2014, and references therein). This cyclic event, is typical for all stars. Every stage in the evolution of a star has its specific physical properties and chemistry.

Low-mass star formation (Fig. 1.1) starts in a cloud in the diffuse interstellar medium (Bizzarro 2014; Evans 1999). This medium can be distorted by stellar wind or a shock-wave. This causes, through gravitational collapse, the formation of a denser region known as a dense cloud consisting of hydrogen, helium, dust and some larger molecules. The centre of this cloud is shielded from intense and destructive interstellar UV radiation. This shield allows for the survival of complex molecules formed. The temperatures inside the cloud gradually drop to cryogenic levels (~ 10 K) resulting in accretion of volatile molecules onto dust grains. Complex organic molecules (e.g. PAHs, fullerenes) are also expected to become embedded in the ice. When the density in the cloud reaches a sufficient level, the cloud core will collapse under its own gravity forming a protostellar core and the temperature in its centre will rise with increasing pressure. The increased pressure counteracts gravity and prevents the core from collapsing further. For further collapse, the protostellar core needs an effective cooling mechanism. It is here that molecules provide with a cooling mechanism. Through collisional excitation and radiative emission, the kinetic energy of the atoms and molecules in the core is converted to IR radiation that can leave the protostellar core and in this way cool the system. As the core collapse continues, the system loses angular momentum by expelling matter over the rotational poles of the system. This process occurs simultaneously with the formation of a protoplanetary disk of matter. The outside of this disk is energetically processed by the UV radiation of the newborn star resulting in UV photochemistry and heating. The inside of the disk, which is shielded from the radiation of the star, remains cold. The chemistry in this part of the disk is dominated by reactions in ice layers on dust grains. In the case of low-mass stars, the matter inside the disk will slowly coagulate and form a planetary system.

When the planetary system is formed, many small icy bodies (e.g. comets, asteroids, icy moons) remain orbiting the star. From observations in our own solar system, we know that ice is also abundant in small particles in the upper atmospheres of many planets and moons. All of these ices are being energetically processed by the UV photons from the star resulting in enrichment of these icy bodies with complex molecules. During its lifetime, the star will slowly increase in volume and brightness up to the point where the core of the star runs out of fusionable hydrogen. Here the star reaches the end of its lifetime on the main sequence of the Hertzsprung-Russell diagram. Eventually, due to the lack of fusion energy, the delicate balance between radiation pressure and gravity in its inside will be distorted, resulting in a catastrophic explosion. The star ejects its outer layers into the universe enriching the interstellar medium with new material.

When a high-mass star (> 4 solar masses) reaches the end of its lifetime, its end of life phase is called a supernova. In a short time, the star will briefly (a few weeks) outshine a galaxy and expel most of its matter to the universe at high velocity (up to 10 % of the speed of light). This drives a shockwave of expanding gas and dust through the interstellar medium.

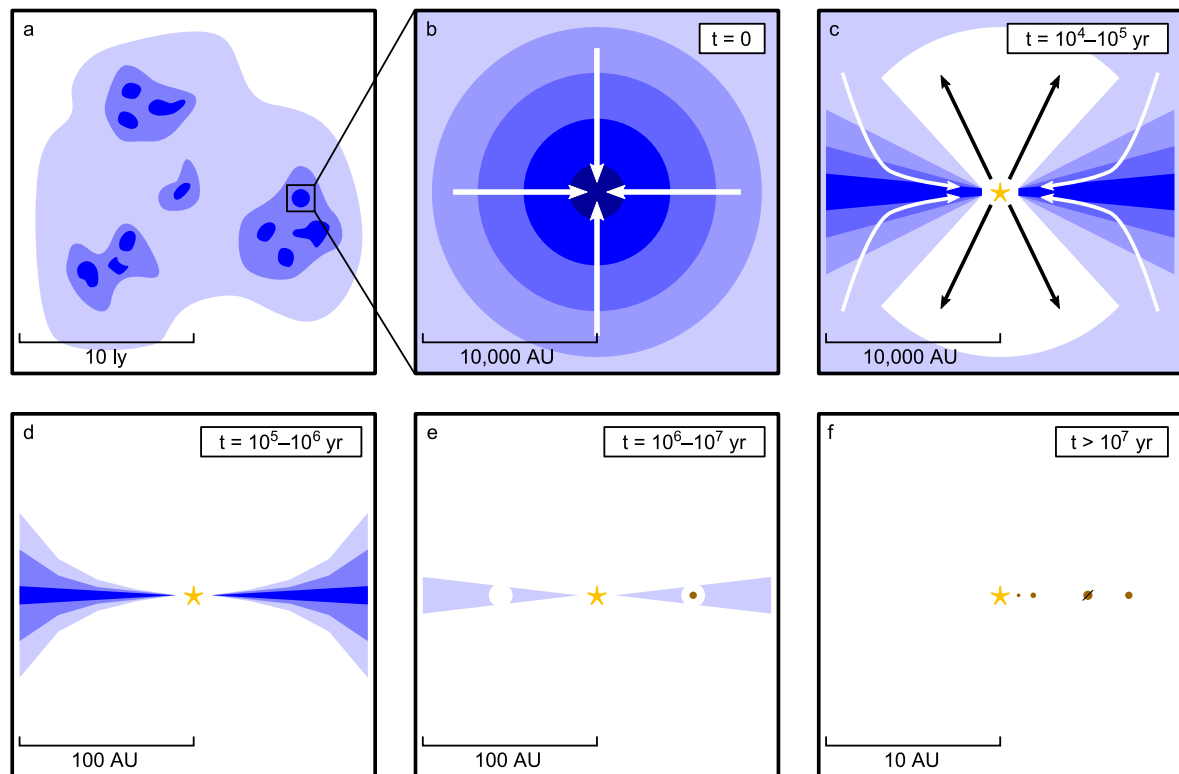


Figure 1.1 — Low-mass star formation, taken from Visser (2009).

1.3.2 Identification of molecules in space

The existence of interstellar matter has only been accepted by scientists after the development of photographic and spectroscopic techniques in the late 19th and early 20th century. The emergence of dark patches on early wide-field astronomical photographic plates or so-called “cavities” were initially attributed to the lack of stars in these regions. However, Barnard (1910) identified them as a result of interstellar gas and dust obscuring the stars behind.

At that moment, the nature of these interstellar clouds was still a mystery and new techniques were required to determine their composition. The application of the photographic technique to spectroscopy, as proposed by Draper (1879), allowed for the classification of stars according to composition and temperature, but also for the determination of the interstellar extinction due to interstellar matter (Trumpler 1930). When the technique was well refined, the applications of spectroscopy to astronomy caused a breakthrough in our understanding of the universe.

Until the detection of the first interstellar molecules, astronomers considered the very harsh interstellar UV radiation environment to be prohibitive to the formation of molecules. Nonetheless, the identification of CH, CN and CH⁺ in diffuse clouds by Swings & Rosenfeld (1937) evidenced the stability of molecules even in this very harsh environment. These on earth transient species also evidence the fundamentally different nature of interstellar chemistry from the conditions on earth. Since then, using a range of spectroscopic techniques, more than 180 molecular species have been identified in the interstellar medium. Most of these identifications are from (gas phase) rotational emission spectra at millimetre wavelengths where a flurry of very sharp lines with a very high level of uniqueness appear. As the intensities of the transitions in a rotational spectra are dependent on the molecule's temperature, this technique can also be used as a cosmic thermometer.

When a molecule does not possess a permanent electric dipole moment, which is typically the case for symmetric molecules (e.g. C₂H₂, CH₄, PAHs, fullerenes), or where the rotation is restrained (e.g. solid state), the molecule is radio-silent and the vibrational transitions in the IR are the main source of information and especially a versatile technique with respect to interstellar ice composition. However, overlap between different similar features (e.g. C-H stretch and O-H stretch) hampers identification of different molecules. Also, molecules with similar structure (e.g. PAHs) can be identified as a class, but due to the similarities in their chemical structure and by consequence their IR spectra, individual identifications are very challenging (Bouwman et al. 2011b).

Finally, the electronic transitions of the molecules fall in the UV-vis range of the electromagnetic spectrum, are often very strong, and are dependent on the electronic structure of the molecule. Therefore, UV-vis spectra offer more uniqueness than the IR, although in the case where a multitude of molecules are present, the spectra can become crowded. Larger molecules tend to have transitions to the longer wavelength with respect to small molecules of the same class. This property can be applied when carbonaceous molecules (e.g. PAHs, polyynes, fullerenes) are embedded in a solid state matrix, the difference in wavelength of the transitions of the PAH and the matrix allows for the identification of PAH transitions in the visible range, even when PAHs are present in very low concentrations, while the transitions of the matrix are further into the UV. Moreover, there is a distinction between the neutrals and their ions with the transitions of the ions shifted towards longer wavelengths. This unique property of UV-vis spectroscopy is extensively applied in this thesis as it allows for the detection and identification of very small concentrations (< 1:10 000) of PAHs or other complex organic molecules embedded in an interstellar ice matrix, a feat impossible to achieve in the IR due to band overlap and weaker transition strength. Moreover, this technique is very promising for the application to interstellar ice observations and the identification of solid-state carbonaceous molecules from which we know they are present embedded in ice (e.g. PAHs, fullerenes, polyynes). However, the environment of the molecule influences the spectra depending on temperature and ice environment. The solid state matrix environment is known to cause bands to shift with multiple nm and to broaden them. This requires UV-vis spectra to be measured in the right environment at the right temperature.

1.3.3 Solid state molecules

The dark nebulae observed by Barnard (1927) are made of of 100 nm to 1 micrometer-sized dust grains consisting of silicates or amorphous carbon. They feature a very strong absorption in the UV-vis region. When observing the same nebulae in the IR, the light from the stars behind the nebulae does shine through the nebula creating an excellent possibility of studying these nebulae through IR absorption spectroscopy (Figure 1.2). However, as a result of the absorbing nature of our atmosphere in the IR, mainly due to H₂O and CO₂, it is required to perform IR observations from above the atmospheric water or from outer space. The continuous improvement of IR detectors and other observational technologies in the last 60 years has enabled observations to improve drastically with every IR space telescope launched.

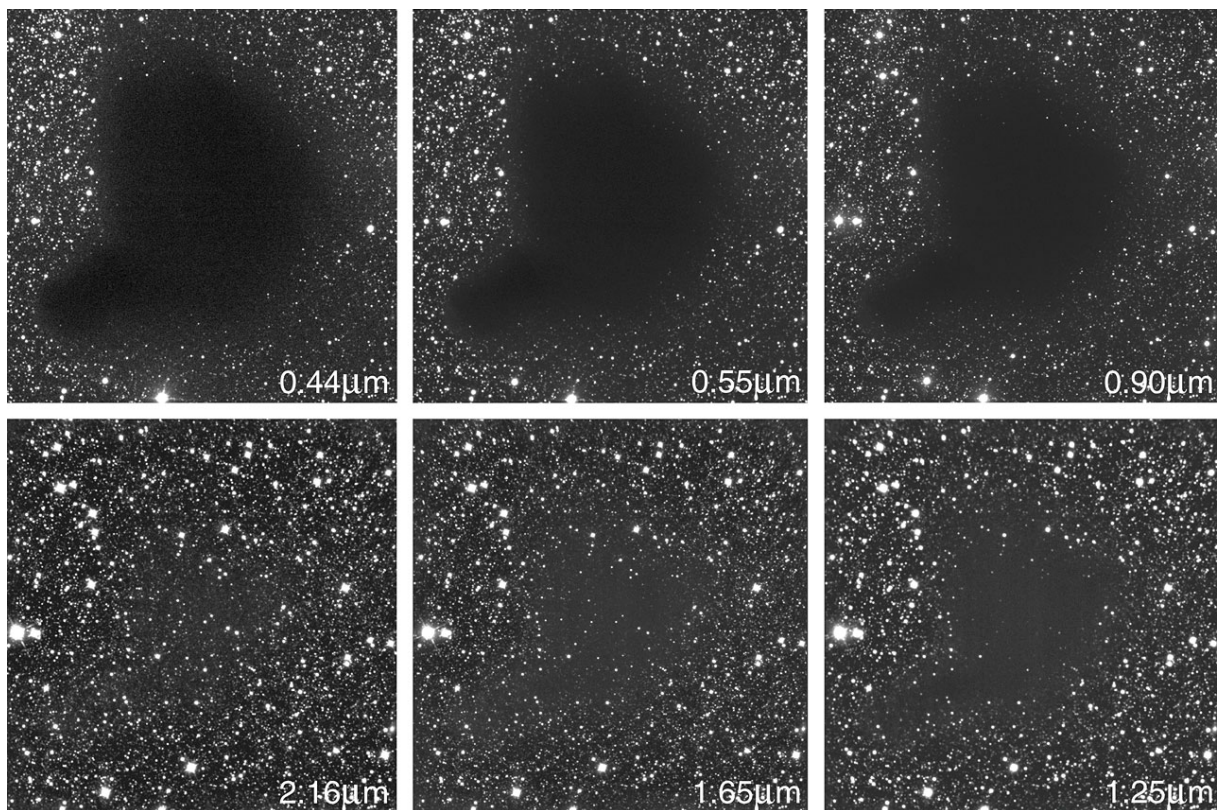


Figure 1.2 — The dark nebula Barnard 68, observed at different wavelengths from the visible to the IR. Note the difference in absorption with differing wavelength. (source: ESO)

Observations of interstellar ice has revealed that its composition is dominated by H₂O with smaller (variable) fractions of CO, CO₂, CH₄, CH₃OH, C₂H₂, NH₃ and others (Boogert et al. 2008), (Fig. 1.3). Larger molecules (e.g. PAHs, aminoacids, polyynes) are also expected to be part of interstellar ices (Geers et al. 2009) but their low concentrations in combination with lack of UV-vis observations have prevented detection and identification so far.

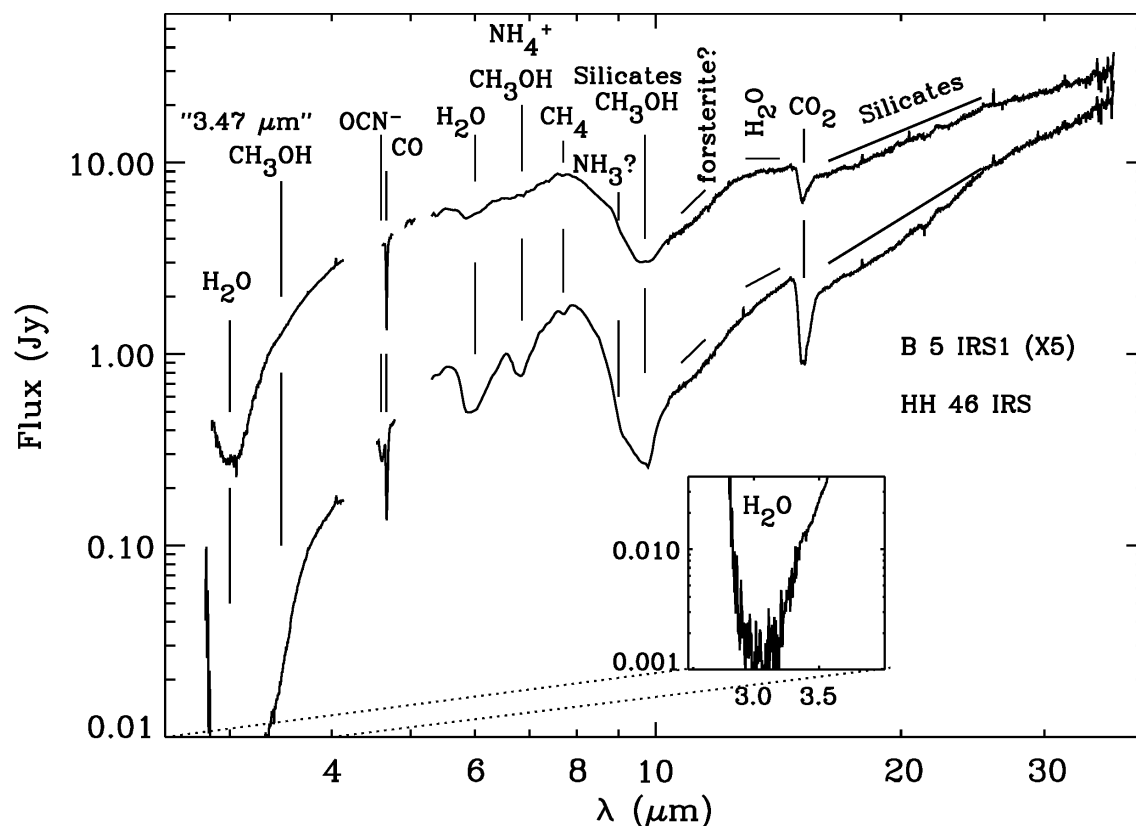


Figure 1.3 — From IR spectroscopy of interstellar ices, their composition is accurately derived. The spectra are dominated by H_2O , the dominant interstellar ice fraction. Adopted from Boogert et al. (2004)

The routes towards the formation of the main volatile species in interstellar ice are studied in detail by Tielens & Hagen (1982). They proposed a reaction network where all volatile species are being formed in the solid state except for CO, which is formed in the gas phase and condenses onto the ice. Solid state chemistry is required as many gas-phase chemical reactions require a third body to remove the excess energy resulting from the chemical reaction (Cuppen et al. 2010; Fuchs et al. 2009; Öberg et al. 2009, 2010; Romanzin et al. 2011). In our atmosphere, this occurs under three body collisions, however, due to the low density in the interstellar medium, three body collisions are very rare making many gas-phase reactions very slow in the interstellar medium. In the solid state, the dust grain acts as a third body able to remove the excess energy making many chemical reactions substantially more efficient in the solid state. This underlines the importance of solid state chemistry in stellar evolution.

1.4 Astrochemistry

The field of astrochemistry studies the abundances and chemical reactions of molecules in the universe and their influence on the evolution of the universe. The study consists of an overlap between a multitude of scientific disciplines (e.g. chemistry, astronomy, molecular physics, mathematics) and comprises three different aspects which have a very intimate interaction with each other (Fig. 1.4).

1.4.1 Laboratory astrochemistry

The aim of laboratory astrochemistry is to gain knowledge about interstellar and planetary chemistry by reproducing the circumstances in space as close as possible in the laboratory. It tries to create the same chemistry in the lab and observe the results taking into account the differences between the laboratory and the interstellar medium. In its strive to be as astrophysical relevant as possible, laboratory astrochemistry needs to be on the forefront of new developments in the fields of vacuum technology, optics, spectroscopy, laser technology and many more, often even pushing the envelope.

A lot of effort is needed in order to reproduce the extreme and diverse conditions of interstellar space. Pressures range from 10^{-15} mbar up to 0.1 mbar, temperatures range from 5 K to several thousands of K and time scales up to 10^7 years need to be simulated in a matter of hours or days. The local molecular composition is even more variable and these molecules are subject to energetic processing (e.g. UV photons, charged particle bombardment, X-ray photons, ...). Molecules can be present in the gas phase or in the solid state. In the lab, typically one aspect of this interstellar chemistry with specific boundary values is taken out and studied in all its details while the vital experimental variables are measured as accurate as necessary (and in many cases as accurate as technically possible). Gradually, the reaction scheme is expanded by adding more components to the chemistry aiming to understand the full reaction scheme as it occurs in the interstellar medium.

1.4.2 Observations

It is vital to link the findings from the laboratory studies to what is happening in the universe. Laboratory astrochemistry is therefore always a tight collaboration with observational astronomers. They observe the universe using the spectroscopic techniques mentioned above. From the spectra, they derive the molecular species and their abundances. It is here that the collaboration with the lab comes into play. Molecular spectra obtained in the lab are a necessary tool for an observational astrochemist. In the other direction, the unidentified lines in the spectra are the inspiration for laboratory research into the origin of these lines.

1.4.3 Astrochemical modelling

The third aspect of astrochemistry is the computational aspect. To understand the processes in the interstellar medium, mathematical models are made. These models require input from the observers with respect to physical and chemical conditions in the interstellar medium. Chemical processes are added from which the parameters (e.g. temperature-dependent reaction rates) have been measured after extensive laboratory work. The results of these models provide again with new information for observation suggestions and requests for chemical processes to be researched in the laboratory.

1.4.4 The astrochemical triangle

In order to gain new insights into the challenges of astrochemistry, advancements need to be made on all three aspects of astrochemistry and requires continuous interaction between them (Fig. 1.4). When one aspect is ahead of (or lagging) the other two, efforts

are required to close the gap. This thesis considers a laboratory study of carbonaceous molecules (e.g. PAHs, polyynes) embedded in an interstellar ice environment. Although from a stellar evolution point of view, it is reasonable to assume that larger molecules become embedded in interstellar ices when the volatile molecules freeze out, observations have only hinted this process. Also, chemical models of PAHs embedded in an interstellar ice environment have not yet been performed due to lack of calculation power. This means that this laboratory study is leading the other two aspects of astrochemistry requiring observations of complex molecules in interstellar ices and astrochemical mathematical models to include the phenomena observed in the lab and described in this thesis. However, this study provides information to the other two aspects facilitating the closure of this gap.

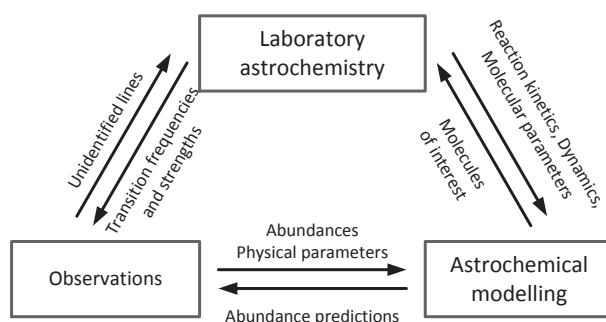


Figure 1.4 — The three aspects of astrochemistry and their relations with respect to each other.

1.5 This study

This thesis treats the chemical behaviour of carbonaceous molecules in water-dominated interstellar ices. VUV photons are considered as the chemical trigger to induce solid state chemistry as it is omnipresent. Lyman- α radiation occurs even in dense molecular clouds as a result of cosmic ray excitation of H_2 and subsequently emitting its excess energy at 122 nm (Mathis et al. 1983). It comprises the addition of new tools to laboratory astrochemistry, expanding knowledge on the behaviour of PAHs in interstellar ices and research into the role of C_2H_2 and polyynes in interstellar ice VUV photochemistry. It provides with spectroscopic tools for observers to enable the identification of the hydrocarbons encountered in interstellar ices, and it provides modellers with reaction dynamic information that can be used as an input for their models.

Chapter 2 provides with a detailed description of the experimental setup used to perform the bulk of the experiments. In this chapter, the concepts of the setup are explained and details are provided on the techniques and methods used to create the interstellar ice analog, measure its UV-vis spectrum and how the sample is subjected to VUV radiation. An example is given of how this practically works involving VUV irradiation of Pyrene, a small PAH, embedded in a water ice. The focus here is not on the science, but on the data processing and analysis techniques.

Chapter 3 treats a very long standing discussion for laboratory astrochemists who use microwave powered H_2 discharge lamps. These lamps have been used since the 1960's although the techniques for measuring the photon flux and its spectral distribution at the sample window lacks consistency and accuracy. Depending on the operational conditions, environmental parameters and experiment geometry, the VUV flux is known to vary strongly. In this chapter, a method to measure the VUV flux using the photoelectric effect with a gold-coated quartz crystal microbalance as detector is described and analyzed. The described method is also checked for accuracy and a comparison with existing methods, such as O_2 actinometry is performed.

Chapter 4 is an example of how the laboratory provides tools to observers. This study is a result of the recent identification of gas phase C_{60} . In a similar way to PAHs, C_{60} can be embedded in an interstellar ice environment. In this chapter, C_{60} is embedded in an interstellar ice matrix and its UV-vis spectrum is measured. The spectrum is fitted with gaussians in order to analyze the spectrum and make a comparison with earlier spectra in different environments. It provides a vital tool for observational astronomers to perform a search for the fingerprint UV-vis spectrum of C_{60} embedded in an interstellar ice.

Chapter 5 expands our knowledge of PAHs embedded in a solid state matrix. With the chemistry of PAHs in a pure H_2O matrix well established by previous research, a next step is made consisting of NH_3 added to the matrix in various concentrations and at different temperatures. The measurements show an interesting and profound influence on the observed VUV photochemistry of the PAH, which is put into an astrochemical context.

Chapter 6 treats a fundamental difference in observation between the IR and the UV-vis with respect to VUV photochemistry of PAHs embedded in an interstellar water ice. When studying such an ice in the lab using UV-vis spectroscopy, a rich ionization chemistry is observed while during similar experiments in the IR, no ionization is observed. This study finds the explanation to this apparent contradiction in the different PAH concentration used in both methods. The effects of concentration are also apparent in the UV-vis spectroscopy of PAHs embedded in a water ice. Increasing the PAH concentration revealed broadening and redshift in the UV-vis spectra, an effect that appeared as a result of PAH molecules coagulating inside the ice.

Chapter 7 treats the role C_2H_2 plays in interstellar ice photochemistry. To get a full picture of the photochemistry as observed, a combination of IR spectroscopy and UV-vis spectroscopy is used. This unique combination allows for tracking the formation of small volatile molecules in the IR and the formation of the polyynes in the UV-vis. Cross-referencing both observations reveal polymerization to be a very versatile VUV photochemical process that persists in competition with water related photoproducts when C_2H_2 is embedded in a water matrix. The findings of this chapter are relevant for UV photochemistry in the atmosphere of Titan and other interstellar ice environments.

Chapter 2

OASIS: optical absorption setup for ice spectroscopy

The main tool used in this research is OASIS (Optical Absorption Setup for Ice Spectroscopy). This setup enables the research of interstellar ices under VUV irradiation. These ices contain both small volatile molecules and an astrophysically relevant quantity of larger carbonaceous molecules, either by deposition, or as a result of the photochemistry. This ice is studied by the means of UV-vis absorption spectroscopy allowing the focus on the carbonaceous photoproducts.

After this description, the possibilities of the setup are explained by the example of UV photochemistry of the PAH pyrene in a pure water matrix. Explaining the methods used in determining the column density of water and PAH, the spectroscopy involved. Finally, the pyrene UV photoproducts are determined and the photochemistry is explained.

Based on Allodi, M. A., Baragiola, R. A., Baratta, G. A., Barucci, M. A., Blake, G. A., Boduch, P., Brucato, J. R., Contreras, C., Cuyllé, S. H., Fulvio, D., Gudipati, M. S., Ioppolo, S., Kaňuchová, Z., Lignell, A., Linnartz, H., Palumbo, M. E., Raut, U., Rothard, H., Salama, F., Savchenko, E. V., Sciamma-O'Brien, E., Strazzulla, G.
Space Science Review, **180**, 101 (2014)

2.1 Experimental details

Most laboratory setups that are used to study interstellar ice constituents spectroscopically, operate in the infrared and characterize *vibrational* parameters; band position, bandwidth, and band intensity. An extension to the UV-vis and near-IR allows to monitor *electronic* properties of interstellar ice analogues (Gudipati & Allamandola 2004, 2006a; Bouwman et al. 2009, 2010, 2011a). OASIS is based on incoherent, broadband, direct absorption spectroscopy. Response times are fast and photochemical processes can be studied for astronomically relevant temperatures at subsecond time scales. The performance of the apparatus has been demonstrated on the example of complex species embedded in water ice (e.g. Bouwman et al. 2011a).

The full experimental details of OASIS have not been summarized before and are listed in detail below. A schematic view of the experimental setup is shown in Fig. 2.1. OASIS consists of three units: a high vacuum chamber in which the ice is grown, a microwave powered H₂ discharge VUV irradiation source and a spectrograph equipped with a sensitive CCD camera. This spectrograph disperses broadband UV-vis light from an intense Xe arc lamp after crossing the (photoprocessed) ice.

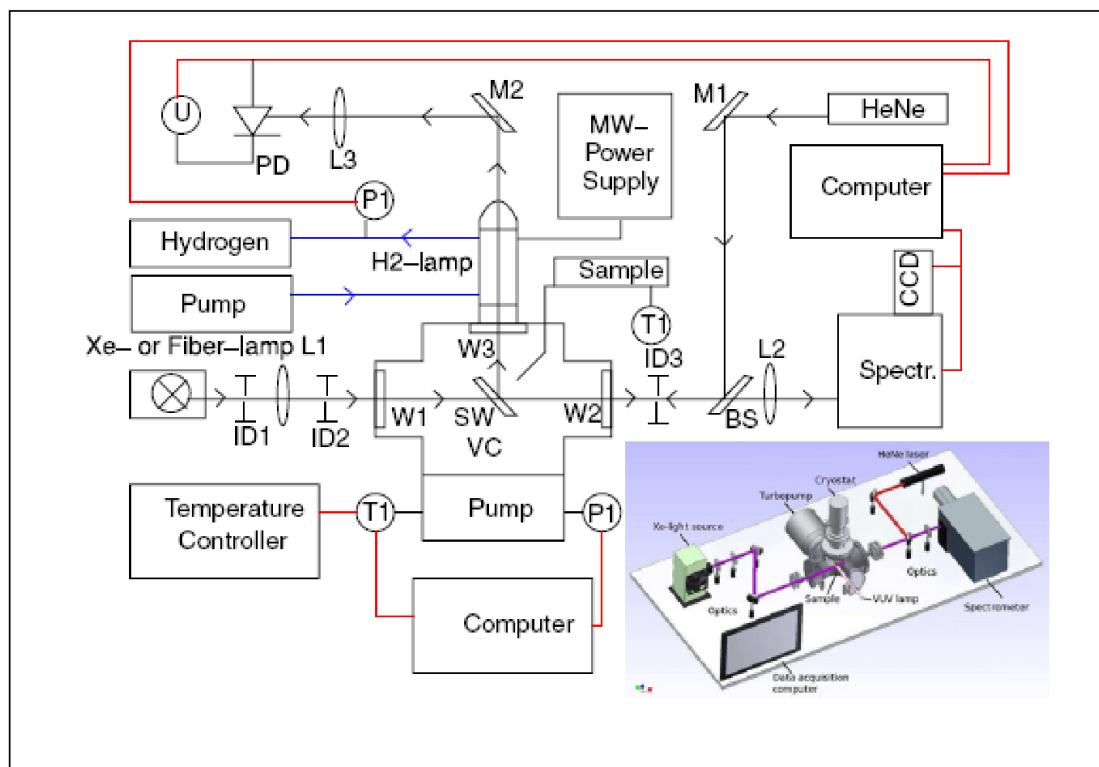


Figure 2.1 — A schematic drawing of OASIS. BS = Beam splitter, IDX = Iris Diaphragm X, LX = Lens X, MX = Mirror X, PD = Photo Diode to monitor interference fringes, PI = Pressure Indicator, SW = MgF₂ Cold Sample Window, TI = Temperature Indicator, U = Voltage meter, VC = Vacuum Chamber and WX = MgF₂ Window X. The light paths are indicated by arrows, the data wiring is indicated in red dotted lines and the hydrogen flow is indicated by blue lines. Taken from Bouwman et al. (2010).

The vacuum chamber consists of an ISO-160 6-cross-piece. Differential pumping is used to guarantee an operating pressure of 10^{-7} mbar or lower. A catalytic trap is mounted on the pre-vacuum pump to prevent pump oil from entering the vacuum chamber.

The top flange of the cross piece holds a HV rotary flange on which a closed cycle helium refrigerator (ARS type DE202NE) is mounted. A MgF_2 sample window, clamped into an oxygen free copper holder between indium gaskets, is mounted on a cold finger and centred along the rotation axis. The rotary flange allows a full rotation of the sample window through 360° while maintaining vacuum. The sample window temperature is thermally controlled between 12 and 325 K through resistive heating using a Lakeshore temperature controller. A Chromel-Au/Fe(0.07%) thermocouple is used to determine the absolute temperature value with an accuracy of 0.1 K.

The interstellar ice analogues are grown onto the cold sample window by vapour deposition. For this, a gas bulb containing the matrix material is connected to a stainless steel tube (1 mm inner diameter at the tip) ending perpendicular to the sample window with a distance of about 15 mm. Solid precursor material is evaporated using small ovens and subsequently deposited together with the matrix material. For evaporation temperatures below 50°C , an external glass oven is used, and for higher temperatures, a resistively heated steel oven attached to the deposition tube inside the chamber is taken. The flow rate of the matrix material is accurately set by a high precision dosing valve, while the evaporation rate of the solid precursor can be roughly chosen by changing the power of the heater. Condensation at any place inside the tube is prohibited by additional resistive heating along the full length of the deposition tube.

The resulting ice film thickness is accurately measured by recording the number of interference fringe maxima (m) of a HeNe laser beam ($\lambda_{\text{HeNe}} = 632.8 \text{ nm}$) that hits the sample window at an angle of $\theta = 45^\circ$. For monitoring film growth and thickness, the intensity of the reflected laser light is measured with a sensitive photodiode and the signal is digitized with a 16 bit analogue to digital converter board. The ice thickness is determined through $d = (m\lambda_{\text{HeNe}})/(2n_{\text{ice}}\cos\theta)$, with the refractive index of the predominantly H_2O ice being ~ 1.3 (see also Bossa et al. 2012, and references therein). In a typical experiment, ice thicknesses of the order of 0.4 to $2.4 \mu\text{m}$ are grown. This can be directly related to the number of H_2O molecules in the sample ice by using the value for the density of amorphous solid water ice ($\rho = 0.94 \text{ g/cm}^3$).

Also the column density of the embedded species (e.g., PAHs and fullerenes) can be monitored during deposition by correlating the absorption signal strength to an absolute column density. This yields typical concentrations of embedded (complex) species of 1:5 000 to 1:10 000 w.r.t. water.

The absorption spectrometer consists of a 150 W Xe arc lamp (LOT-Oriel) that serves as a broad band white light source. The lamp has a spectral energy distribution that covers the full detector range ($200 \text{ nm} < \lambda < 2400 \text{ nm}$). An optical system consisting of lenses and diaphragms guides the light beam through a MgF_2 window along the optical axis - coinciding with the HeNe beam that is also used for pre-alignment - and crossing the ice sample at a 45° angle. Light that is not absorbed exits the vacuum chamber through a second MgF_2 window, after which it is focussed onto the entrance slit of a spectrometer (Shamrock 303i). The spectrometer is equipped with two inter-

changeable turrets which hold four gratings in total (2400, 1200, 600 and 150 l/mm), allowing for a trade-off between wavelength coverage and spectral resolution, depending on experimental needs.

Typical electronic ice absorption bands exhibit a FWHM of 4 to 20 nm, and therefore the 150 l/mm grating is normally used. This grating provides a wavelength coverage of 500 nm. The light is subsequently dispersed onto a very sensitive 1024×256 pixel CCD camera with 16 bit digitization (ANDOR iDus DV-420 OE). The resulting signal is read out in vertical binning mode by a data acquisition computer. Spectra are taken in absorbance mode ($\tau = \log(I/I_0)$) with respect to a reference spectrum (I_0) taken directly after sample deposition. The recording of a single spectrum takes about 10 s and typically consists of 112 spectra co-added to improve S/N ratios. In a regular 3h experiment, more than 1 000 individual spectra are recorded and reduced using LabView routines.

To trigger reactions in the ice, it is irradiated by VUV radiation from a microwave powered hydrogen discharge lamp (Muñoz-Caro & Schutte 2003). The lamp consists of a flow tube clamped in a McCarroll cavity and emits mainly Ly- α radiation around 121.6 nm and, with less intensity (~20%), a band centred around 160 nm. The cavity is excited by a Sairem or Opthos Instruments MW power supply (100 W, 2450 MHz). The H₂ pressure in the lamp is maintained at about 0.4 mbar. This results in a UV photon flux of $10^{13} - 10^{14}$ photons/cm²s at the ice sample depending on the quality of the MgF₂ window that acts as a seal between the cavity and the vacuum chamber. More details on calibrating the flux of this system is given in chapter 3.

This system is used in several laboratories around the world to simulate spectral distribution of the UV interstellar radiation field (Muñoz-Caro et al. 2010; Bernstein et al. 2002; Ciesla & Sandford 2012). An addition specific for OASIS is a shutter in between window and ice substrate. This shutter blocks the VUV light until it is opened and the ice processing starts. Additionally, it eliminates the need to switch the H₂ lamp on and off for (non)irradiation allowing the lamp to stabilize. This is particularly useful when tracking the photochemical behaviour during extended periods of photolysis. The spectra are recorded in absorbance mode as described above, this yields a difference spectrum in which negative signals indicate that a precursor species is consumed, and positive signals correspond to the formation of new species. For the data reduction local linear baseline corrections and multiple Gaussian fitting of the band profiles is applied. As the HeNe laser interference signal and visible absorption spectrum are monitored simultaneously, these measurements can be performed with full characterization of the ice composition. Hence, the setup allows high quality, sub-second time resolution spectroscopic experiments in which the photoprocessing of well-defined interstellar ice analogues can be carefully monitored.

2.2 Results

The performance of the setup is demonstrated discussing the VUV irradiation of a commercially available PAH, Pyrene (Py, $C_{16}H_{10}$) embedded in water ice (see also Bouwman et al. 2009, 2011a, for cross-references). The presence of polycyclic aromatic hydrocarbons (PAHs) in many phases of the interstellar medium is evidenced by their strong and ubiquitous mid-infrared (mid-IR) emission features (Tielens 2008). Mid-IR features are efficiently emitted by a PAH after excitation by an energetic photon. Towards dense clouds, however, these mid-IR features are strongly quenched. Here, most volatile molecules are frozen out on grains forming layers of ice (e.g. Boogert et al. 2008; Öberg et al. 2010). Under such conditions, less volatile molecules such as PAHs condense on interstellar grains as well, where they will influence or contribute to the solid state chemical network.

The PAH:H₂O sample is prepared by vapor depositing (Py, $C_{16}H_{10}$, 99%) with milli-Q water vapour from a purified liquid sample. The thickness of the ice sample is monitored as described above. Typical final ice thicknesses are $\sim 1.7 \mu\text{m}$ and reproducible to within 5% or lower. In parallel, the column density of pyrene (or other PAH) molecules in the ice sample (N_{Py}) is monitored by measuring the integrated absorbance of its strongest transition ($S_2 \leftarrow S_0$). The number of pyrene molecules per cm^2 can be calculated via $N = \int \tau d\nu / 8.88 \times 10^{-13} f$ where $f = 0.33$ is the well known oscillator strength of the ($S_2 \leftarrow S_0$) transition of pyrene, and τ is optical depth. Typical pyrene concentrations range from 1:5 000 to 1:10 000 pyrene:H₂O mixture. The concentration can be roughly varied mainly by changing the H₂O flow rate and in a lesser extent by controlling PAH sample temperature. These mixing ratios are close to the predicted values for the ISM, where overall PAH abundances of the order of a few percent are taken. The neutral Py bands cover mainly the high energy range below 350 nm. The individual bands are readily assigned using available data from rare gas matrix isolation spectroscopy, e.g., for Py (Kjaergaard et al. 2000; Wang et al. 2003). The water ice environment causes bands to shift and broaden compared to rare gas matrix experiments, because of the stronger molecular interactions in the polar water environment. Similar findings are derived for other PAHs, such as anthracene, coronene and benzo[ghi]pyrene (Bouwman et al. 2011a).

Since PAH electronic transition strengths are some 100 to 1 000 times stronger than IR band strengths, photochemical processes of PAHs in ice can be followed with OASIS, even at highly dilute concentrations. This pushes the threshold for PAH detection and monitoring one to two orders of magnitude beyond the IR detection threshold. In the IR, indeed, PAH:H₂O $\sim 1:100$ mixtures are needed to discriminate PAH bands, particularly as common interstellar ice constituents mainly H₂O, but also CO, CO₂, etc. have very strong bands in the IR, making it very difficult if not impossible to disentangle weak PAH and photoproducts IR absorptions in an ice. These species, however, do not exhibit strong transitions in the optical range. Furthermore, electronic transitions are more unique than infrared vibrations which can be very similar, also for very different PAHs. Besides these spectroscopic differences, also chemical differences are observed. These differences are studied and addressed in chapter 6.

The UV photolysis of Py:H₂O mixtures has been described in detail by Bouwman et al. (2011a). The negative bands that appear between 290 and 345 nm (Fig. 2.2) are assigned to the ${}^1B_{2u} \leftarrow {}^1A_g$ electronic transition of neutral pyrene ($S_2 \leftarrow S_0$) (Halasinski et al. 2005). Most of the positive bands that form upon UV photolysis of the Py containing H₂O ice can be ascribed to the Py⁺ species. The system ranging from $\sim 411 - 470$ nm is the strongest Py⁺ transition and assigned as ${}^2A_u \leftarrow {}^2B_{3g}$. The weaker absorption bands between 350 and 370 nm are assigned to the ${}^2B_{1u} \leftarrow {}^2B_{3g}$ Py⁺ vibronic transition. The band on the red-wing of the strongest Py⁺ transition, situated around 490.1 nm, is due to the ${}^2B_{1u} \leftarrow {}^2B_{3g}$ transition. The Py⁺ bands are broader in solid H₂O than in rare gas matrices, in accordance with the stronger interactions within the H₂O matrix network. Similarly, larger shifts in peak position are expected. For the studied conditions, the direct ionisation channel is found to be dominant. This observation is also confirmed for other PAHs embedded in water ice (Bouwman et al. 2011a) and was concluded earlier by Gudipati & Allamandola (2003, 2004). Besides the rather strong Py cation absorptions, two weak bands which do not correlate with the cation features are detected around 400 and 405 nm. The band at 400 nm has been previously found to originate from an electronic transition in PyH and the band at 405 nm has been tentatively assigned to an electronic transition of 3Py (Bouwman et al. 2010).

OASIS also allows to derive temperature dependent kinetic information, simply by recording the integrated absorbances as function of time. Spectra are taken every 10 seconds during photolysis. For pyrene it is found that Py⁺ vibronic bands quickly build up to a maximum after about 1 000 s and then slowly fall off over the course of the experiment. In a similar way it is interesting to note that charged species remain in the ice, also when the VUV light is switched off. This is relevant for solid state astrochemical processes as charge induced interactions may play a key role.

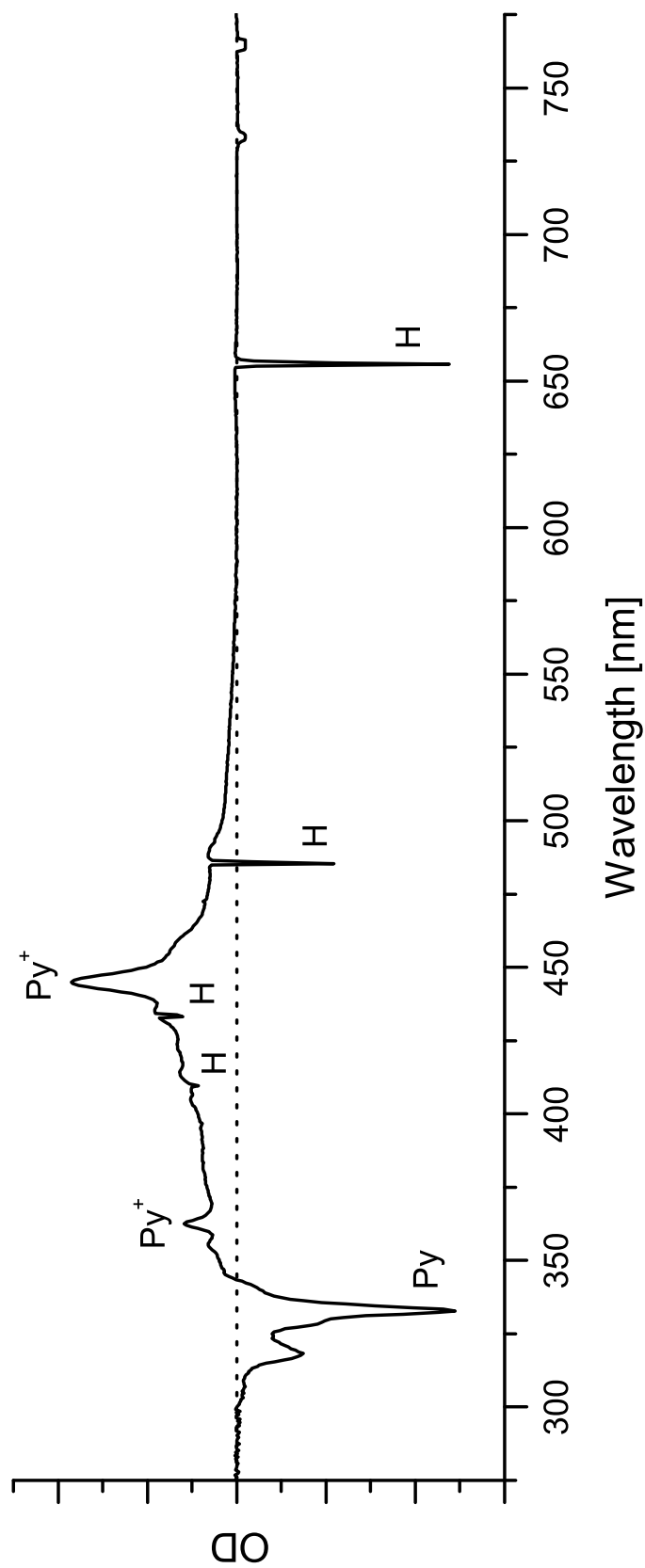


Figure 2.2 — The 280 to 800 nm spectrum of the PAH pyrene in H₂O ice, photolyzed at 25 K. Negative features indicate that the corresponding band carrier is destroyed, positive bands indicate that a species is formed. Hydrogen emission lines (sharp negative signals) originating from the VUV lamp are labeled with an H. Taken from Bouwman et al. (2011a).

Chapter 3

A straightforward method for vacuum–UV flux measurements

Abstract. Vacuum-Ultraviolet (VUV) radiation is responsible for the photo-processing of simple and complex molecules in several terrestrial and extraterrestrial environments. In the laboratory such radiation is commonly simulated by inexpensive and easy-to-use microwave-powered hydrogen discharge lamps. However, VUV flux measurements are not trivial and the methods/devices typically used for this purpose, mainly actinometry and calibrated VUV silicon photodiodes, are not very accurate or expensive and lack of general suitability to experimental setups. Here we present a straightforward method for measuring the VUV photon flux based on the photoelectric effect and using a gold photodetector. This method is easily applicable to most experimental setups, bypasses the major problems of the other methods, and provides reliable flux measurements. As a case study, the method is applied to a microwave-powered hydrogen discharge lamp. In addition, the comparison of these flux measurements to those obtained by O₂ actinometry experiments allow us to estimate the quantum yield values $QY_{122} = 0.44 \pm 0.16$ and $QY_{160} = 0.87 \pm 0.30$ for solid-phase O₂ actinometry.

Fulvio, D., Brieva, A.C., Cuyllé, S.H., Linnartz, H., Jäger, C., Henning, Th.
Applied Physics Letters, **105**, 014105 (2014)

3.1 Introduction

Vacuum-Ultraviolet (VUV) radiation plays a key role in the photo-processing of gas- and solid-phase molecules in many different terrestrial and extraterrestrial environments, from inter- and circumstellar regions to the atmosphere and the surface of planets, asteroids and comets. (Weber & Greenberg 1985; Gerakines et al. 1996; Cottin et al. 2008; Palumbo et al. 2008a; Öberg et al. 2009; Fulvio et al. 2012) For this reason, various chemistry, astronomy and biology laboratories over the world carry out experimental programs devoted to the study of VUV photoinduced processes on simple and complex molecules.

Lyman- α photons at 122 nm (10.2 eV) constitute a major component of the VUV radiation field in many of these environments, (Mathis et al. 1983; Cottin et al. 2008) explaining why in the last decades there has been a growing interest in simulating the VUV field using microwave-powered hydrogen discharge lamps (Warneck 1962). The objective of experiments carried out with these lamps is to produce reliable laboratory data allowing the comparison with models and observations. To this purpose, the irradiation source needs to be well characterized in terms of its VUV flux and spectral emission pattern.

Two common ways of carrying out absolute VUV flux measurements are: (1) actinometry and (2) calibrated VUV silicon photodiodes. Actinometry is based on the monitoring of a well characterized chemical reaction as a function of the VUV fluence. A common actinometer for estimating the Lyman- α flux produced by hydrogen discharge lamps is solid-phase O₂: (Gerakines et al. 2000; Baratta et al. 2002; Cottin et al. 2003) upon VUV photon absorption O₃ is formed from O₂, a process well documented in the gas-phase. (Warneck 1962) Due to the lack of data for solid-phase O₂ experiments, gas-phase quantum yield (QY) values are commonly used. However, a discrepancy of about a factor of 3 was observed between the flux measurements as determined by solid-phase O₂ actinometry and by a calibrated VUV photodiode. (Cottin et al. 2003) This may be due to the inaccurate assumption that gas-phase QY values are suitable for solid-phase experiments. Additional limitations of solid-phase actinometry come from technical requirements. For instance, spectroscopy is typically needed to monitor molecular abundances and a cryostat is required to condense O₂ ($T \leq 30$ K).

Calibrated VUV photodiodes measure the current induced by VUV irradiation. Although they are considered to be more precise and accurate than actinometry (as their quantum efficiency in the VUV domain is very well documented) their use is much less common. The reason of the prevalent spread of actinometry has to be found in the high cost of calibrated photodiodes and the change in the photocathode surface efficiency (difficult to characterize and monitor) due to atmospheric exposure. In some photodiodes, a passivating oxide layer is used as surface coating in order to protect the photosensitive layer from oxidation and other potential contaminations. However, the passivating layer contributes to the spectral photosensitivity of the diode and is subject to degradation as a result of VUV exposure. The degradation rate depends on the accumulated VUV fluence over time.

In the following we present an alternative method for VUV flux measurements based on the photoelectric effect. We show how by using this simple method it is possible

to obtain reproducible and reliable measurements. As a case study, the method is applied to a microwave-powered hydrogen discharge lamp. In addition, we show how the method can be applied to estimate the quantum yields for solid-phase actinometry. As an example, we discuss the case for solid-phase O₂.

3.2 Experimental Setup

Microwave-powered hydrogen discharge lamps consist of a glass tube with a constant flow of H₂ at pressure typically between 0.3 and 1 mbar. The hydrogen is excited by microwave radiation using a McCarroll (McCarroll 1970) or Evenson (Fehsenfeld et al. 1965) cavity and the microwave generator power is usually kept between 50 and 100 W. The discharge in the lamp is initiated by a Tesla coil. The typical VUV spectrum of hydrogen discharge lamps is dominated by the Lyman- α emission at 122 nm (10.2 eV) and the molecular H₂ emission feature around 160 nm (7.7 eV). The relative ratio between these two features depends on the specific experimental conditions, such as the pressure inside the discharge tube, extra components in the gas flow (for instance He added to H₂) and the relative proportion of these components. (Jenniskens et al. 1993; Westley et al. 1995; Muñoz-Caro & Schutte 2003; Cottin et al. 2008; Chen et al. 2014) In a typical laboratory setup, the lamp faces the experimental chamber (where the species under study is located) through a VUV-transparent window. The proper choice of the window material is important, as its VUV transmittance can strongly affect the spectrum and photon flux reaching the target. Special care needs to be taken as the VUV radiation can cause degradation of the VUV transmittance of the window over time. For instance, LiF windows, although having high transmittance in the VUV range, degrade significantly within hours of VUV exposure. (Cottin et al. 2003) For experiments with hydrogen discharge lamps, MgF₂ windows are the common choice to guarantee high VUV transmission down to the Lyman- α wavelength while ensuring a high level of resistance against VUV degradation.

The method presented in this Letter to easily determine VUV flux values is based on the photoelectric effect: (photo)electrons are emitted from the conduction band of a material once the acquired energy exceeds the work function of the material. Increasing the photon flux increases the number of emitted photoelectrons and the energy of the photoelectrons depends on the energy of the incident photons.

We describe now the experimental procedure, along with a few technical suggestions, before discussing the results. We choose gold as material for the photodetector (the work function of gold is between 4.2 and 5.2 eV, the spread in the value being due to the sensitivity of the work function to the surface contamination status) (Eastman 1970; Feuerbacher & Fitton 1972) and in practice we use a commercial gold-coated quartz crystal microbalance (QCM) (see Chapter 2) as photodetector to carry out the measurements. Although the work function of most metals falls in the 4 - 5 eV range, gold is a convenient choice as it is inert (therefore does not oxidise in air) and does not degrade upon VUV irradiation. Besides, gold is a material commonly available in laboratory as it is used for a number of purposes (such as IR reflectance standard or coating in QCMs). We propose QCMs because of their small size, compatibility with most systems, and low price.

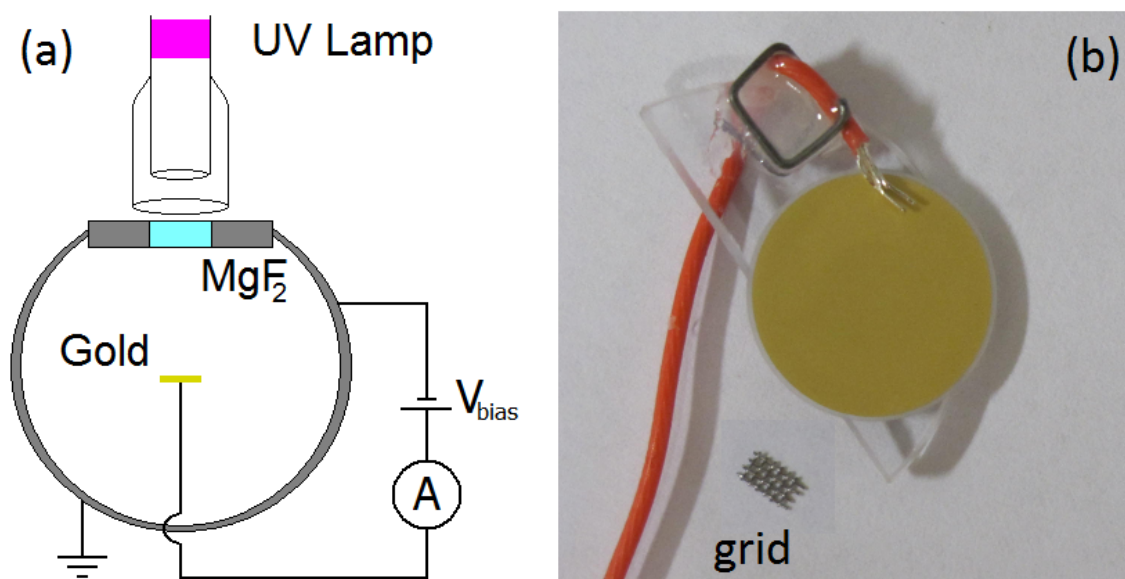


Figure 3.1 — (a) Schematic of the experimental setup and circuit used in this study. (b) Gold photodetector (diameter = 12.7 mm) mounted on a semicircular support for easy fit at the sample position. The connection detector-circuit is realized by a simple wire touching the gold surface or, when needed, a small metallic grid to facilitate the contact with the gold surface.

Figure 3.1 shows a schematic of the experimental setup and the gold QCM used. The gold photodetector is placed inside an high-vacuum chamber (base $P < 5 \times 10^{-6}$ mbar) at the sample position, connected by means of a feedthrough to a voltage controlled power supply in a circuit closed by the vacuum chamber itself (grounded). The distance from the source to the detector in our system is about 16 cm. A microammeter is used to measure the current passing through the circuit. The VUV lamp faces the photodetector through a MgF_2 window as shown in Figure 3.1. Unless otherwise specified, the experiments are conducted under constant VUV photon flux and at normal incidence of the VUV light onto the detector. The lamp is always operated with a constant flow of H_2 and a pressure of 0.6 mbar, 100 W are applied by the microwave generator to the Evenson cavity and the reflected power was below 5 W (in most cases equal to 2 - 3 W) in all experiments.

Ideally, under VUV irradiation, the photoelectrons emitted from the gold surface are collected by the chamber and return to the gold through the circuit represented in Figure 3.1. However, there are two additional effects which contribute to the current readings. First, VUV stray light may reach other spots (different than the gold photodetector) inside the chamber, with consequent photoelectron emission, and some of these photoelectrons can be collected by the detector. Second, some of the low energy electrons emitted by the gold detector may return back to it. The “spurious” photoelectrons generated by these two effects contribute antithetically to the current produced by the photoelectrons emitted by the gold surface and collected by the chamber. The

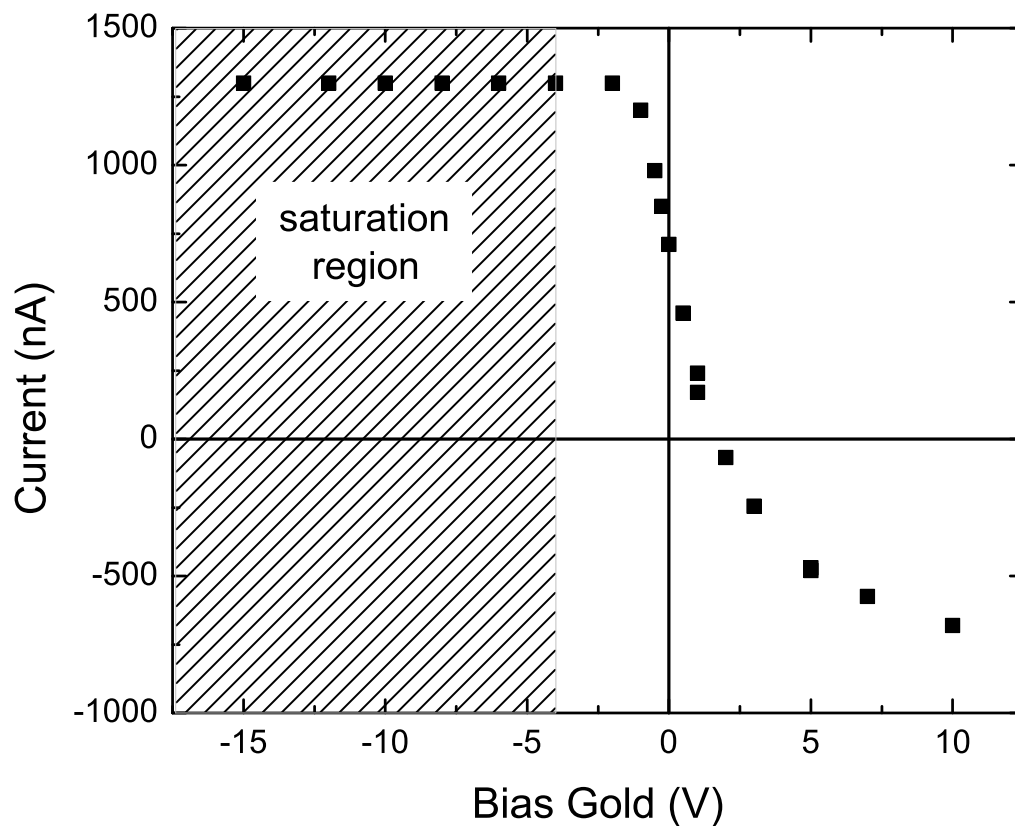


Figure 3.2 — Total current vs. V_{bias} applied to the photodetector.

Table 3.1 — VUV flux ($\text{ph cm}^{-2} \text{s}^{-1}$) as measured by the method discussed in this Letter (column 1) and by $\text{O}_2 \rightarrow \text{O}_3$ actinometry using gas-phase value $QY = 1.92$ (column 2). The last column gives the quantum yield QY values for solid-phase O_2 actinometry, as estimated from the flux measurements presented in column 1. Values of QY are in O_3 molecules formed per absorbed photon.

	Flux gold photodetector	Flux actinometry ($QY = 1.92$)	Quantum Yield solid-phase estimate
122 nm	$1.8 \pm 0.6 \times 10^{14}$	$0.4 \pm 0.1 \times 10^{14}$	$QY_{122} = 0.44 \pm 0.16$
160 nm	$3.1 \pm 1.1 \times 10^{14}$	$1.4 \pm 0.35 \times 10^{14}$	$QY_{160} = 0.87 \pm 0.30$

contribution of the spurious electrons to the overall current depends on the bias voltage V_{bias} applied to the gold photodetector, as shown in Figure 3.2. When positive or no bias voltage is applied, the spurious photoelectrons counteract the current due to the electrons photoemitted by the gold detector and collected by the chamber.

The higher the positive bias voltage applied, the stronger is the electric field which steers the spurious photoelectrons towards the gold surface. Therefore, more of them are collected from increasing distance inside the chamber. On the other hand, when increasing the negative bias voltage applied to the gold surface, the current reaches a maximum value (hereafter referred to as “saturation” current) which remains constant for higher negative values of the potential (Figure 3.2). Saturation happens when every photoelectron emitted by the gold is collected by the chamber and, simultaneously, no spurious electrons can reach the gold surface since the electric potential between gold and chamber is greater than their kinetic energy.

3.3 Method and verification

The basic concept of our method is that the saturation current is the appropriate parameter to determine the VUV flux at the position of the gold photodetector. If so, the saturation current has to depend linearly on (i) the surface area of the gold detector and (ii) the power applied by the microwave generator, as the VUV flux scales linearly with the surface area and the power applied (Bénilan et al. 2011). We have verified these two points experimentally. Figure 3.3 presents the results of (i), for the whole range of V_{bias} (Figure 3.3a) and the value of the saturation current vs. the surface area of the gold detector (Figure 3.3b). The area of the photodetector was cut into smaller areas between consecutive experiments. The resulting data points in Figure 3.3b can be fitted by a straight line passing through the origin as expected for a current which depends only on the flux absorbed. The results of (ii) (not shown for the sake of brevity) confirm the linear correlation between the saturation current and the power applied by the microwave generator in the range 65 - 120 W. These two control experiments prove that saturation depends on the VUV flux rather than the limited surface of the gold detector or any other undesirable effect in the circuit.

We now describe the procedure to determine the VUV flux. The total flux F_{tot} can be divided into the contribution of the spectral components centered at different λ : F_λ . Knowing the photoelectric yield PY_λ of gold for photons of given wavelength λ and the current I_λ^{sat} produced by these photons, the VUV photon flux F_λ is:

$$F_\lambda = \frac{I_\lambda^{sat}}{e \times PY_\lambda \times A}$$

where e is the elementary charge and A is the irradiated area. VUV spectra of hydrogen discharge lamps are dominated by two spectral features: the Lyman- α emission centered at 122 nm and the molecular H_2 emission around 160 nm. This means that we need to estimate the flux due to each spectral feature: F_{122} and F_{160} . To this purpose, two measurements of the saturation current have to be performed: the first one as described above, I^{sat1} ($= I_{122}^{sat1} + I_{160}^{sat1}$), and the second one adding an extra window

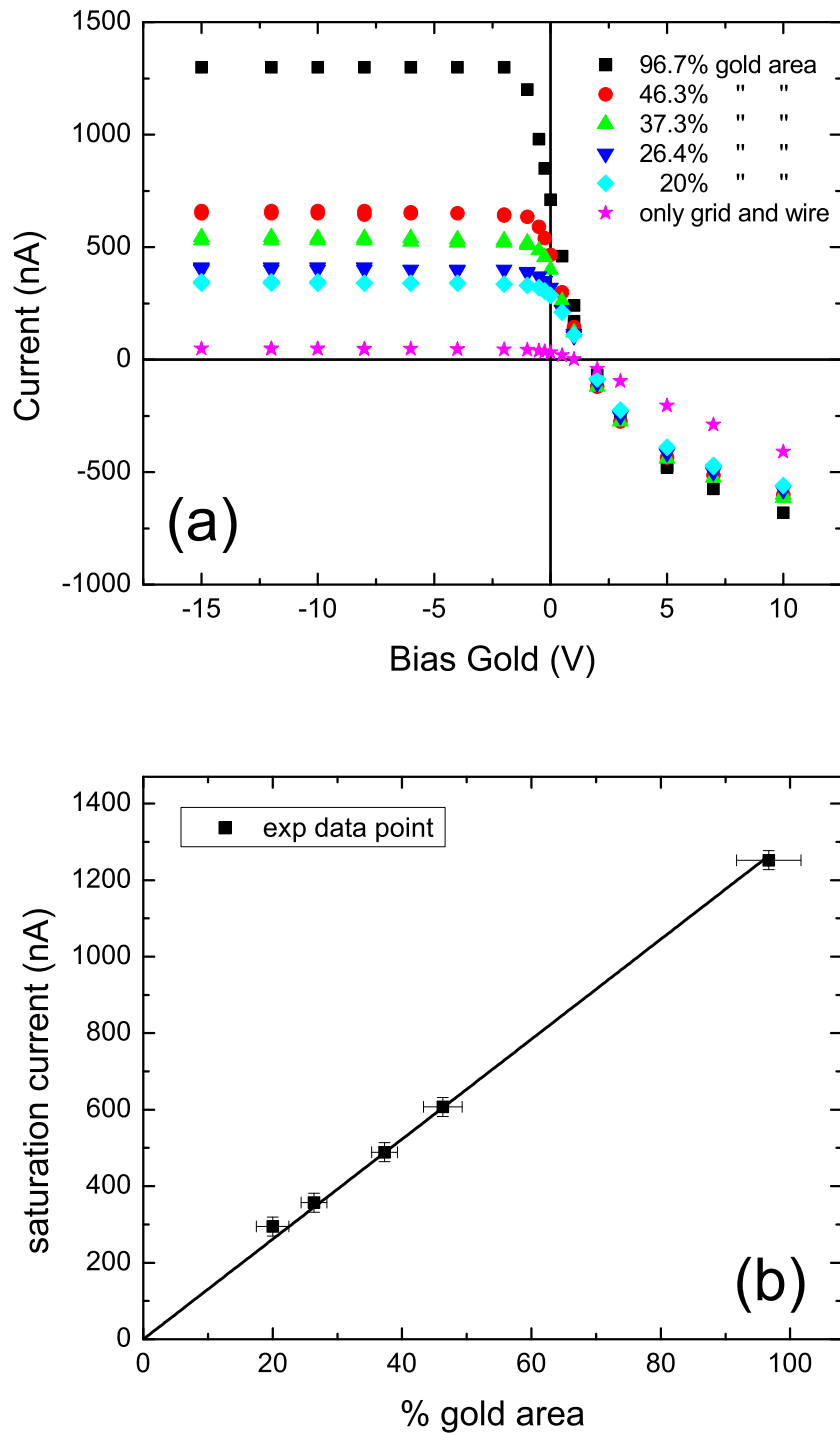


Figure 3.3 — (a) Same as in Figure 3.2 for different surface areas of the gold photodetector. The lowest curve (\star) shows the current only due to the metallic grid and wire used for the circuit contact with the gold surface. (b) Saturation current for different gold surface areas (from (a)) and best fit to the data points. Saturation current values are plotted after removing the contribution of the grid and wire (curve \star).

with known transmittance (T_{122} and T_{160}) at the wavelength of each emission feature, I^{sat2} ($= I_{122}^{sat2} + I_{160}^{sat2}$). From expression (1) we get a system of two linear equations in two unknowns:

$$\begin{cases} I^{sat1} &= Ae(PY_{122}F_{122} + PY_{160}F_{160}) \\ I^{sat2} &= Ae(PY_{122}T_{122}F_{122} + PY_{160}T_{160}F_{160}) \end{cases}$$

The solution of the system provides the flux for each spectral component. For measuring I^{sat2} we use a sapphire window, opaque to the 122-nm component while partially transmitting the 160-nm one. The transmittance T_{160} of this sapphire window is measured to be 0.5. Solving (2) we find, for the lamp settings discussed before, the following flux values at the detector position (Table 3.1, column 1): $F_{122} = 1.8 \pm 0.6 \times 10^{14}$ ph cm⁻² s⁻¹ and $F_{160} = 3.1 \pm 1.1 \times 10^{14}$ ph cm⁻² s⁻¹. We point out that the broadness of the emission band is one of the main error sources, mainly because of the uncertainty on the PY_{λ} value used to estimate the flux from expression (1). We have used $PY_{122} = 2 \times 10^{-2}$ and $PY_{160} = 1 \times 10^{-3}$ (in units of photoelectrons per incident photon) (Feuerbacher & Fitton 1972). We want also to point out that discerning between the two spectral components is required, as recent solid-phase experiments have shown that photoinduced processes can be wavelength dependent (Chen et al. 2014; Fayolle et al. 2011).

3.4 Verification

An application of the method discussed in this Letter is the estimation of the quantum yields for solid-phase actinometry. As an example, we discuss the case of solid O₂. First, we have re-determined the VUV flux by O₂ actinometry experiments (under the same experimental conditions). Inside the high-vacuum chamber, solid O₂ is grown at 11 - 15 K onto a KBr substrate placed in thermal contact with a closed-cycle helium cryostat. The thickness of the O₂ film is always > 1.8 micron (to ensure total absorption of the VUV photons) and is determined by laser interferometry as described in Fulvio et al. (2009). An FTIR spectrophotometer (Bruker Vertex 80v) is used to record transmittance spectra (resolution: 1 cm⁻¹) in the range 6000 - 400 cm⁻¹. The flux is derived by measuring the area of the ν_3 infrared band of O₃ centered at 1040 cm⁻¹ as a function of the irradiation time:

$$Flux = \frac{Area(\nu_3)}{time \times QY \times A(\nu_3)}$$

where QY is the O₃ quantum yield and $A(\nu_3)$ is the integrated absorption strength for the ν_3 band. While the integrated absorption strength value is known for solid O₃, ($A(\nu_3) = 1.4 \times 10^{-17}$ cm molecule⁻¹ Teolis et al. 2007). there is a lack of solid-phase data for the O₃ quantum yields. To date, the gas-phase-estimated value $QY = 1.92$ has been commonly used. Employing $QY = 1.92$ we find the flux values reported in column 2 of Table 3.1. These values are about a factor of 3 smaller than the flux values obtained using the gold photodetector (column 1). This trend is similar to the one found

when comparing the flux measurements obtained by solid-phase O₂ actinometry and a calibrated VUV photodiode (Cottin et al. 2003). We think that the discrepancy may be due to the use of gas-phase QY values for solid-phase experiments. Knowing the flux values from the measurements with the gold photodetector and using expression (3), we estimate the QY values for solid-phase O₂ actinometry as reported in column 3. However, the precision of these estimates strongly depends on the precision on the measurements of the photoelectric yields of gold. In this view, our results suggest the need for more precise photoelectric yield measurements.

Finally, we want to point out two additional advantages of our method for VUV flux measurements: (1) the response of the photodetector is “limited” to 5 - 11 eV; this is the spectral range where the lamp emission simultaneously induces photoelectric effect on gold and is transmitted by the MgF₂ window; on the other hand, the spectral response of VUV silicon photodiodes extends to the visible and IR range; this last case may lead, if neglected, to an overestimated VUV flux measurement; (2) our method can be used even in conditions of “rough” vacuum: when slowly increasing the pressure in the vacuum chamber, our measurements remain unaffected up to 1×10^{-2} mbar; this is another advantage with respect to actinometry.

3.5 Conclusions

In summary, we present a straightforward method to determine the VUV flux and discuss in detail the case of a commonly used microwave-powered hydrogen discharge lamp. Technical details and pragmatic suggestions are provided. The main advantages of the proposed method and detector can be summarized as follows: no need for spectroscopy; no need for cryogenic components; response in the spectral region 5 - 11 eV, low cost, small size and easy fitting in almost every system; suitable for chamber pressure up to 1×10^{-2} mbar. Finally, the method here presented can be applied to estimate the quantum yields for solid-phase actinometry. As an example, the case of solid-phase O₂ actinometry has been discussed.

Acknowledgments

This research has received funding from the European Community’s Seventh Framework Programme (FP7/2007-2013) under Grant Agreement No. 238258. A. C. B acknowledges support by the EU FP7-Marie-Curie IEF (grant agreement no. 274794).

Chapter 4

UV-vis spectroscopy of C₆₀ embedded in water ice

Electronic solid state spectra are recorded for C₆₀ embedded in 40 K water ice using broad band direct absorption spectroscopy, and assigned with reference to existing matrix data. The results are interesting in view of the recent gas phase detection of fullerenes in the interstellar medium and provide a realistic solid state signature to search for frozen C₆₀ in space.

Cuyllé, S.H., Linnartz, H., Thrower, J.D.
Chemical physics letters, **550**, 79 (2012)

4.1 Introduction

Decades of dedicated fullerene research have resulted in a wealth of spectroscopic and dynamical information on fullerenes and carbon nanotubes (Kroto et al. 1985, 1991). Their special properties have been intensely investigated and various applications have been proposed ranging from e.g., solar cell applications (Sariciftci et al. 1993) to targeted drug delivery (Simon et al. 2007). With their detection on Earth, fullerenes were also proposed to be present in the interstellar medium. First observations that hinted in this direction were reported in by Werner et al. (2004) and Sellgren et al. (2007). An unambiguous identification was reported by Cami et al. (2010) who observed both C_{60} and C_{70} in the unusual planetary nebula Tc1 by comparing Spitzer-IRS and laboratory infrared emission gas phase spectra of vibrational modes (Cami et al. 2010). Since this discovery, C_{60} has been detected along other lines of sight, including reflection nebulae (Sellgren et al. 2010), embedded young stellar objects, a Herbig Ae/Be star, a post-asymptotic giant branch star (Roberts et al. 2012) and H-deficient RGB stars (García-Hernández et al. 2011), indicating that fullerenes may be widespread in space. This is actually not that surprising given the fact that many carbon bearing species have been identified in the interstellar medium and fullerenes belong to the most stable carbon species (see also Ehrenfreund & Foing 2010, and references therein); they are predicted to carry up to 1.5 % of the available carbon in inter- and circumstellar environments. Even more recently, Evans et al. (2012) reported the possible detection of solid-phase C_{60} in the binary XX Oph. Indeed, at the low temperatures of dark interstellar clouds, C_{60} molecules are expected to stick together and to form agglomerates, as has been observed for polycyclic aromatic hydrocarbons (PAHs) (Geers et al. 2009). It also has been proposed that PAHs, as large non-volatile species, will accrete in dense interstellar clouds onto cold dust grains together with other species most noticeably water to become embedded in interstellar ices. This idea has been extensively discussed by Gudipati & Allamandola (2003) and Bouwman et al. (2009) and in Chapter 6, and is consistent with the astronomical observation that strong infrared emission lines originating from UV excited PAHs are not visible from such clouds, as in the ice matrix the responsible vibrational modes are quenched. Here, volatile molecules freeze out, forming layers of ice on micrometer sized dust grains (Öberg et al. 2011), providing a molecule reservoir. Upon external chemical triggers, i.e., UV photon irradiation, ice species participate in a solid state chemical reaction network (see e.g. Wakelam et al. 2010; Gudipati & Allamandola 2006a). A similar evolution is expected for C_{60} and for this reason the UV-vis spectrum of C_{60} embedded in water ice has been studied. This spectrum provides, in essence, the spectroscopic tool with which to search for C_{60} embedded in water ice.

Table 4.1 — Strong spectral features of C₆₀ embedded in water ice (C₆₀:H₂O ~1:5000) at 40K.

Label	ν_{H_2O} (cm ⁻¹) _{vac}	λ_{H_2O} (nm) _{vac}	FWHM (cm ⁻¹)	$\nu_{Ne/hexamatrix}$ (cm ⁻¹) _{vac}	Transition	$\Delta\nu_{H_2O-matrix}$ (cm ⁻¹)
A	45 952(130)	217.6	2189	47 633(228) _{hex}	8 ¹ T _{1u} - ¹ A _g 0 ₀	-1681
B	42 256(111)	236.7	3617	43 988(194) _{hex}	7 ¹ T _{1u} - ¹ A _g 0 ₀	-1732
C	38 753(94)	258.0	2961	38 983(153) _{hex}	6 ¹ T _{1u} - ¹ A _g 0 ₀	-230
D	34 270(75)	291.8	4756	34 257(12) _{Ne}	5 ¹ T _{1u} - ¹ A _g 0 ₀	-622
E				33 013(11) _{Ne}	4 ¹ T _{1u} - ¹ A _g 0 ₀	
F	30 618(61)	326.6	1382	30 969(10) _{Ne}	3 ¹ T _{1u} - ¹ A _g 0 ₀	-351
G	29 737(57)	336.3	2619		Unknown	-
H	27 116(48)	368.8	2901	26 604(7) _{Ne}	2 ¹ T _{1u} - ¹ A _g 0 ₀ (tentative)	512

4.2 Experiment

The experiments are performed with OASIS, our Optical Absorption Setup for Ice Spectroscopy that has been described in detail by Bouwman et al. (2009) and in chapter 2. The setup consists of a high vacuum chamber (3×10^{-7} mbar) in which ices are grown on a thermally controlled MgF_2 deposition window. The window is mounted on top of the cold head of a closed-cycle helium cryostat. An integrated tip heater allows accurate temperature control between 13 and 325 K. Here, experiments are performed at an astronomically relevant and fixed temperature of 40 K. The co-deposition system for H_2O (Milli-Q, purified by three freeze-pump-thaw cycles) and C_{60} (Sigma-Aldrich, 99%) consists of an external manifold with a dosing valve for the water matrix and a resistively heated oven affixed to the end of the line for C_{60} . Heating the oven with 2-3 W is sufficient for thermal evaporation of the C_{60} without chemically altering it. This allows a homogeneous mixing of both constituents, typically in a $C_{60}:H_2O$ ratio of roughly 1:5000. During deposition, the ice thickness is monitored using a HeNe laser based interferometric system. Typical deposition rates amount to about 3 nm/s and final ice thicknesses are between 0.5 and 1 μm . The ice is spectroscopically investigated by focusing white light of a Xe-arc lamp through the ice onto the inlet of an Andor Shamrock 303i spectrometer. This monochromator disperses the light in a range from 200 - 1000 nm with a best spectral resolution of 0.55 nm. Given the large spectral range covered here, this yields different absolute accuracies in terms of absolute numbers (cm^{-1} , see Table 4.1). UV-vis spectra are recorded every 10 s and several spectra can be added to increase S/N-ratios. A particular benefit of this technique is that a large spectral range can be covered in one run and this allows simultaneous investigation of many spectral features, also in the time domain ensuring a constant ratio between C_{60} and water over the depth in the ice.

4.3 Results

Fig. 4.1 shows the broadband (200 - 420 nm) UV-vis spectrum of C_{60} embedded in water ice. This spectrum has been recorded in a single pass experiment during 10 s. Besides several broad bands in the 200-400 nm region, a rather large number of narrower bands are observed for wavelengths longer than 365 nm. An expanded view of this region is shown in Fig. 4.2. The spectral features show similarities with previously recorded spectra for C_{60} in matrix environments other than water - hexane, n-hexane at 77 K, and 3-methylpentane (Hare et al. 1991; Leach et al. 1992), Ne and other rare gas matrices at 4 K (Sassara et al. 2001, 2002) and hexane/polystyrene (Pavlovich & Shpilevsky 2010) - and have been assigned in these studies to vibronic transitions. Electronic gas phase spectra of C_{60} have been predicted or measured (Catalán 1994; Catalán & Pérez 2000; Dai et al. 1994; Haufler et al. 1991), but their accuracy is limited; the predictions are derived from the solid state work (and are not further considered here) and the gas phase measurements concern high temperature environments. For this reason mainly Ne matrix data (Sassara et al. 2001, 2002) complemented with n-hexane data (Leach et al. 1992) are used to guide the identification of the bands observed here in a water ice matrix. Ne environments provide the lowest matrix-induced band shifts and this is confirmed in Table 4.2 for the limited set of bands for which gas phase data are avail-

able (Sassara et al. 2001, 2002; Catalán 1994); the matrix shifts typically amount to a few tens of cm^{-1} (and up) with respect to unperturbed gas phase data. This is comparable with values that have been found for different PAHs (Bouwman et al. 2009).

A sequential fit procedure has been applied. The five broader bands (A-E) not overlapping with the weaker features are fit using the χ^2 fitting tool of Origin 8. Here a well educated guess is made for the three initial Gaussian parameters - centre wavelength, integrated absorption area and FWHM after which the fitting is performed, restricting the centre wavelength to a certain range centered on the peak position found in the different matrix studies. The resulting optimal values are listed in Table 4.1. As the bands are very broad the accuracy here is limited. This is also reflected in the large variation of derived $\Delta\nu$ H_2O -matrix/gas values for the stronger and broad features. The red wing of the sixth band (F) at $29\,737\text{ cm}^{-1}$ and the seventh band around $27\,116\text{ cm}^{-1}$ (G) overlap with the weaker features and a χ^2 method does not work, as a baseline in the $28\,500$ to $23\,500\text{ cm}^{-1}$ region is needed to separately fit the partially overlapping narrower bands. Therefore the fitting procedure has been adapted in such a way that the G band coincides with the measured spectrum for a number of hand-chosen overlap points, while taking into account the solution for the adjacent Gaussian around $29\,737\text{ cm}^{-1}$ for the F band. As also the F and G bands overlap, the fit is optimized for one Gaussian per optimization run, and repeated until the fitting parameters remain stable. The G assignment is tentative and possibly incorrect, given the $\Delta\nu$ value that clearly deviates from the other values found for the stronger and broad features.

The subsequent fitting of the narrower features in the $365 - 425\text{ nm}$ region follows a rather similar method. Most peak positions can be estimated from the spectrum and eventually compared to the data summarized in Sassara et al. (2002). Separate peak-to-peak pair optimization results in 17 Gaussian bands (a-q) fitted to the narrower features. This is shown in Fig. 4.2. The resulting band parameters are listed in Table 4.2.

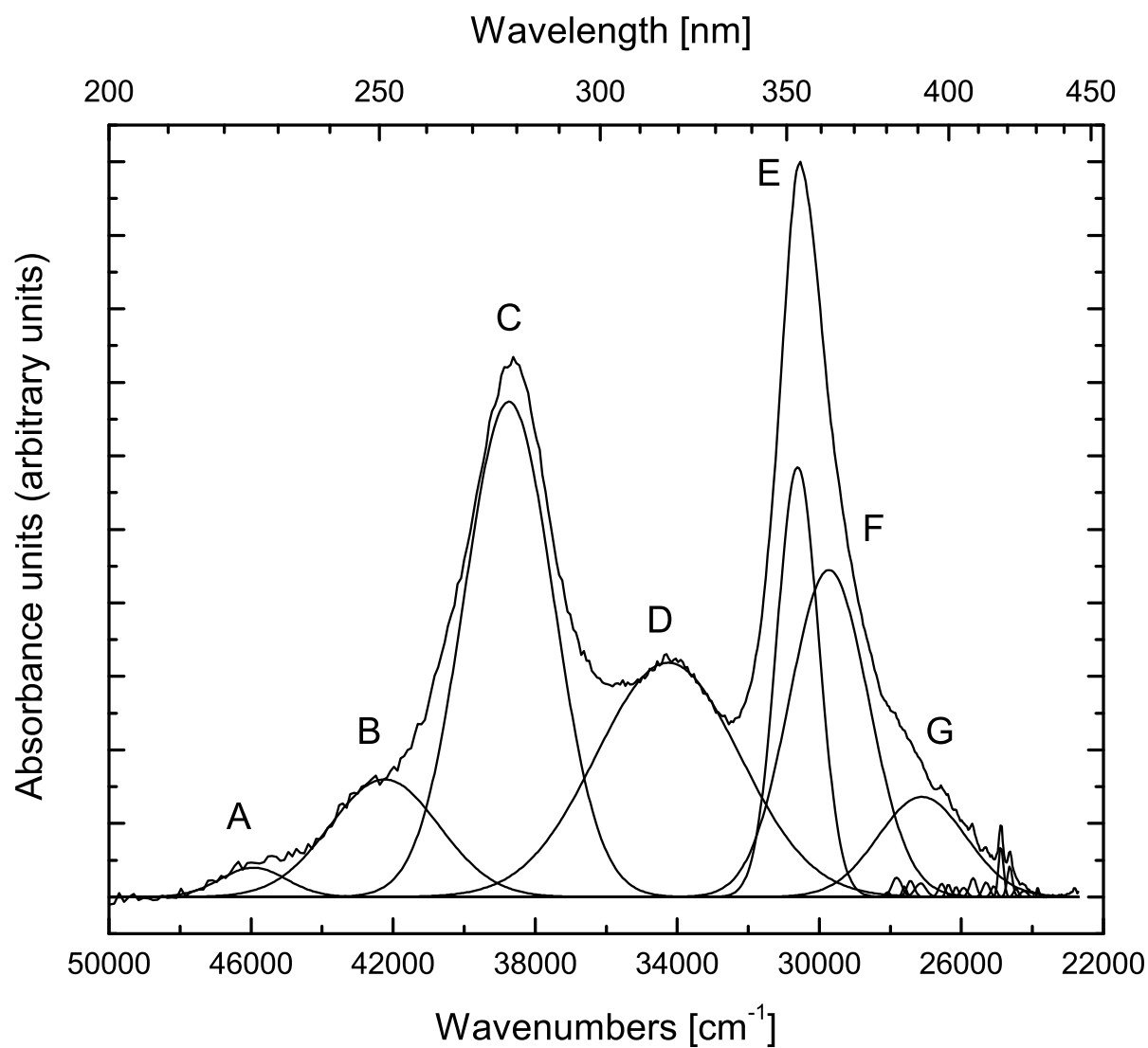


Figure 4.1 — Broadband spectrum of C_{60} embedded in water ice showing Gaussian fits of individual vibronic bands previously assigned in other matrix environments. The band assignments are reported in Table 4.1.

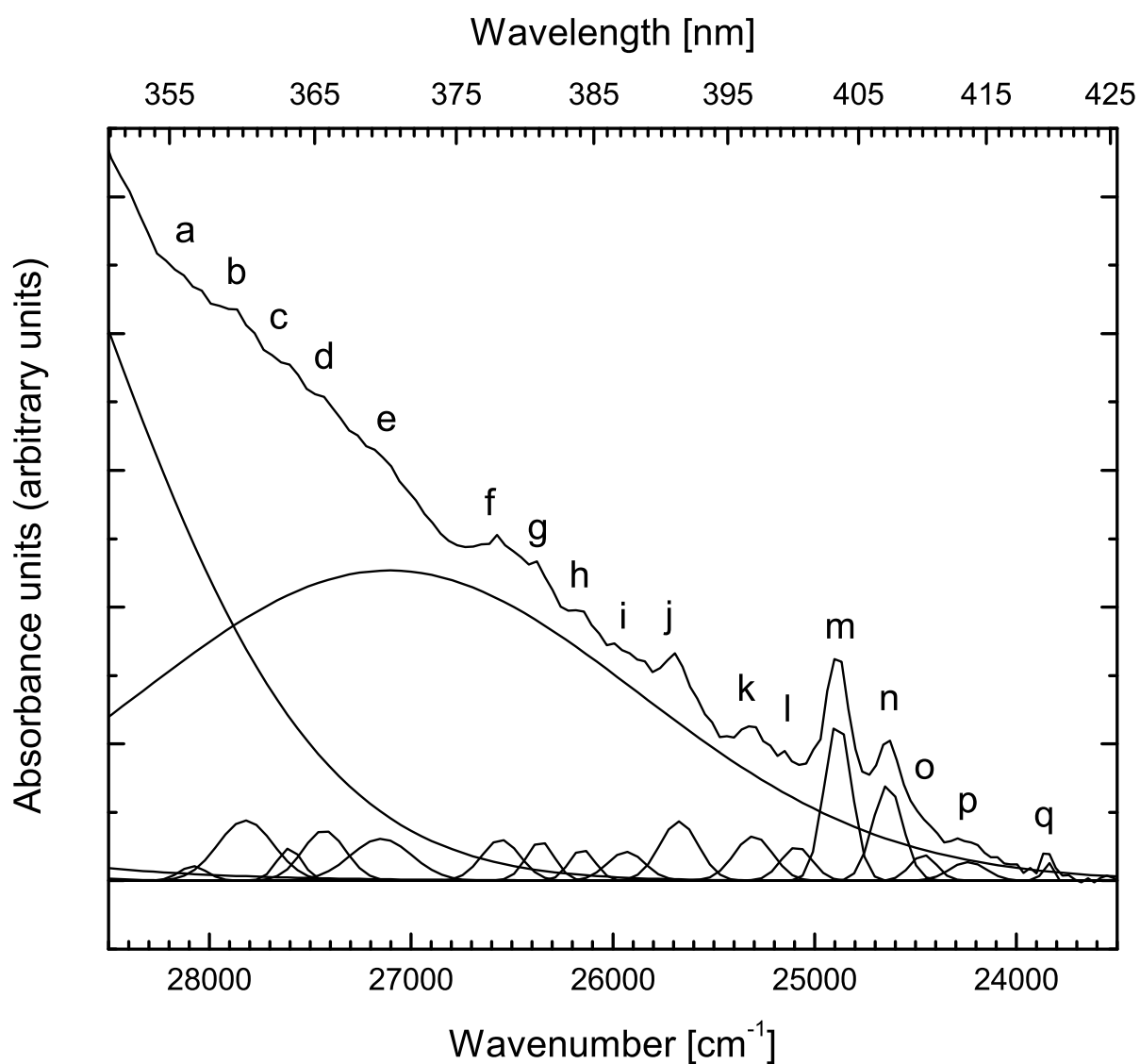


Figure 4.2 — Extended view of figure 4.1 showing details of a series of narrower bands including Gaussian fits that follow the assignment of vibronic bands, previously assigned in other matrix environments. The band assignments are reported in Table 4.2.

Table 4.2 — Weaker and narrow spectral features of C_{60} embedded in water ice ($C_{60}:H_2O \sim 1:5000$) at 40K ($\sim 365-420nm$).

Label	ν_{H_2O} (cm^{-1}) _{vac}	λ_{H_2O} (nm) _{vac}	FWHM (cm^{-1})	$\nu_{Ne}/hexmatrix$ (cm^{-1}) _{vac}	ν_{gas}	Transition	$\Delta\nu_{H_2O-matrix/gas}$ (cm^{-1})
a	28 088(52)	356.0	159	28 097(8) _{Ne}	-	$2^1G_u - ^1A_g + h_g(7)$ (tentative)	-9/-
b	27 828(51)	359.4	323	27 941(8) _{Ne}	-	$2^1G_u - ^1A_g + h_g(6)$ (tentative)	-113/-
c	27 611(50)	362.2	147	27 747(8) _{Ne}	-	$2^1G_u - ^1A_g + h_g(5)$	-136/-
d	27 439(50)	364.4	249	27 456(8) _{Ne}	-	$2^1G_u - ^1A_g + h_g(4)$	-17/-
e	27 156(49)	368.2	357	27 390(8) _{Ne}	-	$2^1T_{1u} - ^1A_g + h_g(3)$	-234/-
f	26 563(47)	376.5	223	26 853(7) _{Ne}	-	$2^1T_{1u} - ^1A_g + h_g(1)$	-290/-
g	26 367(46)	379.3	159	26 710(7) _{Ne}	-	$2^1G_u - ^1A_g 0_0^0$	-147/-
h	26 160(45)	382.3	164	26 604(7) _{Ne}	-	$2^1T_{1u} - ^1A_g 0_0^0$	-237/-
			150	26 324(7) _{Ne}	-	$1^1T_{1u} - ^1A_g + h_g(7)$	-164/-
			159	26 358(7) _{Ne}	-	$1^1T_{1u} - ^1A_g + a_g(2)$	-198/-
			159	26 393(7) _{Ne}	-	$1^1T_{1u} - ^1A_g + h_g(8)$	-233/-
i	25 942(45)	385.5	219	26 172(7) _{Ne}	-	$1^1G_{1u} - ^1A_g + a_g(2)$	-230/-
			159	26 102(7) _{Ne}	-	$1^1T_{1u} - ^1A_g + h_g(6)$	-160/-
j	25 680(44)	389.4	224	25 935(7) _{Ne}	25 934	$1^1T_{1u} - ^1A_g + h_g(5)$	-255/-254
k	25 311(43)	395.1	224	25 550(7) _{Ne}	25 544	$1^1T_{1u} - ^1A_g + h_g(3)$	-239/-233
l	25 096(42)	398.5	181	25 343(6) _{Ne}	-	$1^1T_{1u} - ^1A_g + a_g(1)$	-247/-
m	24 892(41)	401.7	158	25 120(6) _{Ne}	25 133	$1^1T_{1u} - ^1A_g + h_g(1)$	-228/-241
n	24 646(41)	405.7	173	24 852(6) _{Ne}	24 858	$1^1T_{1u} - ^1A_g 0_0^0$	-206/-212
o	24 469(40)	408.7	154	24 711(6) _{Ne}	-	$1^1G_u - ^1A_g 0_0^0$	-242/-
p	24 248(39)	412.4	215	24 103(58) _{hex}	-	$2^1G_u - ^1A_g 0_0^0$	-145/-
q	23 857(38)	419.2	46	23 676(56) _{hex}	-	$2^1H_u - ^1A_g + h_g(8)$	-181/-

4.4 Assignments

The assignment of the resolved bands is based both on previous matrix and gas phase experiments. As stated before, the latter are essentially unperturbed, but not necessarily more precise because of the high temperature environments in which they have been recorded. The assignments within the different studies reported in literature are largely consistent but not fully in agreement with each other. In order to circumvent further confusion, the present study follows the assignments by Leach et al. (1992) and Sassara et al. (2001, 2002). The strong features labeled A through G - except F represent a series of vibronic transitions into the ${}^1T_{1u}$ excited state, starting from the 1A_g ground state of C_{60} . The central band (D) is located at $34\,270\text{ cm}^{-1}$, and is composed of the $4^1T_{1u} - {}^1A_g$ and $5^1T_{1u} - {}^1A_g$ bands. As found in Leach et al. (1992) it is not possible to resolve both bands and an averaged value is used to calculate the matrix shift. The band at $38\,753\text{ cm}^{-1}$ (C) corresponds to the $6^1T_{1u} - {}^1A_g$ transition. The next two transitions involving the 7^1T_{1u} and 8^1T_{1u} levels, around $42\,256\text{ cm}^{-1}$ and $45\,952\text{ cm}^{-1}$, respectively, are harder to discern, as towards shorter wavelengths there is an increasing degree of extinction, likely because of UV scattering in the ice or setup, causing spectral features to become significantly weaker. A similar behavior was attributed by Apostolopoulou et al. (2009) to C_{60} nanoparticles, consistent with a picture in which C_{60} tends to form agglomerates Ismail & Rodgers (1992). On the red side, the $3^1T_{1u} - {}^1A_g$ transition (band E) around $30\,618\text{ cm}^{-1}$ shows an extensive wing up to $24\,000\text{ cm}^{-1}$ and needs two additional Gaussians (bands F and G) for appropriate fitting. The only stronger feature reported in this region is the $2^1T_{1u} - {}^1A_g$ transition and band G is found to be the nearest (Orlandi & Negri 2002). The origin of feature F is unknown, but has to be taken into account as without it, no accurate fit can be obtained. Typical shifts with respect to values obtained in a Ne matrix or hexane environment (also listed in Table 4.1) are of the order of a several hundreds of cm^{-1} and should be regarded with care, given the large uncertainties.

The weaker features labeled a-q, visible in Fig. 4.2, in the 350 - 420 nm region have been assigned in previous matrix work (Leach et al. 1992; Sassara et al. 2001, 2002) to electronic transitions in the 1H_u , 1G_u and ${}^1T_{1u}$ states with excited Jahn-Teller (h_g) or symmetric (a_g) modes. A comparison of the $C_{60}:\text{H}_2\text{O}$ spectra to those recorded in a 4 K Ne matrix shows a significant additional broadening as matrix effects in the water ice are indeed expected to be stronger than in a Ne environment. This washes out some of the weakest features that can still be observed in e.g., Sassara et al. (2001). Therefore, special care is needed to extrapolate the Ne matrix results to solid water, particularly as spectral separations are of the order of typical matrix shifts. There are, however, a few distinct spectral features in Fig. 4.2 that facilitate the identification of the subsequent bands and the most probable assignment is presented here. Features m and n around $24\,892$ and $24\,646\text{ cm}^{-1}$ are stronger than the other bands and likely correspond to the $1^1T_{1u} - {}^1A_g + h_g(1)$ and $1^1T_{1u} - {}^1A_g$ bands as assigned in Sassara et al. (2002). The latter band actually belongs to the series of stronger features discussed before and it should be noted that the FWHM-value is smaller than found for the bands A-G. Furthermore, there is an empty region around $26\,800\text{ cm}^{-1}$, between features e and f that is also found in the other matrix studies.

Using this as a starting point, feature o is assigned as $1^1G_u - ^1A_g$ through its relative distance from feature n. Features p and q are out of the range discussed in Sassara et al. (2002). Band p can be labeled as $2^1G_u - ^1A_g$ following Leach et al. (1992) or $1^1G_u - ^1A_g$, according to Sassara et al. (2001, 2002). The latter assignment, however, is in contradiction with the previous o-feature labeling. Based on its distance from feature n, band q is assigned as $2^1H_u - ^1A_g + h_g(8)$. Features j and k are due to the $1^1T_{1u} - ^1A_g + h_g(5)$ and $1^1T_{1u} - ^1A_g + h_g(3)$ transitions, respectively, based on their relative strength and distance from feature m (Sassara et al. 2002). Due to overlap of these two bands, a previously observed feature assigned to $1^1G_u - ^1A_g + h_g(5)$ is not observed here. Feature l is associated with $1^1T_{1u} - ^1A_g + h_g(1)$ and is in between k and m.

Moving to the shorter wavelengths, the assignment of the bands a-i is not trivial, as these features suffer from serious spectral overlaps and multiple transitions effectively result in a single bump in the water ice environment. Feature i may be due to either $1^1G_u - ^1A_g + a_g(2)$ or $1^1T_{1u} - ^1A_g + h_g(6)$ that are difficult to distinguish in the Ne matrix. Feature h is the next peak, and can be associated with three overlapping modes: $1^1T_{1u} - ^1A_g + h_g(7)$, $1^1T_{1u} - ^1A_g + a_g(2)$ and $1^1T_{1u} - ^1A_g + h_g(8)$. Feature g can be linked to the adjacent peak, which is $2^1T_{1u} - ^1A_g$. The last peak before the earlier mentioned empty region, peak f, may be due to multiple transitions that form a single peak, comprising the $2^1T_{1u} - ^1A_g + h_g(1)$ and the $2^1G_u - ^1A_g$ band in its long wavelength flank. Crossing the empty zone, the measurements of Sassara et al. (2002) show three peaks in a strongly sloping baseline. These are linked to features c, d and e in water ice, labeled as $2^1G_u - ^1A_g + h_g(5)$, $2^1G_u - ^1A_g + h_g(4)$ and $2^1T_{1u} - ^1A_g + h_g(3)$, respectively. Finally, features a and b are out of the range of the measurements of Sassara et al. (2001), and tentative assignments are $2^1G_u - ^1A_g + h_g(7)$ and $2^1G_u - ^1A_g + h_g(6)$, respectively. Also here it is found that in the water ice environment the bands experience a redshift with respect to the Ne matrix values. A comparison with the available gas phase yields a similar result. This shift is obviously due to the stronger interaction of C_{60} with water compared to Ne, but as this interaction affects both ground and excited state, it is hard to quantify this effect.

4.5 Astrophysical considerations

The spectrum shown in Fig. 4.1 and the band positions listed in Table 4.1 provide in principle - a tool to search for C_{60} embedded in water ice. The spectra presented here are recorded for 40 K, an astronomically relevant temperature, and provide a starting point with which to search for C_{60} : H_2O ice. It is likely that the fullerenes are not formed within the ice, but adsorb onto the grains during the accretion process (Berné & Tielens 2012). A solid state astronomical search for C_{60} : H_2O , using the rather characteristic pattern of the two strong bands C and E around $38\,753\text{ cm}^{-1}$ and $30\,618\text{ cm}^{-1}$, will be far from trivial, even in the case that C_{60} abundances are sufficiently high. The number of embedded objects with ice surroundings that can be observed in absorption is very limited and it should be noted that wavelengths below 300 nm are not accessible in ground based observations. Also, spectral overlap with electronic transitions of other species, e.g. PAHs, may exist. However, as has been proven in the past, e.g., for anions (McCarthy et al. 2006), the most effective strategy to search for new interstellar species

and the best way to figure out whether detection is technically feasible is by giving it a try. The present data provide the tools to do so.

Acknowledgments

This work has been realized within LASSIE, an interdisciplinary training network within the European Communitys 7th Framework Programme under grant agreement no. 238258.

Chapter 5

Lyman- α induced charge effects of PAHs embedded in ammonia and ammonia:water ice

Abstract. Infrared emission features assigned to gas phase polycyclic aromatic hydrocarbons (PAHs) are observed in space along many lines of sight. In regions where interstellar ices are present, these emissions are largely quenched. It is here that PAHs form agglomerates covered by ice or freeze out onto dust grains, together with volatile species such as H₂O, CO, CO₂, and NH₃. Upon exposure to the Ly- α dominated interstellar radiation field, PAHs are expected to participate in photo-induced chemical reactions, explicitly also involving the surrounding ice matrix.

In this paper, a systematic laboratory based study is presented for the solid-state behavior of the PAHs pyrene and benzo[ghi]perylene upon Lyman- α irradiation in ammonia and mixed NH₃:H₂O astronomical ice analogs. The results are compared to recently published work focusing on a pure water ice environment. It is found that the ice matrix acts as an “electronic solid-state switch” in which the relative amount of water and ammonia determines whether positively or negatively charged PAHs form. In pure water ice, cations are generated through direct ionization, whereas in pure ammonia ice, anions form through electron donation from ammonia related photoproducts. The solid-state process controlling this latter channel involves electron transfer, rather than acid-base type proton transfer. In the mixed ice, the resulting products depend on the mixing ratio. The astronomical consequences of these laboratory findings are discussed.

Cuyllé, S.H., Tenenbaum E.D., Bouwman, J., Linnartz, H., Allamandola, L.J.
Monthly notices of the royal astronomical society, **423**, 1825 (2012)

5.1 Introduction

The astrospectroscopic identification of individual polycyclic aromatic hydrocarbons (PAHs) has not yet been realized. Microwave spectra of gas phase PAHs are not available because they have, at best, weak permanent dipole moments. The transitions in those that do have permanent dipoles - arising from isotope or hetero-atom substitutions - suffer from severe band dilution due to the high partition function. The presence of PAHs in space, however, is generally accepted because of the observation of a set of strong infrared emission lines around 3.3, 6.2, 7.7, 8.6 and 11.2 μm that have been explained by PAH emission following UV excitation (Tielens 2008, and references therein). PAH mid-infrared emissions are observed along many lines of sight; molecular cloud edges, photodissociation regions, planetary nebulae and even in other galaxies, with the exception of dense clouds, where these features are quenched. Here, volatile molecules freeze out forming layers of ice on small dust grains (Pontoppidan et al. 2004; Öberg et al. 2010), providing a solid-state molecule reservoir. Subsequently, chemical triggers - photon irradiation and particle bombardment - drive solid-state reactions that have been shown in the laboratory to provide pathways towards molecular complexity in space (Fuchs et al. 2009; Öberg et al. 2009; Linnartz et al. 2011, and references therein). Less volatile species, such as PAHs are also expected to condense under these conditions. This effectively quenches the emission process upon UV excitation and explains the missing mid-infrared emission features in dense clouds. Indeed, in young stellar objects, observations indicate that PAHs likely exist in the solid phase, either as components of ice mantles, or as PAH conglomerates (Geers et al. 2009). Consequently, PAHs are also expected to participate in the solid-state chemical network that is responsible for the formation of larger organic compounds. Unfortunately, systematic laboratory studies focusing on this important process are largely lacking.

In-situ spectroscopic studies of PAHs in ice environments comprise mainly of infrared (Bernstein et al. 1999) and more recently optical work (Bouwman et al. 2009, 2010). Spectroscopic studies in the optical and in the infrared focusing on the UV induced PAH chemistry have been reported specifically for PAHs embedded in water ice (Bernstein et al. 2007; Bouwman et al. 2011a,b; Guennoun et al. 2011). Water is the most abundant constituent of interstellar ices and was shown in several recent studies to catalyze reactions (Öberg et al. 2010) and to promote cation formation (Bouwman et al. 2011a). In this work, we investigate to which extent a different matrix environment (pure ammonia or mixed with water) influences the ionization process. Ammonia was chosen since, after water, it is among the most abundant polyatomic interstellar molecules known. Past studies showed that ammonia is conducive to solid-state anion formation (Schutte & Khanna 2003). The study here is astronomically relevant, as mixed water-ammonia ice is widely present around young stellar objects (Bottinelli et al. 2010) and pure NH_3 ice has been found in planetary atmospheres such as that of Jupiter (Brooke et al. 1998; Baines et al. 2002; Wong et al. 2004).

5.2 Experimental

The measurements are performed with OASIS, our Optical Absorption Setup for Ice Spectroscopy that monitors PAHs and PAH reaction products upon UV irradiation *in-situ* and in real-time. Experiments are performed on two commercially available PAH molecules: pyrene (Py, $C_{16}H_{10}$, Aldrich, 99%) and benzo[ghi]perylene ($B_{ghi}P$, $C_{22}H_{12}$, Aldrich, 99%). The experimental procedure applied here is the same as used in Bouwman et al. (2009, 2010, 2011a). Ices are grown on a cryogenically cooled MgF_2 sample (40 K) window that is located inside a high-vacuum chamber ($P < 5 \times 10^{-7}$ mbar) by flowing a gas mixture of PAH and pure ammonia (Praxair, 99.96%, as commercially available) or mixed ammonia:water (milli-q, degassed with 3 freeze-pump-thaw cycles) from an external manifold. Pyrene vapor is created by heating solid pyrene inside a pyrex vial to $\sim 40^\circ$ C. $B_{ghi}P$ has a much lower vapor pressure and PAH vapor is created by warming $B_{ghi}P$ powder in a resistively-heated steel oven, affixed to the end of the gas deposition tube inside the vacuum chamber. In both cases, typical PAH:ice mixing ratios amount to approximately 1:5 000.

During ice growth, the ice thickness is monitored via interference fringes resulting from the reflection of a HeNe laser beam off the sample window. Typical ice growth rates amount to $75 \text{ nm minute}^{-1}$ and standard ices are calculated to be $\sim 1.3 \mu\text{m}$ thick, using an ammonia ice refractive index of 1.49 and a solid-state ammonia density of 0.86 g cm^{-3} (Romanescu et al. 2010). After deposition, the ice is illuminated with vacuum ultraviolet photons produced by a microwave-powered hydrogen discharge lamp that emits Ly- α photons ($\sim 121.6 \text{ nm}$) but also emits a broader band around 160 nm (Muñoz-Caro et al. 2002). The emitted light is directed towards the ice substrate through a MgF_2 window that also acts as a vacuum seal. The lamp flux at the substrate surface is $\sim 10^{14} \text{ photons cm}^{-2} \text{ s}^{-1}$ (Bouwman et al. 2011a, and chapter 2).

During an experiment, spectral properties are monitored in direct absorption, dispersing the light of an intense white light source (Xe-arc lamp) that is focused through the ice onto the slit of a broadband ANDOR Shamrock spectrometer. This system disperses light in the 300-815 nm region with a maximum spectral resolution of 0.55 nm. Before the vacuum UV exposure starts, a reference spectrum is taken to which subsequent spectra are compared. Negative peaks then correspond to species being consumed while positive peaks correspond to species newly formed. The spectra presented here are plotted in units of optical depth (O.D. = $\ln(I/I_0)$). Spectra are recorded for different ice temperatures between 12 and 80 K.

5.3 Results

5.3.1 PAH:NH₃ Ly- α photolysis

Fig. 5.1a shows a spectrum of Py:NH₃ ($\sim 1:5$ 000) ice at 40 K after 100 seconds of UV exposure. As was the case for Py in water ice (Bouwman et al. 2009), the negative absorption signal around 337 nm is due to Py consumption, but other spectral features clearly differ — both in wavelength and relative intensities — in the UV irradiated Py water dominated NH₃:H₂O 1:10 ice spectrum (Fig. 5.1c). Immediately after photolysis starts, positive signals at 381 and 487 nm grow. These features can be assigned to

the Py anion based on the work by Shida (1988). The identification is solidified by the same experiment conducted at 80 K (Fig. 5.1b), where the anion signal is more intense, also revealing weaker Py⁻ features reported by Shida (1988) at 448 and 461 nm.

Remarkably, PAH anion production is favoured by the NH₃ ice whereas PAH cation production is favoured by the H₂O ice. To test if this is a general trend, the UV photolysis of another PAH, B_{ghi}P, in NH₃ ice has been studied. Spectral data from the B_{ghi}P experiments are displayed in Fig. 5.2. Negative absorption bands at 366 and 385 nm gradually grow, hard to see at 40 K (Fig. 5.2a), but clearly visible at 80 K (Fig. 5.2b), signaling consumption of neutral B_{ghi}P (¹B₂). The latter is in correspondence with UV irradiation data found for B_{ghi}P in a NH₃:H₂O 1:10 ice (Fig. 5.2c), but again, the resulting reaction products differ from those in H₂O ice. A positive band at 541 nm corresponds to the B_{ghi}P anion (Shida 1988). As for Py, the 80 K experiment shows an improvement in S/N and allows the detection of other anion bands at 419 and 505 nm as well. For both PAHs: Py and B_{ghi}P, the neutral PAH signal loss and PAH-anion signal growth in ammonia ice are clearly weaker than the corresponding PAH-cation signals in water ice.

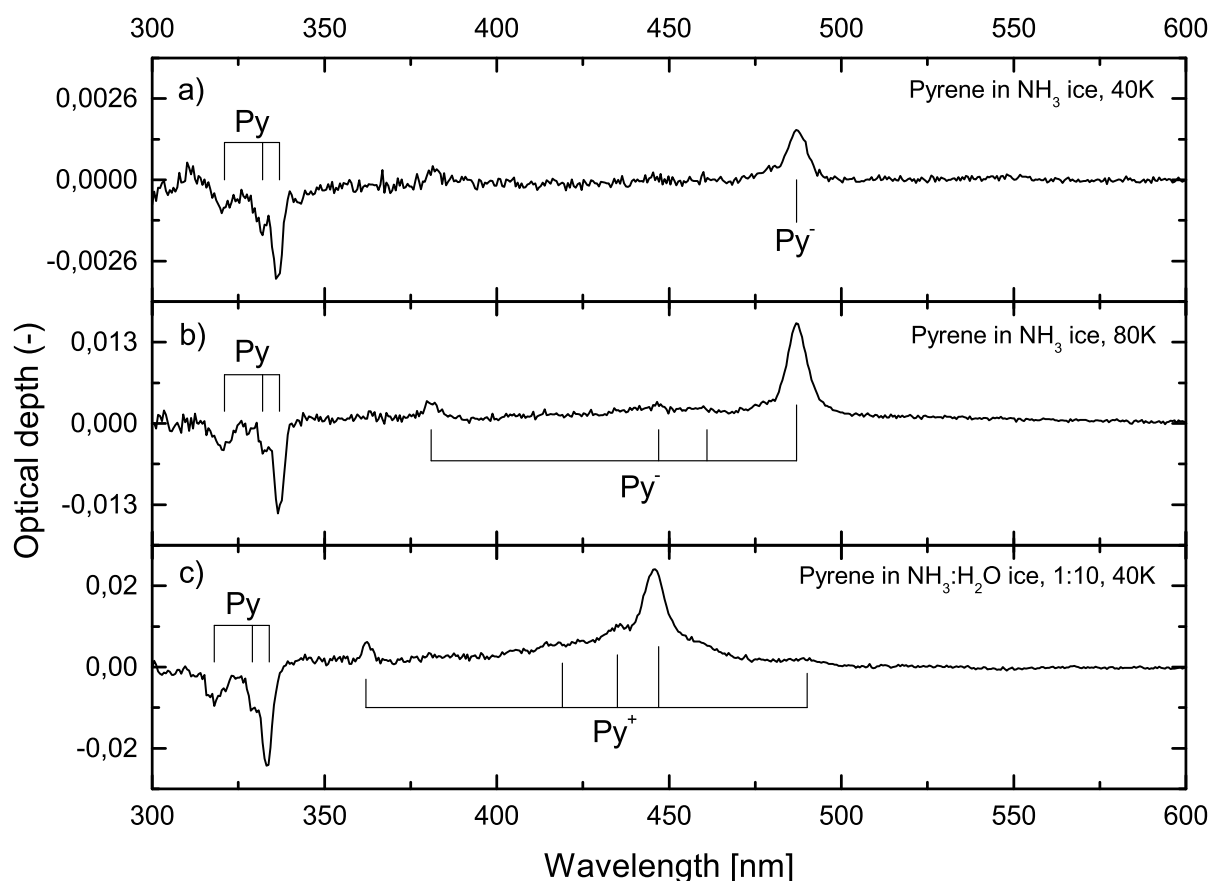


Figure 5.1 — Spectra of pyrene (C₁₆H₁₀) containing ammonia ice ($\sim 1:5\ 000$) acquired after 100 seconds of Ly- α exposure. Negative peaks indicate the consumption of the precursor molecule and positive peaks indicate the formation of new species a) Pyrene in NH₃ ice at 40 K, b) Pyrene in NH₃ ice at 80 K, c) Pyrene in NH₃:H₂O 1:10 ice at 40 K.

The influence of ice temperature is further explored in experiments performed at 12, 40, 55, and 80 K. At higher temperatures, both PAH anion formation and PAH neutral consumption are more efficient. For example, at 80 K, after 100 s of Ly- α exposure, the Py anion peak has an intensity of 0.014 O.D. units, while at 40 K the intensity is ten times less. This is in contrast with water based low temperature ice chemistry where the cation formation is largest for lower temperatures (Bouwman et al. 2010).

In Table 5.1, the spectroscopic data for PAH (anions) in NH_3 ice are summarized. The observed wavelengths for the band maxima are compared to literature values of corresponding transitions in other matrix environments. Typically, the PAH anion wavelengths in NH_3 ice are a few up to ~ 5 nm lower than in MTHF (2-MethylTetraHydroFuran) glass at 77K, and the PAH: NH_3 neutral peaks are 1.8-6 nm red shifted with respect to bands observed in a pure H_2O ice.

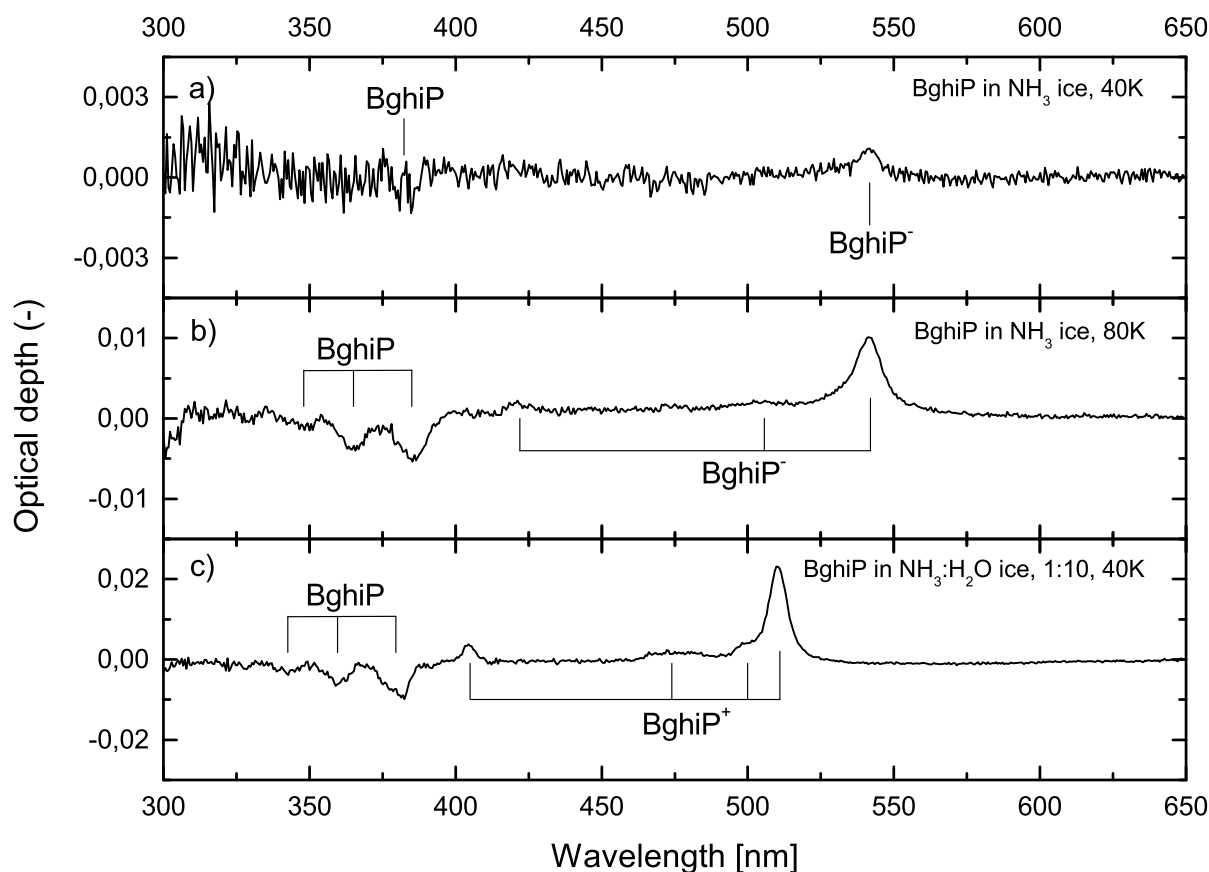


Figure 5.2 — As Fig. 5.1 for benzo[ghi]perylene ($\text{C}_{22}\text{H}_{12}$).

Table 5.1 — PAH transition wavelengths in NH_3 ice, H_2O ice and in MTHF matrices, with the strongest transition first.

Molecule	Transition	λ_{peak} in NH_3^1 (nm)	λ_{peak} in H_2O^2 (nm)	λ_{peak} in MTHF ³ (nm)
Py	$S_2(^1B_{2u}) \leftarrow S_0(^1A_g)$	337.0 (5), 333.1 (5), 320.8 (5)	334, 329, 319	-
Py ⁻	-	486.9 (5), 381.4 (5), 448 (4), 461 (2)	-	492, 383, 449, 463
$B_{ghi}P$	$S_2(^1B_2) \leftarrow S_0(^1A_1)$	384.7 (1.5), 366 (1)	380, 360	-
$B_{ghi}P^-$	-	541.2 (5), 419 (2), 505 (3)	-	545, 423, 505

5.3.2 PAH:H₂O/NH₃ UV photolysis

To compare the influence of a water or ammonia environment on the photochemistry in PAH containing ices, experiments have been performed on mixed H₂O:NH₃ ices. This is also a more realistic interstellar ice analogue, as in space (e.g., around young stellar objects), both water and ammonia are present in ices on cold dust grains, with typical NH₃ abundances with respect to H₂O ranging from a few up to 15 per cent (Bottinelli et al. 2010). Laboratory measurements are performed for different mixing ratios that cover these astronomically relevant values. In addition to the experiments for PAHs in pure water and ammonia ices, experiments have been performed at 40 K for ices with NH₃:H₂O mixing ratios of 100:1, 10:1, 5:1, 1:1 and 1:10. In all cases, the PAH:ice molecular ratio was kept at $\sim 1:5000$. The measurements allow one to determine the transition region for which the cation-generating chemistry that dominates in pure water ice, switches to anion-generating chemistry in pure ammonia ice. It is found that, as long as the water and ammonia amount are comparable, this switching point is not that well defined. The anion feature at 487 nm appears for samples with a NH₃:H₂O fraction of 1:1 or higher and the cation feature at 445.6 nm is observed in ices with a 1:1 or higher H₂O:NH₃ fraction. In the 1:1 NH₃:H₂O ice, both PAH anion and cation features are observed simultaneously as is illustrated in Fig. 5.3 for Py for irradiation times of 30 and 190 s. Nevertheless, the influence of the NH₃:H₂O ratio of the ice on the relative amount of anion formation, Py:Py⁻ is significant. Fig. 5.4 shows the anion feature at 487 nm, normalized with respect to the total Py abundance, at its maximum and for different ice compositions at 40 K. Compared to pure NH₃ ice (Fig. 5.4a), no significant difference is found in the 100:1 NH₃:H₂O ice (Fig. 5.4b), as may be expected. When increasing the relative amount of water in the ice to 10:1 NH₃:H₂O (Fig. 5.4c) the anion signal is halved. A further increase of the water fraction to 1:1 NH₃:H₂O (Fig. 5.4e) goes along with a further reduction of the anion signal. For a 1:10 NH₃:H₂O ice mixture (Fig. 5.4f), anion features are no longer observed. Instead, the spectrum is dominated by signals originating from PAH-cations and is not distinguishable from a spectrum of a vacuum UV irradiated PAH:H₂O ice (without NH₃).

5.3.3 Reaction products

A characterization of the PAH reaction scheme in the ammonia and ammonia:water ice, similar to the scheme derived for pure water ice (Bouwman et al. 2010), is not straightforward, because the anion signals are not very strong and no other photoproduct bands are evident. A number of possible PAH reaction products, however, can be ruled out or, at least, are of limited importance, based on the non-detection of known spectral features in the studied wavelength region. E.g., 1- and 2-aminopyrene have favorable electronic absorptions at 360 and 340 nm, respectively (Šoustek et al. 2008), neither of which are observed. An interesting result since amino substituted coronene has been detected using very sensitive mass spectroscopic techniques in coronene:NH₃ ice irradiation experiments (Bernstein et al. 2002). This difference likely arises from the somewhat lower sensitivity of optical spectroscopy. Another undetected species is monohydrogenated pyrene, which absorbs at 400 nm (Bouwman et al. 2010). Mono-deprotonated pyrene (the pyrenyl anion) can be ruled out based on theoretical pre-

dictions of a strong absorption feature in the 337-400 nm range (Hammonds & Sarre, private communication). It should be noted that the latter feature is at a higher energy than needed for electron detachment, so it may be that the pyrenyl anion does form but undergoes electron detachment before experiencing electronic excitation. While absorption from 2-aminopyrene and the pyrenyl anion could, in principle, overlap in wavelength with a pyrene absorption, the occurrence of this scenario is very improbable because the pyrene absorption feature retains its expected shape during photolysis. Smaller reactive species and products generated in the ammonia and water matrix must play a role, as both environments result in different final products. However, transitions associated with these remain undetected. For example, NH_2 has transitions throughout the visible region (Blindauer et al. 1993) and NH , absorbs at 337 nm (Langford & Williamson 1998), but both species are not observed, not even in a pure ammonia ice. Both species are very likely present in the ice, but their low oscillator strengths (~ 0.001 - 0.007) combined with line broadening due to matrix interactions likely prohibit a direct detection. For similar reasons, OH has not been observed in Ly- α irradiated H_2O ice (Bouwman et al. 2009).

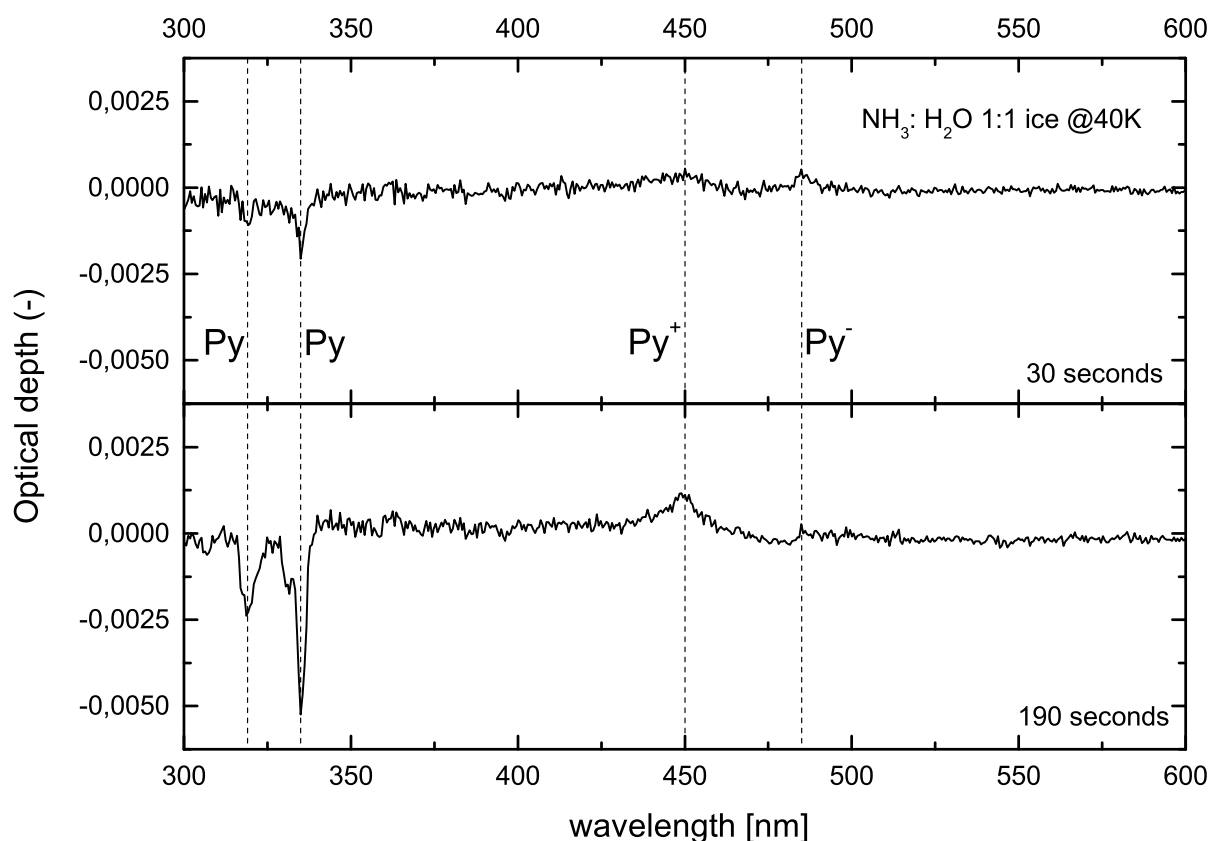


Figure 5.3 — Spectra of pyrene in a $\text{H}_2\text{O}:\text{NH}_3$ 1:1 matrix at 40 K under vacuum UV photolysis (30 s in the upper panel, 190 s in the lower panel). Indicated are the wavelengths of the anion feature in NH_3 ice, the cation feature in H_2O ice and the neutral features in NH_3 ice.

5.4 Discussion

5.4.1 NH_3 ice chemical process

While it is not possible to identify the reaction intermediates directly, the time (i.e., fluence) dependent behavior of the PAH precursor and resulting anion can be monitored, providing additional insight into the processes induced by the UV radiation. The upper panel in Fig. 5.5 shows the integrated $B_{ghi}P$ and $B_{ghi}P^-$ absorbance during continuous vacuum UV irradiation of $B_{ghi}P:NH_3$ ice. The anion signal increases and reaches a maximum after about two minutes and then slowly decreases. In parallel, the neutral precursor is consumed during the whole irradiation process. In the lower panel of Fig. 5.5, the UV irradiation is stopped after two minutes. The anion signal decreases relatively quickly now and, simultaneously, the neutral PAH signal increases; it is likely that PAH anion is converted into PAH neutral via a charge-exchange type of reaction with an electron acceptor in the ice. The ongoing chemical processes are schematically summarized in an effective reaction scheme shown in Fig. 5.6. The focus here is on empirical trends and not on absolute numbers.

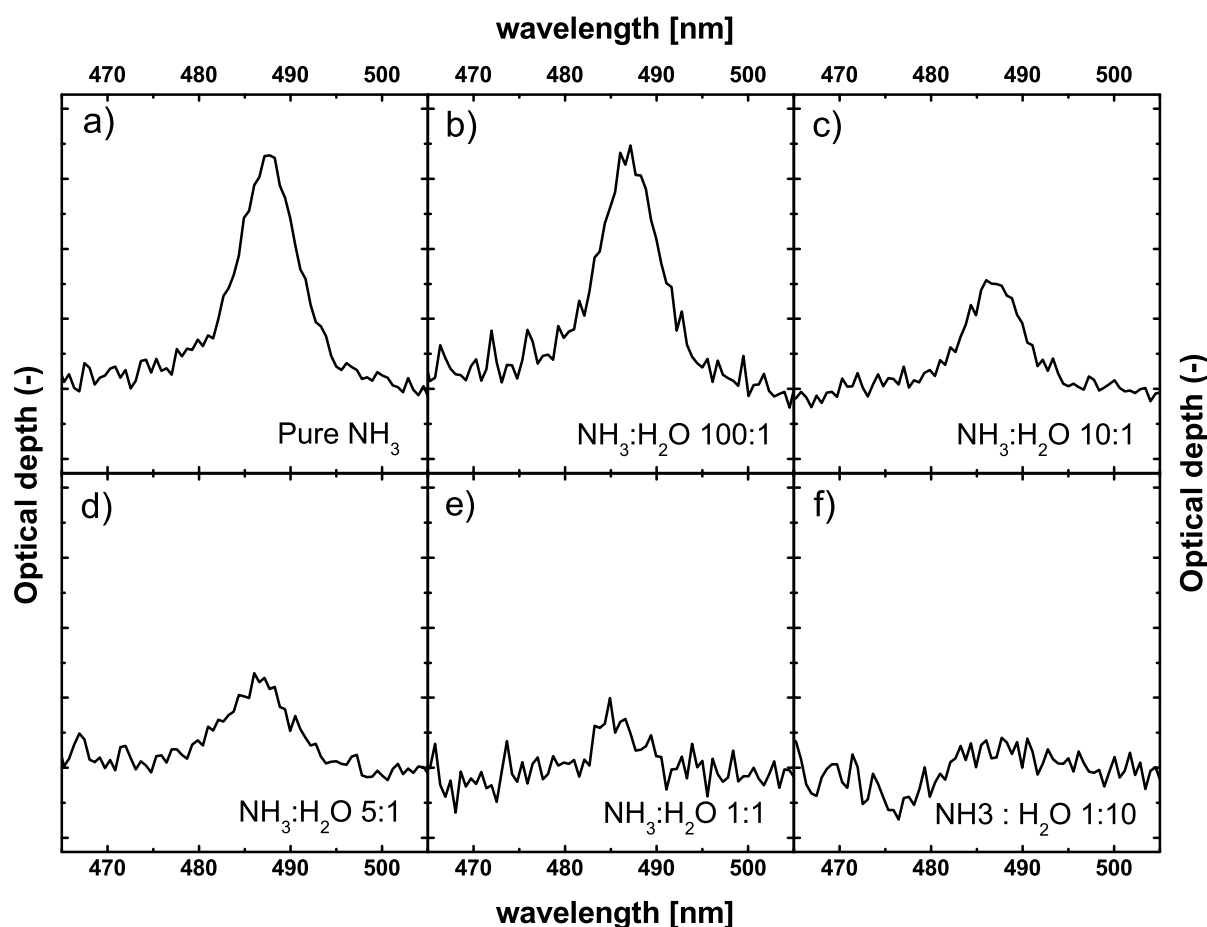
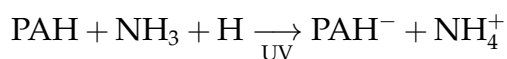


Figure 5.4 — Maximum strength of the Py^- feature for different ice compositions at 40 K, varying between pure ammonia and pure water ice: a) NH_3 , b) $\text{NH}_3:\text{H}_2\text{O}$ 100:1, c) $\text{NH}_3:\text{H}_2\text{O}$ 10:1, d) $\text{NH}_3:\text{H}_2\text{O}$ 5:1, e) $\text{NH}_3:\text{H}_2\text{O}$ 1:1, f) $\text{NH}_3:\text{H}_2\text{O}$ 1:10 (identical to H_2O).

In this scheme, the PAH anion acts as a steady-state reaction product. When photolysis is halted, the PAH⁻ peak disappears, as the k_{12} reaction continues, converting the PAH anion back into its neutral form. Another PAH⁻ destruction path, besides e^- loss, may also occur during photolysis (k_2), given the fact that the Py⁻ signal reaches a maximum and then decreases during ongoing irradiation. It is not possible to explicitly specify the resulting reaction products (P_2) because these are not visible in the spectral data (i.e., are not abundant enough to be observed, have low absorption strengths or absorb outside the accessible wavelength domain). Besides the conversion of PAH to PAH⁻, the neutral PAH may also be destroyed through another photo-induced pathway, k_1 , given the fact that in the ongoing irradiation experiment the neutral PAH signal decreases, even after the PAH anion formation signal stabilizes. Again, it is not possible to identify the products (P_1) of this pathway. Even the recent extension of the setup with a quadrupole mass spectrometer monitoring species desorbing from the ice during warm up, has not helped. As a consequence it cannot be excluded that P_1 is equivalent to P_2 and that the PAH anion is simply an intermediate in this conversion. Despite this lack of information on possible intermediates, it is likely that the k_{11} reaction involves a direct electron transfer from ammonia photoproducts to the PAH neutral. The observed higher PAH anion production at increased temperatures signals that the k_{11} reaction is enhanced when mobility of atoms or molecules in the ice is greater. Such a temperature effect is not *a priori* expected in a reaction involving the transfer of a free electron to a PAH molecule. The underlying reaction mechanism for k_{11} involves a PAH and electron donating photofragment, suggesting a net scheme:



where the hydrogen atom also originates from ammonia photolysis. It is probable that protonated ammonia, NH₄⁺, forms as a counter ion to the PAH anion. Infrared studies have shown the formation of NH₄⁺ in mixed ices containing ammonia. In ices that are exposed to vacuum UV photons, energetic electrons, high-energy protons, or even simple heating, ammonia acts as a base and accepts a proton from an acid, creating NH₄⁺ and a conjugate acid, as has been discussed for OCN⁻ and HCOO⁻ (Hudson et al. 2001; Novozamsky et al. 2001; Bennett et al. 2010; Moon et al. 2010). In the infrared, NH₄⁺ has been widely observed in interstellar ices (Schutte & Khanna 2003). In the optical regime, NH₄⁺ does not have absorption features. Complementary IR studies, therefore, are needed to further characterize the potential role of protonated ammonia in this reaction scheme.

Interestingly, while past studies showed ammonia-related ion formation in ices to be due to acid-base chemistry, the work presented here for PAHs reveals a different chemical process leading to the formation of PAH anions. These are found not to be produced by proton loss from the anion's parent molecule, as is the case for OCN⁻ (Hudson et al. 2001). Rather, PAH anions form through simple electron acceptance from ammonia-related donor molecules. Since PAH electron affinities increase with PAH size, with larger PAHs, it may be possible for this charge exchange to occur without energetic assistance.

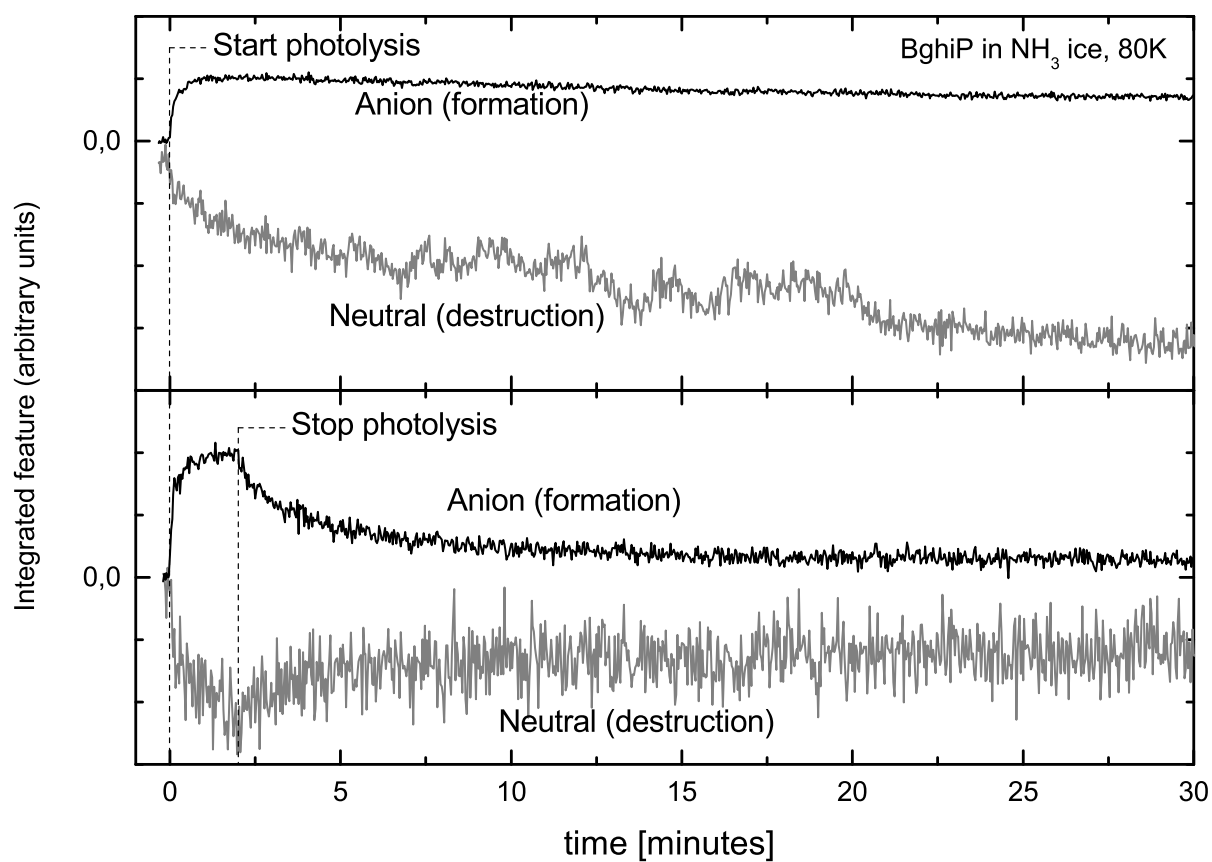


Figure 5.5 — Integrated $B_{ghi}P$ absorbance in NH_3 ice upon vacuum UV irradiation as function of time (i.e., fluence). In the upper panel the ice is irradiated continuously for 2 hours (only the first 30 minutes are shown). In the lower panel the vacuum UV irradiation is stopped after 2 minutes.

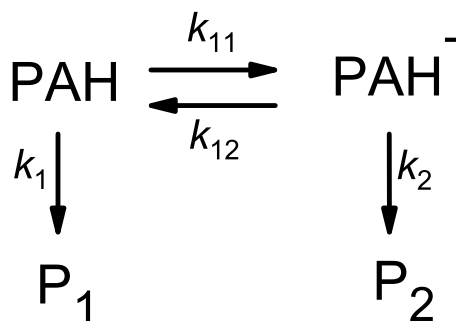


Figure 5.6 — Effective reaction scheme for vacuum UV irradiated $PAH:NH_3$ ice.

5.4.2 Ammonia vs. Water Ice

There is a clear difference between the behaviour of PAHs photolyzed in water versus ammonia ice. In H₂O ice, pyrene, coronene, anthracene, benzo[ghi]perylene, naphthalene, quarterrylene, and 4-methylpyrene are all converted to their monocationic, or dicationic (for quaterylene) forms upon exposure to vacuum UV photons (Bouwman et al. 2009, 2010, 2011a; Gudipati & Allamandola 2003, 2004, 2006b). The PAH⁺ molecules formed in water ice are highly stable and exist for days or longer, even after irradiation is stopped (Gudipati & Allamandola 2006a; Bouwman et al. 2009). In contrast, the PAH⁻ molecules formed in ammonia ice convert back to their neutral form in the first few minutes after the photolysis has stopped (Fig. 5.5, lower panel). Unlike in ammonia ice, where ~15% of the consumed PAHs are converted to their anionic form, in water ice, 30-100% of the consumed PAHs are converted to PAH⁺ within ~30 minutes of UV photolysis. Finally, during a long vacuum UV irradiation, H₂O:PAH ice undergoes complete conversion of the originally deposited PAHs, whereas in NH₃:PAH ice, only approximately 10% of the originally deposited PAHs are consumed. The cause for this contrasting efficiency is not *a priori* clear but may be due to different wavelength dependent absorption cross sections of NH₃ with respect to H₂O ice. Recently, it was shown that CO photo-desorption depends on the wavelength of the impinging radiation (Fayolle et al. 2011). As stated before, the discharge lamp also emits light around 160 nm where water ice is essentially transparent (Mason et al. 2006), but ammonia is not. The difference in photo-absorption cross section leads to different penetration depths of the vacuum UV photons in water versus ammonia ice. In ammonia ice, 99% of the incident photons will be absorbed at a depth of 0.55 micron (calculated from Mason et al. 2006). This is consistent with the partial destruction of originally deposited PAHs.

Another cause of the different behaviour observed in water and ammonia PAH-containing ices lies in the energetics of charged molecule chemistry. The electron affinities (EA) of Py and B_{ghi}P are 0.5 eV and 0.8 eV, respectively (Mallocci et al. 2005), comparable to those of the ammonia photoproducts NH (EA=0.38 eV; Al-Zaal et al. 1987) and NH₂ (EA=0.77 eV; Wickham-Jones et al. 1989). These EA values represent gas-phase calculations or measurements, but EA values in the solid phase can differ significantly, with changes on the order of 1-2 eV (Woon & Park 2004). The closeness between PAH, NH₂, and NH electron affinity values means that PAHs in photolyzed NH₃ ice are near equal competitors for free electrons with the other ice components (NH and NH₂). This is not the case in water ice, where the photoproduct OH has an electron affinity of 5 eV (Gudipati & Allamandola 2006a,b), making it a more favored electron acceptor than PAH molecules. Water ice itself is also a possible electron acceptor, with a theoretical EA of 2-3 eV (Gudipati & Allamandola 2006a,b). The electron affinity of ammonia ice has not been calculated or measured, but our results indicate that it is likely to be significantly smaller than that of water ice. Finally, experimental studies of electron transfer in solid ammonia and water at 20 K showed that water is much more effective at trapping electrons than ammonia (Lu & Sanche 2001). All these facts are consistent with a picture in which H₂O ice converts PAHs more efficiently into PAH⁺ than NH₃ ice into PAH⁻, in full agreement with the experimental observations.

5.4.3 Astrophysical Implications

NH_3 has been shown to be an important component of ices surrounding young stellar objects (YSOs). In a Spitzer survey of 41 low-mass YSOs, Bottinelli et al. (2010) detected solid-phase NH_3 in roughly half of the survey sample, with abundances relative to water ranging from 2-15%. Comparison of the NH_3 absorption maximum with laboratory spectra led Bottinelli et al. (2010) to conclude that ammonia is present in water-rich ice, as opposed to pure ammonia or CO/CO_2 rich ice. A VLT/Spitzer study by Geers et al. (2009) of PAH emission features in 53 low-mass YSOs found a systematic lack of PAH spectral signatures in almost all the objects surveyed. Geers et al. (2009) concluded that these non-detections are most probably due to PAHs being frozen in ice layers, or in coagulated form, quenching the typical infrared emission signatures. The results discussed here, particularly for highly diluted PAH abundances in $\text{NH}_3:\text{H}_2\text{O}$ 1:10 ice, are applicable to mixing rates observed in YSOs. The results indicate that under such conditions, PAH cations are likely to form. Following the experimental results found here for different water:ammonia mixtures, it is concluded that for a 10% ammonia abundance w.r.t. water, the PAH chemistry likely will be dominated by cation formation schemes. The laboratory data presented here may also be of interest to Jupiter's upper atmosphere, where clouds of NH_3 ice particles have been observed (Baines et al. 2002; Brooke et al. 1998; Wong et al. 2004) and small PAHs have been studied as a condensation point for aromatic haze (Biennier et al. 2011). While the actual NH_3 clouds are only seen covering 1% of the atmosphere, it is widely believed that the clouds cover the entire atmosphere but are obscured from detection by a coating of haze. Atreya et al. (2005) proposed that the obscuring haze coating is comprised of PAHs. The atmosphere of Jupiter is exposed to solar UV photons, and conditions therefore may, in principle, be favorable for solid-state anion formation.

In summary, the experiments described here show that the ice environment is of fundamental importance and determines which solid-state reactions take place. The ice matrix constituents determine which solid state reactions take place, the final charge may be positive or negative, depending on the relative amount of NH_3 to H_2O in the ice. This effect has been specifically studied for PAHs but represents likely a more generally valid effect, also determining the spectral appearance of other interstellar ice constituents.

Acknowledgments

This research is financially supported by the Netherlands School for Astronomy, the Dutch Organisation for Fundamental Research (FOM), NWO-VICI, the Dutch Organisation for Science, and the European Unions 7th Framework Programme (FP7/2007-2013) under grant agreement n.238258. E.D.T. acknowledges support from an NWO Rubicon Fellowship. L.J.A. gratefully acknowledges support from NASA's laboratory astrophysics and astrobiology programs.

Chapter 6

Photochemistry of PAHs in cosmic water ice - The effect of concentration on UV-vis spectroscopy and ionization efficiency

Context. Observations and models show that Polycyclic Aromatic Hydrocarbons (PAHs) are ubiquitous in the interstellar medium. Like other molecules in dense clouds, PAHs accrete onto interstellar dust grains, where they are embedded in an ice matrix dominated by water. In the laboratory, mixed molecular ices (not containing PAHs) have been extensively studied using Fourier transform infrared absorption spectroscopy. Experiments including PAHs in ices have started, however, the concentrations used are typically much higher than the concentrations expected for interstellar ices. Optical spectroscopy offers a sensitive alternative.

Aims. We report an experimental study of the effect PAH concentration has on the electronic spectra and the vacuum UV (VUV) driven processes of PAHs in water-rich ices. The goal is to apply the outcome to cosmic ices.

Methods. Optical spectroscopic studies allow us to obtain *in-situ* and quasi real-time electronic solid state spectra of two prototypical PAHs (pyrene and coronene) embedded in water ice under VUV photoprocessing. The study is carried out on PAH:H₂O concentrations in the range of 1:30 000 to pure PAH, covering the temperature range from 12 to 125 K.

Results. PAH concentration strongly influences the efficiency of PAH cation formation. At low concentrations, ionization efficiencies are over 60 % dropping to about 15 % at 1:1 000. Increasing the PAH concentration reveals spectral broadening in neutral and cation PAH spectra attributed to PAH clustering inside the ice. At the PAH concentrations expected for interstellar ices, some 10 to 20 % may be present as cations. The presence of PAHs in neutral and ion form will add distinctive absorption bands to cosmic ice optical spectra and this may serve as a tool to determine PAH concentrations.

Cuyllé, S.H., Allamandola, L.J., Linnartz, H.
Astronomy & Astrophysics, **562**, A22 (2014)

6.1 Introduction

Polycyclic aromatic hydrocarbon molecules are observed along many lines of sight through their UV pumped IR emission features in the 3.3 - 18 μm region (e.g. Draine & Li 2007; Tielens 2008, and references therein). However, within dense molecular clouds, volatile molecules freeze onto the low temperature (10 to 50 K) dust particles (e.g. Boogert et al. 2008, 2011; Ehrenfreund 2002; van Dishoeck 2008, and references therein) forming ice mantles around the dust grains. PAH molecules are expected to take part in this process causing them to become embedded in the ice mantles (e.g. Bernstein et al. 1999; Bouwman et al. 2009, 2011a; Gudipati & Allamandola 2003, and references therein). Over the past two decades, a handful of papers have attributed interstellar IR *absorption* features to PAHs frozen in the ices (e.g. Sellgren et al. 1995; Keane et al. 2001). The remarkable absence of PAH IR *emission* features from within molecular clouds is fully consistent with PAHs embedded in interstellar ices.

Careful observations coupled with dedicated laboratory experiments carried out for nearly 50 years have shown that the main constituent of interstellar ice is H_2O , with lower but substantial fractions of other volatile molecules such as CO , CO_2 , CH_3OH and NH_3 (e.g. Boogert et al. 2008, 2011; Ehrenfreund 2002; Pontoppidan 2004; Sellgren et al. 1995; van Dishoeck 2008, and references therein). Observations together with laboratory and theoretical studies (e.g. Bauschlicher et al. 2008, 2009; Steglich et al. 2011, 2012; Tielens 2008, and references therein) indicate that the PAH molecules observed in the gas phase contain about 50-100 carbon atoms effectively storing about 10 to 20 % of the cosmic carbon inventory. PAH abundances within the ice are estimated to be up to 2 % with respect to H_2O (Bouwman et al. 2011b, and references therein). Since PAHs are significantly larger than the known typical interstellar ice components and each PAH molecule contains at least an order of magnitude more carbon than other ice constituents, they are an extraordinarily important source of carbon in interstellar ices. Furthermore, as shown in many previous studies of non-PAH containing ices, *in-situ* energetic processing driven by e.g. UV photons, free atoms or electrons, results in a very extensive reaction network (Fuchs et al. 2009; Öberg et al. 2009, Chapter 2 and references therein). Also, PAH containing ices will be subject to photoprocessing, specifically Ly- α photons that are the result of H_2 emission after excitation by cosmic rays (van Dishoeck et al. 2006). It is therefore of fundamental importance to understand the role that PAHs play in water-rich ices both from a spectroscopic and chemical point of view.

To start providing this information, initial studies of solid state PAH-ice spectroscopy and Ly- α -dominated VUV photochemistry have focused on the behavior of single PAH types isolated in H_2O , CO , NH_3 or noble gas, low temperature matrices (Bernstein et al. 2005, 2007; Bouwman et al. 2010, 2011a; Gudipati & Allamandola 2003, 2006a; Guennoun et al. 2011; Sandford et al. 2004, and Chapter 5). These deliberate simplifications, focusing on single PAHs in a pure matrix environment, are not representative for realistic interstellar ices, but are an essential first step in characterizing spectroscopic features and understanding fundamental photochemical reaction networks unique to PAHs, particularly in relation to the dominant interstellar ice component, H_2O . The initial work of PAH photochemistry in water ice and water-rich ice mixtures took ad-

vantage of the great sensitivity of mass spectrometry. These studies were not *in-situ* studies, but rather focused on the non-volatile residual products, showing that PAHs undergo side group additions with the photofragments of the ice constituents (Bernstein et al. 1999, 2002).

Later *in-situ* studies followed, using two different techniques, each with both strengths and limitations. The first technique uses FTIR (Fourier Transform Infra-Red) absorption spectroscopy to observe the behavior of PAHs via their typical vibrational modes. Studying the photochemistry of the PAH pyrene (or coronene) suspended in argon and H₂O matrices (Guennoun et al. 2011), confirmed side group addition reactions upon VUV irradiation. However, when PAHs are frozen in water ice, the spectral overlap between PAH absorption features and ice matrix features, in combination with the relatively weak oscillator strengths of PAH vibrational transitions, requires high PAH concentrations in order to detect any PAH photoproduct bands. Even with this, at best, only a few of such bands can be detected and these are generally severely blended with very broad water features (Bernstein et al. 2007). The required concentrations are typically higher than $\sim 1:100$ PAH:H₂O and therefore not representative for interstellar conditions. The second technique, UV-vis (Ultraviolet-visible) absorption spectroscopy, was developed to overcome this limitation by taking advantage of strong PAH electronic transitions (Bouwman et al. 2009; Gudipati & Allamandola 2003). Small molecules (like H₂O, CO, NH₃) have, in contrast to PAHs and their ions, weak or no transitions in this spectral range. Taken together, these properties make it possible to record very clean optical spectra where only the strong, unique, and well-defined transitions related to the PAHs and their photoproducts are present, enabling one to track the UV-driven processes *in-situ* and in quasi real-time. The higher transition strength also facilitates the use of lower, astrophysically more relevant concentrations of PAH molecules in the ice matrix (typically $\sim 1:5\,000$ PAH:H₂O). UV-vis (hereafter also called optical) spectroscopic studies of irradiated ices have shown a very rich PAH ionization chemistry that is strongly dependent on matrix composition and temperature (Bouwman et al. 2011a; Gudipati & Allamandola 2003, 2006a, and chapter 5).

Reviewing the results of both methods, an interesting difference in observations appears. On the one hand, optical (low density/concentration) studies of PAHs in H₂O ice irradiated with VUV photons show that significantly more than 50 % of the neutral PAH molecules are readily converted into their cations while, on the other hand (higher density/concentration) IR studies show very limited PAH ionization. The greater sensitivity of optical spectroscopy to significantly lower PAH concentrations in interstellar ice analogs over IR spectroscopy make it ideally suited to investigate the effect PAH concentration plays in the spectroscopy and photochemistry of PAHs in water ice. Knowledge of the fundamental processes affected by PAH:H₂O concentration is essential before one can understand the role PAH concentration plays in interstellar ice chemistry. Since this seems to involve the interplay between ion-driven versus radical-driven processes, PAH concentration may play a very critical role in the energetic processing of interstellar ices. A systematic experimental study of this effect is presented here followed by an assessment of the astronomical implications.

6.2 Experimental method

The measurements for this study are performed with OASIS, our Optical Absorption Setup for Ice Spectroscopy, described in detail by Bouwman et al. (2009, and Chapter 2). It consists of a high vacuum chamber ($P < 3 \times 10^{-7}$ mbar) inside which a MgF_2 ice deposition window is suspended on the cold finger of a closed cycle helium cryostat. A Lakeshore 330 temperature controller holds the deposition window at the desired temperature in the range of 12 to 325 K using a resistive heater wound around the cold finger. The absolute temperature accuracy is better than 1 K.

The ice is grown on the cold window from H_2O vapor provided from an external glass bulb. The H_2O vapor is guided through a 6 mm diameter stainless steel tube ending at a distance of 20 mm perpendicular to the deposition window inside the chamber. Between the bulb and the deposition window, a leak valve is installed and used to control the H_2O deposition rate. The thickness of the ice is measured by laser interference using a HeNe laser (632.8 nm). This system comprises a photodiode to measure the intensity of the laser beam reflected off the growing ice and deposition window. A difference in path length between both reflections causes optical interference as the ice thickness increases, effectively modulating the photodiode signal intensity by about 20 % over time. This method of measuring ice thickness is routine (Bossa et al. 2012, 2014; Romanescu et al. 2010) and is, for our specific case, described by Bouwman et al. (2009). The ice thickness (t) is given by:

$$t = \frac{m\lambda_{\text{HeNe}}}{n_{\text{ice}}\cos\theta}$$

With 'm' being the amount of periods (or interference fringes) in the signal, λ_{HeNe} the wavelength of the HeNe laser, n_{ice} the refractive index of the ice (Romanescu et al. 2010) and θ the reflection angle, which in our case is 45 degrees. The density of amorphous solid water ice (Sceats & Rice 1983) combined with the ice thickness, allows one to determine the absolute column density of the matrix material. As the focus of the present study is on concentration effects, special care has been taken to perform these experiments as accurately as possible.

In this study, we embed coronene (Cor or $\text{C}_{24}\text{H}_{12}$) or pyrene (Py or $\text{C}_{16}\text{H}_{10}$), as prototypical PAHs in ice by co-deposition ensuring that the PAH: H_2O ratio remains constant over the full depth of the ice. Coronene is evaporated in an oven consisting of a small metal cannister attached to the end of the deposition tube inside the vacuum chamber and is heated by a resistive wire. The temperature of the oven is controlled by setting the current through the resistive wire; the temperature is not directly measured. Since pyrene has a higher vapour pressure than coronene, a lower sublimation temperature suffices. It is sublimed using an external glass vial attached to the matrix deposition tube. The vial is heated to 30 - 80 °C using a wire heater. The temperature is measured using a type K thermocouple and controlled by modifying the current through the heater. This heater is also wound around the deposition tube to prevent pyrene condensation inside the deposition tube.

During deposition and photolysis, the PAH molecules and their photoproducts in the ice are monitored simultaneously in quasi real-time using an optical spectrometer (Andor Shamrock sr-303). The white light of a LOT-Oriel Xe arc lamp passes through two irises and is focused on the deposition window. After the deposition window, the light passes through a third iris and is refocused onto the entrance slit of the spectrometer using a lens. A 150 lines/mm grating disperses the light onto a CCD with 1024 pixels providing a spectral coverage from about 230 to 700 nm in a single go with a spectral resolution of 0.55 nm. During the measurements, multiple spectra are taken and averaged to improve signal to noise levels. In practice, a new spectrum is generated every 10 s. The first spectrum is taken as a reference (I_0) to which all subsequent spectra are compared in units of optical depth (O.D. = $\ln(I/I_0)$). Besides measurement of the spectral data, the chamber pressure and window temperature are also recorded and stored. The spectra measured before and after photolysis are used to determine the column density of the PAH and reaction products in the ice. For each spectrum, the band area of individual features is integrated and the resulting column density is derived (Kjaergaard et al. 2000), following;

$$N_{PAH} = \frac{\int \tau_v d\nu}{8.88 \times 10^{-13} f}$$

Where N_{PAH} is the column density of the PAH molecules, $\int \tau_v d\nu$ the integrated band area and f the oscillator strength of the involved transition. Knowing the column density of both the ice and the PAH molecules or eventual photoproducts allows their concentration to be obtained with a time resolution of 10 s. Taking into account the reproducibility of these experiments, we estimate an accuracy of about 10%. From these data, the maximum ionization yield is determined by averaging the cation values of 5 spectra around the maximum ionization yield.

This study focuses on different concentrations of coronene (Aldrich, 97 %):H₂O (milli-Q, 3 freeze-pump-thaw cycles) deposited at 40 K, subsequently cooled or heated to 12, 25, 40, 80 or 125 K and VUV photoprocessed. A verification test with a similar concentration range is performed for pyrene (Aldrich, 99 %):H₂O (milli-Q, 3 freeze-pump-thaw cycles) deposited at 40 K and VUV processed at 12 K. The UV light is generated using a microwave powered H₂ discharge lamp producing 10^{14} photons cm⁻² s⁻¹ at the ice sample (Muñoz-Caro et al. 2002). The spectrum of the lamp consists mainly of Ly- α photons at 121.6 nm, but also a broadband emission centered around 160 nm.

Temperature dependent studies of PAH chemistry in water ice (Bouwman et al. 2011a; Gudipati & Allamandola 2006a) have shown that lower temperatures enhance the stability of PAH cations in the H₂O ice matrix. Performing the measurements at 12 K as a reference provides maximal signal to noise levels of the observed cation features. Besides being the lowest temperature attainable using the OASIS setup, 12 K is also near the lowest temperatures observed for interstellar ices. Measurements with coronene at higher temperatures are also performed and serve as a consistency check.

6.2.1 Controlling PAH concentration

Ices are grown with the aim to realize PAH:H₂O concentrations ranging from roughly 1:10 000, which is a typical value on the low end of the range for the OASIS setup up, to 1:100, the range where FTIR measurements are typically performed. The latter concentration is unusually high for the OASIS setup, requiring some challenges to be tackled. Increasing the column density of the PAH molecules in the ice has its limits as eventually a point is reached where the molecular absorption bands start to saturate, rendering the spectra useless. As a result of this limitation, the PAH concentration is mainly controlled through modifying the deposition rate of the H₂O matrix, while keeping the deposition rate and column density of the PAH within set limits. Using this method, Py:H₂O ices with concentrations in the range of 1:12 000 up to 1:80 have been successfully grown.

For ice thicknesses less than 400 nm, coronene presents a challenge as optical interference significantly deteriorates the baseline, degrading the reliability of the first series of spectra. Fortunately, this interference disappears as the ice becomes thicker. This effect does not occur when depositing very thin Py:H₂O ices. A workaround for the high concentration coronene experiments, therefore, is realized by growing an ice in two steps. The first step is to grow a pure water ice with a thickness of about 500 - 600 nm. On top of this pure water ice, a very thin layer of ice with the desired high concentration of coronene is deposited. This eliminates the interference effect and makes it possible to grow ices at high Cor:H₂O concentrations (1:1 000 and higher). This method also allows one to accurately verify the deposition rate. It should be noted, though, that pores in 40 K deposited ice (Bossa et al. 2012, 2014) or other differences caused by the deposition method may also influence the overall outcome, but a direct comparison between both deposition methods with a \sim 1:1 000 Cor:H₂O ice does not reveal any substantial differences. Our measurements at 12, 25, 40, 80 and 125 K are performed at concentrations ranging from \sim 1:30 000 to \sim 1:120 Cor:H₂O. Additionally, pure coronene is also deposited. An overview of all measurements is given in Table 6.1.

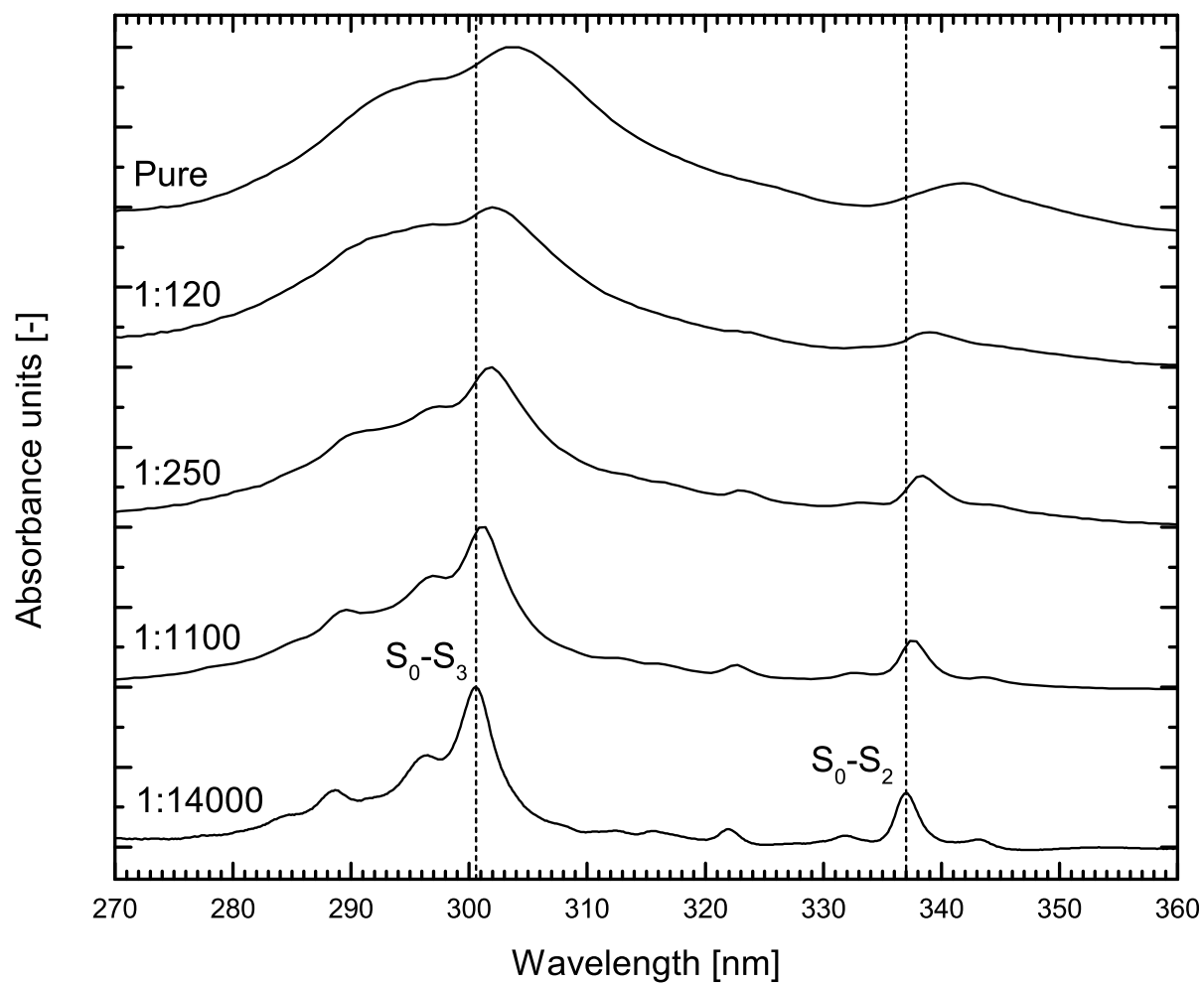


Figure 6.1 — The 270 - 360 nm absorbance spectra of Cor:H₂O ices at 5 different concentrations. All ices were deposited at 40 K. To aid comparison, all of the spectra are normalized to the peak of the $S_0 - S_3$ transition.

Table 6.1 — The different PAH:H₂O ice concentrations and temperatures studied here and the corresponding PAH photoionization yields. The relative error in both PAH concentration and ionization yield is 10 %.

		Coronene				Pyrene			
		25 K	40 K	80 K	125 K	12 K			
PAH:H ₂ O	yield	PAH:H ₂ O	PAH:H ₂ O	PAH:H ₂ O	PAH:H ₂ O	PAH:H ₂ O	yield		
1:14 000	0.63	1:16 000	0.66	1:14 000	0.65	1:29 000	0.32	1:12 000	0.43
1:1 400	0.11	1:5 000	0.38	1:1 100	0.06	1:1 200	0.03	1:3 600	0.31
1:1 100	0.12			1:900	0.08	1:800	0.0	1:800	0.14
1:250	0.03			1:400	0.02			1:400	0.11
1:120	0.0							1:80	0.09

6.3 Results

6.3.1 Coronene

The optical spectrum of coronene in H₂O ice can be directly compared to earlier noble gas matrix work (Ehrenfreund et al. 1992) and the observations of Cor:H₂O by (Bouwman et al. 2011a). Figure 6.1 shows the 270 to 360 nm region of the spectrum of coronene in water ices at different concentrations ranging from 1:14 000 Cor:H₂O to pure coronene, all deposited at 40 K. These spectra reveal two strong features at 300.5 nm and 337.0 nm, both accompanied by a multitude of weaker features, assigned by (Ehrenfreund et al. 1992) to, respectively, the S₀-S₃ and S₀-S₂ transitions of neutral coronene. Increasing the concentration of coronene from 1:14 000 to 1:1 100, 1:250, 1:120 Cor:H₂O and eventually pure coronene results in progressive spectral broadening and a ~4 nm redshift for both transitions as well as a significant increase in relative intensity of the higher vibronic bands with respect to the 0-0 band for the S₀-S₃ transition. In agreement with earlier observations (Bouwman et al. 2011a), photoprocessing of a ~1:14 000 Cor:H₂O ice at 12 K instantly reveals - besides a sequence of decreasing neutral coronene bands - the growth of spectral features in the 350 - 475 nm range with the strongest new band at 463 nm (Fig. 6.2). All new features can be assigned to the coronene cation based on the work by Bouwman et al. (2011a); Ehrenfreund et al. (1992) and Shida (1988). As in previous work, the oscillator strength of the coronene cation is derived by assuming a 1:1 conversion from coronene neutral to coronene cation during the first 100 s of photolysis. However, although the same method was used, due to a difference in integration range, an ambiguity between Ehrenfreund et al. (1992) and Bouwman et al. (2011a) and this study exists where different oscillator strengths are obtained. The measurement made by Ehrenfreund et al. (1992) covered the spectrum from ~430 nm, missing the short wavelength wing observed by Bouwman et al. (2011a). Ehrenfreund et al. (1992) states a FWHM of 2.8 nm resulting in a very narrow integration range of roughly ~454.8 nm to ~463.2 nm. This resulted in an absolute oscillator strength of 0.012. Bouwman et al. (2011a) observed an extensive short wavelength wing related to the coronene cation and used the very broad integration range of 389 to 473 nm resulting in $f = 0.23$. We also observed the long wavelength wing, although in some of our measurements, the cation feature appeared very weak causing the short wavelength wing to be indistinguishable from the baseline. It was therefore chosen to limit the integration range of our measurements to only the strongest peak. In practice, this resulted in an integration range from 456 nm to 469 nm giving an oscillator strength of 0.0278, the value used throughout this study. These results are consistent, as Bouwman et al. (2011a) obtained the highest oscillator strength using the largest integration range (84 nm), followed by our study, utilizing a narrower integration range (13 nm) resulting in a smaller oscillator strength and finally, Ehrenfreund et al. (1992) who obtained the smallest oscillator strength using the smallest integration range (<~8,4 nm). The relevant oscillator strengths are summarized in Table 6.2. Normalization of all data with respect to the total deposited coronene column density for each experiment enables the direct comparison of the photo-dynamics between different experiments. Fig. 6.3 shows the results for vacuum UV irradiated Cor:H₂O ice, illustrating the growth of coronene cation and loss of neutral coronene in the 12 (a-

d), 40 (e,f) and 80 K (g,h) ices for different concentrations. The left column in Fig. 6.3 (measurements at 12 K) clearly shows the strong influence concentration has on the coronene cation production efficiency. Raising the PAH concentration substantially decreases the maximum cation yield. The plots in the right column of Fig. 6.3 shows that this trend holds in higher temperature ices as well; an interesting result since it has already been shown that for higher temperatures the ion production efficiency is lessened (Bouwman et al. 2011a). Comparing the measurements at 12 K (Fig. 6.3 a to d) to those at 40 K (Fig. 6.3 e and f) reveals no major differences between both measurement series, however, the measurements at 80 K (Fig. 6.3 panels g and h) show that the coronene cation is only barely present in the ice at a concentration 1:1200, where it is clearly more abundant for similar concentrations at 12 and at 40 K. This is consistent with the observations from Bouwman et al. (2011a) on the temperature dependence of the ionization yield of PAHs in water ice. The PAH ion stabilization lifetime is strongly dependent on temperature, with the highest yields found at the lowest temperatures (Bouwman et al. 2011a; Gudipati & Allamandola 2006a, and Chapter 5).

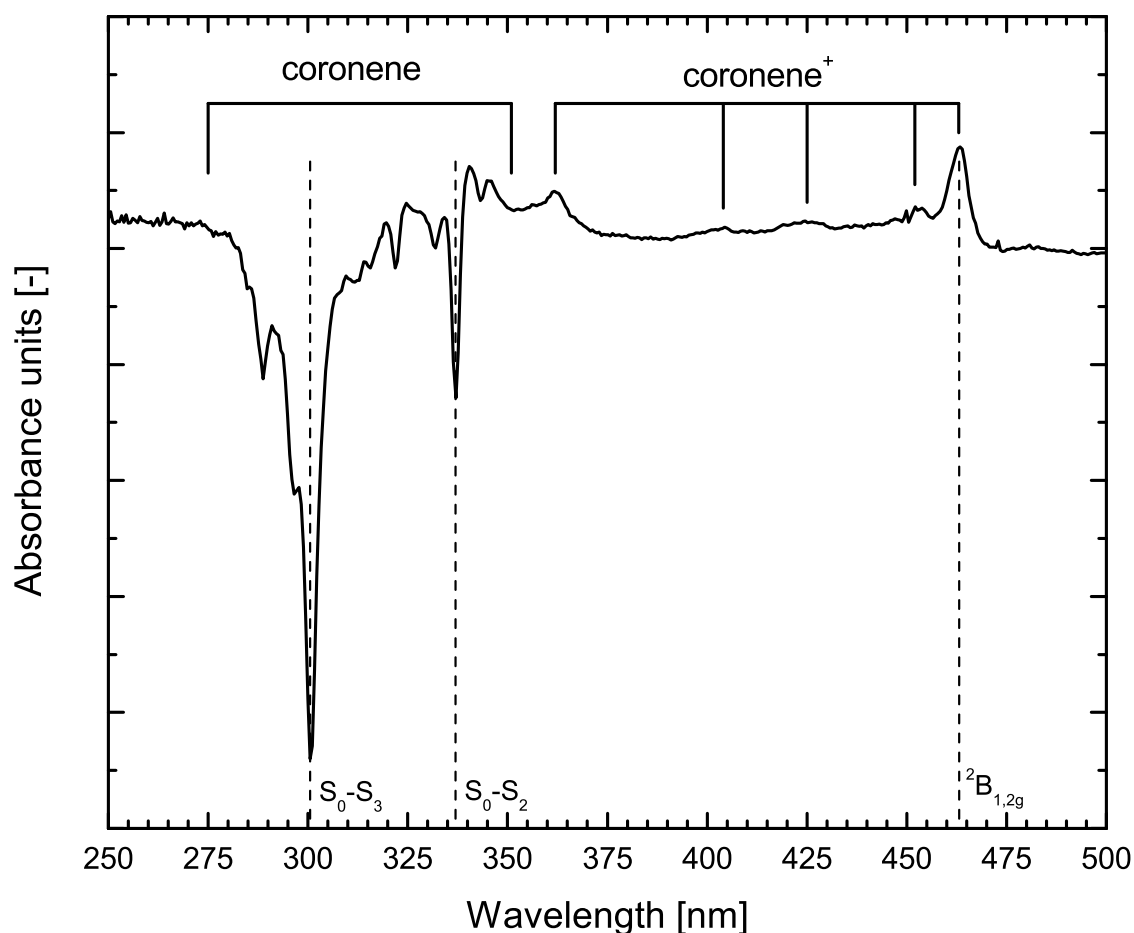


Figure 6.2 — The absorbance spectrum (I) of coronene in H_2O (1:14 000) at 12 K after ~ 12 minutes of vacuum UV photolysis referenced to the unphotolyzed spectrum (I_0), shown at the bottom of Fig. 6.1. Negative peaks indicate the loss of neutral coronene while positive peaks indicate the appearance of new photoproducts, in this case the coronene cation.

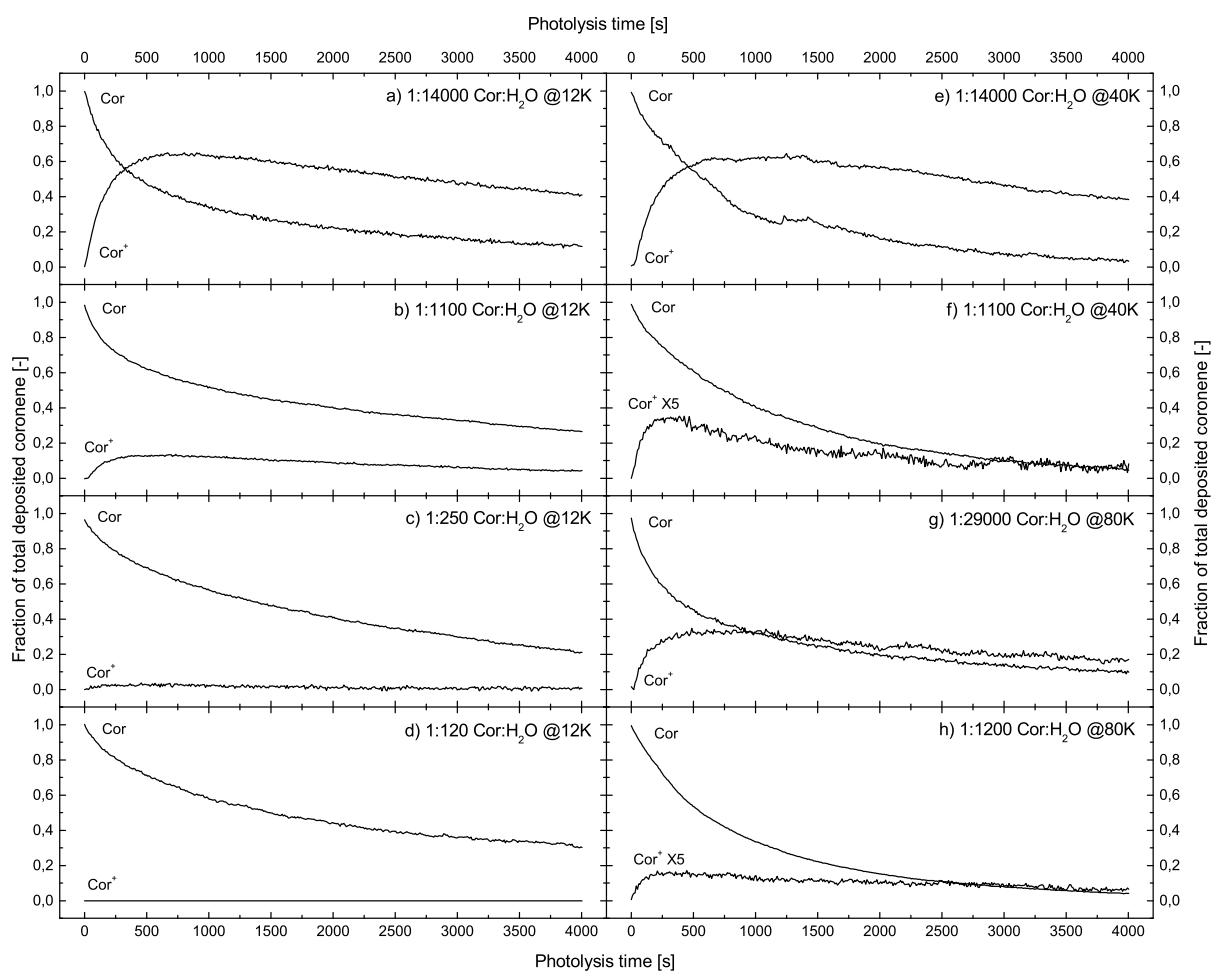


Figure 6.3 — The growth of Cor⁺ and loss of Cor at different concentrations and different temperatures, as function of VUV dose (photolysis time).

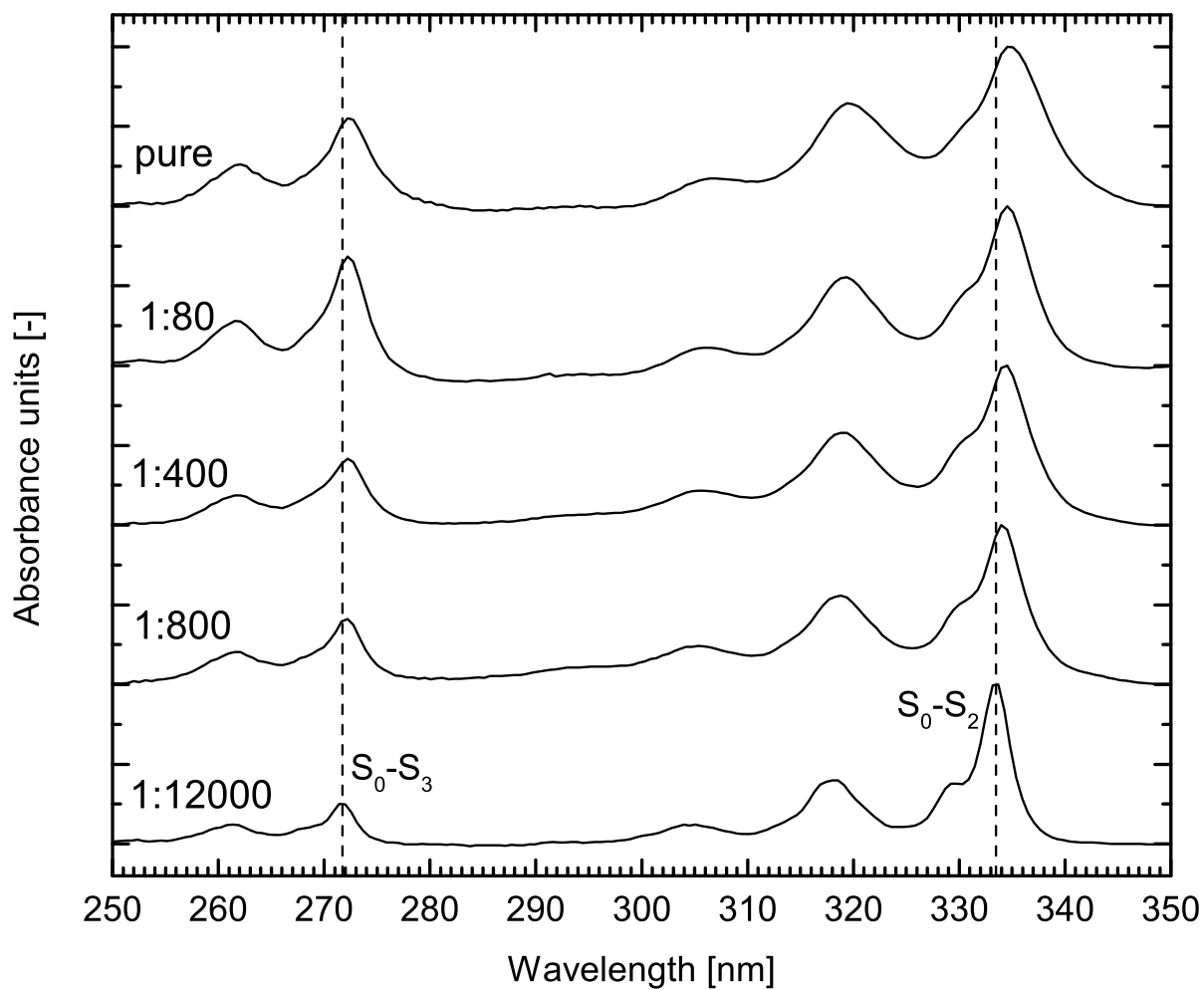


Figure 6.4 — The 250 - 350 nm spectra of Py:H₂O ices at 5 different concentrations. All ices were deposited at 40 K.

Table 6.2 — Oscillator strengths and transition assignments of the neutral and cation transitions of coronene and pyrene considered here.

	Coronene		Pyrene	
	Neutral	Cation	Neutral	Cation
Transition & peak	${}^1E_{1u}$: 301 nm ^a , ${}^1B_{1u}$: 337 nm ^a	${}^2B_{1,2g}$: 463 nm ^a	${}^1B_{2u}$: 334 nm ^b	2A_u : 446 nm ^c
Absolute f	$f=1.166^a$	$f=0.0278^d$	$f=0.33^b$	$f=0.104^d$
Feature range	275 - 350 nm	456 - 469 nm	285 - 349 nm	409 - 460 nm

Notes. ^(a)Ehrenfreund et al. (1992), ^(b)Bito et al. (2000), ^(c)Shida (1988), ^(d)derived here as described in Section 6.3.

6.3.2 Pyrene

The spectrum of neutral pyrene in a H₂O matrix shows a strong feature at 334 nm which corresponds to the 0-0 band of the ¹B_{2u}, S₀-S₂ transition, accompanied by weaker vibronic bands on the short wavelength side (Fig. 6.4) (Bouwman et al. 2009). When comparing the pyrene spectra deposited at increasing concentrations in H₂O, a slight broadening in combination with a small redshift becomes apparent (Fig. 6.4), however, both effects are less pronounced than for coronene. As with coronene, there is also an increase in relative intensity of higher vibronic bands with respect to the 0-0 band in only one of the two electronic transitions measured, but this time it occurs in the S₀-S₂ transition rather than the S₀-S₃ transition. Upon photolysis, a number of new features appear in the 350-470 nm range, most of which, can be assigned to the Py cation. This behavior has been extensively documented by Bouwman et al. (2010, 2011a, and Chapter 5) and is not further elaborated here. The strongest pyrene cation band falls at 446 nm and has been assigned to the ²A_u transition (Shida 1988). The oscillator strength of this Py cation band has been derived using the same method as described for coronene in section 6.3.1. Assuming a 1:1 conversion from pyrene to the pyrene cation during the first 100 s of photolysis results in an oscillator strength of $f=0.104$ for the 446 nm transition. In this case, band integration is performed from 409 to 460 nm. The maximum ionization yields for the concentrations studied here are listed in Table 6.1 and plotted in Fig. 6.6.

As with coronene, normalizing the spectra in each separate experiment to the total column density of the initially deposited neutral pyrene allows inter-comparison of the data from each experiment. Fig. 6.5 shows the loss of neutral pyrene and growth of the pyrene cation upon vacuum UV photolysis at 12 K for three different concentrations. The same overall trend as observed for coronene is apparent; the maximum cation ionization yield decreases as the pyrene concentration increases. However, there are also several small, but significant, differences between the ionization behaviour of coronene and pyrene. In contrast with coronene, Py cation growth continues (albeit slowly) or stabilizes at long photolysis times whereas it drops earlier with coronene. Additionally, overall ionization seems to be more efficient at higher concentrations.

6.3.3 Ionization efficiency

Fig. 6.6 shows the maximum ionization yields for all coronene:H₂O (and pyrene:H₂O at 12 K) measurements plotted versus their respective concentrations as listed in Table 6.1. There are two distinct regimes visible. The first is a rapid drop from the lowest concentrations (PAH:H₂O <1:10 000) to about 1:1 000 PAH:H₂O followed by a much slower (and fractionally smaller) drop with PAH:H₂O above 1:1 000. This illustrates, once again the concentration effect on solid PAH ionization efficiency.

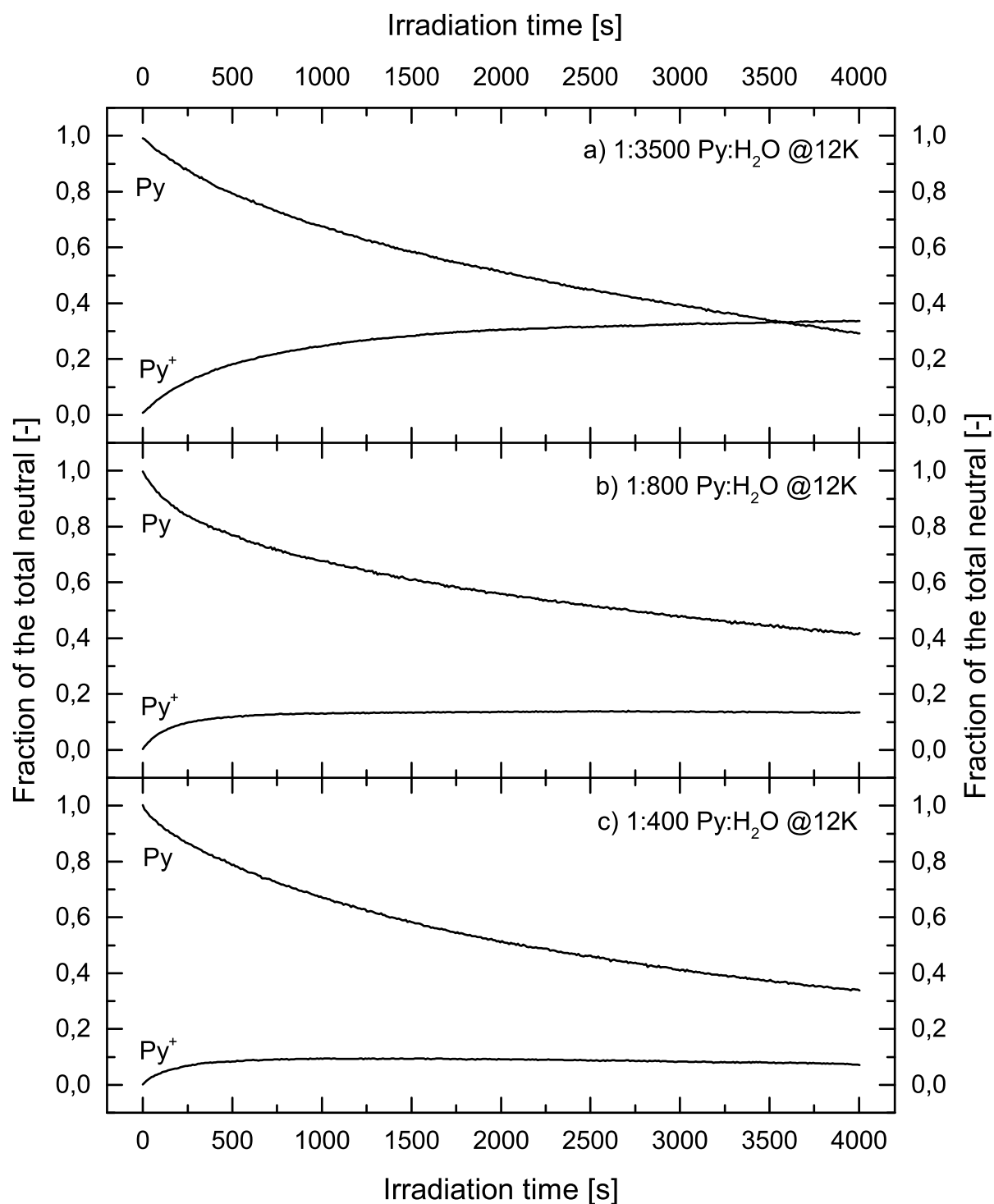


Figure 6.5 — The growth of Py⁺ and loss of Py at different concentrations and different temperatures, as function of VUV dose (photolysis time).

6.4 Discussion

Understanding the photochemical processes at play in both the ice and liquid forms of water remains an active area of research in its own right (Chipman 2011; Gillis & Quickenden 2001; Marsalek et al. 2011; Verlet et al. 2005, and references therein). In this section we restrict the discussion of the concentration effects presented above in terms of the factors that are likely to play dominant roles, namely PAH cluster formation, site geometry, ice micro-structure and PAH inter-molecular distance. Based on the overall, macroscopic physical and chemical PAH:H₂O ice environment, a rationalization of the concentration dependent behavior shown in Fig. 6.6 is presented subdivided into a low concentration and a high concentration regime. It should be noted that we do not aim to describe our observations at a molecular physics level, as this lies beyond the scope of the present paper.

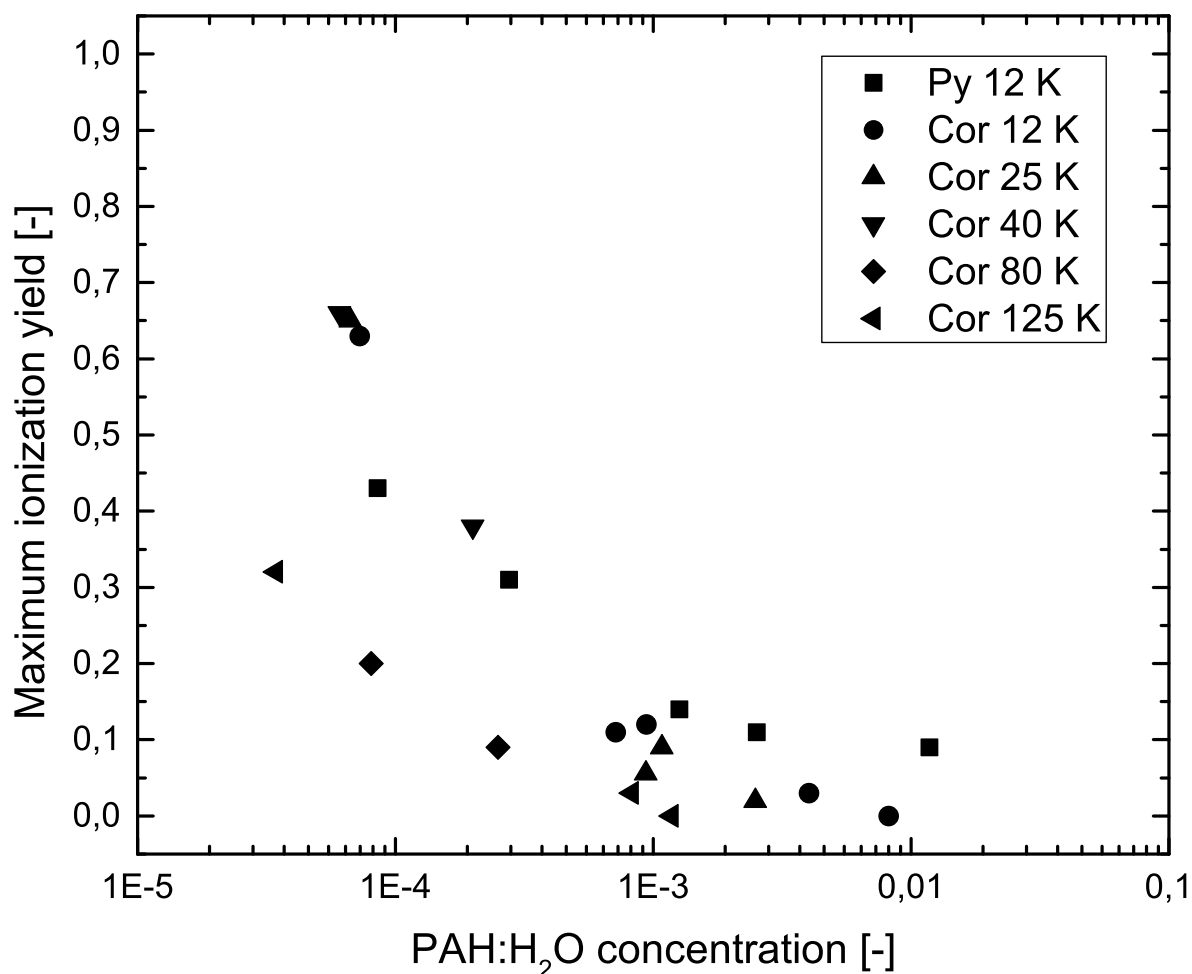


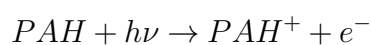
Figure 6.6 — Maximum ionization yield for different temperatures and concentrations of pyrene and coronene in H₂O matrix.

6.4.1 Low concentration regime (PAH:H₂O < 1:1 000)

The low concentration regime shows a drop in maximum ionization by half at concentrations of the order of 1:4 000, a range where the optical spectra do not reveal features related to PAH clustering in the ice as can be seen in Figs. 6.1 and 6.4. The most dramatic impact of clustering on the electronic transitions occurs when the PAH:H₂O ratio is well above 1:1 000. This is fully consistent with an IR spectroscopic study of PAH clustering behavior for the PAH naphthalene isolated in an argon matrix (Roser & Allamandola 2010). They found the onset of weak spectroscopic effects due to clustering in the CH stretching and CH out-of-plane bending modes at ratios above 1:1 000 and no evidence in the CC stretching region until concentrations exceed 1:500. Since these concentrations are far greater than those for which maximum PAH ionization drops precipitously, we conclude that PAH cluster formation is *not* responsible for the rapid decrease in maximum ionization yield with increasing PAH:H₂O concentration as shown in Fig. 6.6. Furthermore, the maximum ionization yields for both coronene and pyrene show a similar overall concentration dependence. Spectroscopic evidence shows that site geometry only plays a role at the concentration range where PAH isolation is no longer possible (PAH:H₂O is higher than 1:1 000). The geometrical size of coronene and pyrene significantly differ, and therefore likely require different numbers of H₂O molecules to isolate and stabilize their ion forms.

When assessing the influence of ice micro-structure and PAH concentration, it is important to recognize the critical role that water plays in interstellar ice astrochemistry (e.g. Öberg et al. 2010), overall ice structure and physical behavior (Bossa et al. 2012, 2014; Collings et al. 2005; Hawkins et al. 2005; Kumi et al. 2006; Malyk et al. 2007). The complex interplay between water molecules and charged small species embedded has been studied extensively using theoretical methods (Park & Woon 2004a,b; Woon & Park 2004, and references therein). From these studies, it was found that the number and orientation of the water molecules influence the ionization energies, potentially enabling auto-ionization in interstellar ices not containing PAHs. Most of these studies have focused on species of sizes, polarizabilities and dipole moments similar to that of water (Woon 2006, and references therein). PAHs are very different. They are much larger than water molecules, they have very large polarizabilities and pure PAHs have very small permanent dipole moments. The earlier experimental studies of PAHs in water ices demonstrated the ease and efficiency of PAH ionization and stabilization and the role of temperature on those processes. The resulting PAH ionization energy lowering, along with the concentration dependence described here show the critical and unique role water plays as none of these phenomena are observed in noble gas matrices.

In addition to the break up of H₂O molecules into H and OH upon VUV irradiation, another important early step in PAH photolysis is:



The electron affinity (EA) of water ice is estimated to be between 2 and 3 eV (Khan 2004;

Novakovskaya & Stepanov 2004) and the EA of the OH radical in ice is computed to be 5.06 eV. As long as the PAH concentrations are low enough, VUV irradiated water-rich ices provide ample sites that can trap electrons in 5 eV wells (Woon 2004). This, in combination with the added thermodynamic stability associated with the solvation energy of the isolated PAH cation in H₂O ice enables the stabilization of PAH cations in these ices, rather than electron recombination and neutralization. This effect appears very pronounced when comparing PAH ionization yields between low concentration H₂O matrices and low concentration noble gas matrices. The maximal ionization yield in H₂O matrices is reported to be higher than 50 %, while in noble gas matrices, they are typically only between 2 to 10 % (Hudgins & Allamandola 1995, 1997).

6.4.2 High concentration regime (PAH:H₂O > 1:1 000)

Increasing the concentration above 1:1 000 PAH:H₂O gradually reveals the spectral broadening and redshift in both the neutral and cation spectra (see Figs. 6.1 and 6.4). This phenomenon is related to PAH clustering in the ice. Indeed, increasing the PAH concentration reduces the average distance between PAH molecules, effectively increasing the recombination reaction channel and simultaneously decreasing the number of water related traps. In this reaction channel, an electron, freed upon VUV photolysis recombines with another PAH cation already present inside the ice matrix rather than undergoing a competing reaction channel. This is clearly more likely for concentrations in which the average distance between PAHs is small enough such that significant clustering occurs.

A further steady decrease of maximal ionization yield is observed until the point where a significant difference between both PAHs is apparent. Comparing the ionization fractions between pyrene and coronene, pyrene consistently has higher ionization fractions. The origin of this difference in behavior is not *a priori* clear as the effects of PAH clustering are not studied in detail. The type of clusters (parallel or perpendicular) and PAH size may play a role.

6.5 Astrophysical implications

PAH containing ices have not been identified in space yet. Infrared laboratory studies have been ambiguous, as different PAHs show similar spectra, because the typical vibrational modes involved are identical. However, unique electronic solid state spectra that have become available over the last years (Gudipati & Allamandola 2003; Bouwman et al. 2011a, and Chapter 5) provide laboratory data to realize the observational identification of PAH species in the optical domain. The focus of the present study is the reactivity of PAH containing ice. As with the earlier studies of the fundamental processes driven by the VUV photolysis of PAHs in water ice, the concentration studies reported here have important implications to our understanding of ices in astronomical objects of different types, ranging from icy bodies in the Solar System to the interstellar medium. This work presents the first detailed studies of the effect of concentration on PAH ionization efficiency in H₂O ice. We show that there is a clear link between PAH concentration and photoionization yield and thus, by implication, with the types of initial PAH photoproducts present in the ice that are available for

subsequent reactions and processes. Here we consider some of the possible implications regarding interstellar ices.

The behavior of ionization efficiency in H₂O ice falls in two distinct concentration regimes. At low PAH concentrations, ionization yield and stabilization is high, ranging from ~70 % at the lowest concentrations studied here to about 15 to 20 % at PAH:H₂O ~1:1 000, and reducing to a few percent for Cor:H₂O 1:250 and nearly 10 % for Py:H₂O 1:80. At higher concentrations, the drop off with increasing concentration gradually slows down, varying from 10 to 15 % for both pyrene and coronene at 1:1 000 reducing to no ionization for ~1:100 coronene. PAH concentrations with respect to H₂O in interstellar ices are estimated on the order of up to 2 - 3 % (e.g. Bouwman et al. 2011b; Keane et al. 2001; Sellgren et al. 1995). However, at this stage in our understanding, PAH concentration in interstellar ices can only be loosely defined and it is likely that the effective concentration from the perspective of the overall ice is lower. There are two main reasons behind this. First, interstellar PAH abundance is estimated from the intensity of the mid-IR emission features from mixtures of large PAHs (30 < C < 100) in the gas phase that are associated with UV rich regions. The PAHs studied here are much much smaller. Lower PAH concentrations in interstellar ices are required to satisfy the constraints imposed by cosmic C/H abundances. Second, there are other molecules in interstellar ices besides H₂O. The relative abundances of the molecules known to be present in interstellar ices are not given in percentages because the full molecular make-up of interstellar ices is unknown. It is for this reason that lists of the species comprising interstellar (and likewise cometary ices) are given with respect to H₂O, which is usually given a value of 100. Given typical interstellar ice compositions and relative abundances w.r.t. H₂O (roughly H₂O = 100; CO and CO₂ ~ 30 - 50; CH₃OH, H₂CO ~ 20 - 30; NH₃ ~ 5 - 15; etc.), it is clear that the total concentration of different PAHs in interstellar ices is very likely to be of the order of a few percent. We assume that the conclusions derived here for the concentrations of two individual PAHs can be used to describe the cumulative effect of a mixture of PAHs. Exact numbers, however, are not available. We do not want to exclude *a priori* a scenario in which the total PAH abundance is even lower, and in such an ultra-low domain we expect that a similar situation applies as for the processes described at low concentration, but less pronounced.

For the following, we conservatively adopt interstellar PAH:H₂O ice concentrations in the 0.1 - 0.5 % range i.e., 1:1 000 to 1:200, percentages that fall in the high concentration regime. These concentrations are lower than the 2-3 % PAH:H₂O concentrations derived by Bouwman et al. (2011b) and consistent with the values implied from Sellgren et al. (1995) and Keane et al. (2001). In this concentration range, PAH ionization occurs, with conversion efficiencies on the order of 10 - 20 %. Under these laboratory conditions, the maximum yield drops and further processing occurs. Under interstellar conditions, these processes are much slower. Combining the concentration dependence of the VUV processes described here with the astrophysical models of PAH freeze out and processing presented by Bouwman et al. (2011a), reinforces the conclusion that UV induced, radical driven processes such as PAH ionization processes could be important. The presence of ionized species within interstellar ices, or cosmic ices in general, and their roles in the chemical, physical and spectroscopic properties of these ices has not

been seriously considered. Since ion-mediated processes are so fundamentally different from the reactions normally considered for cosmic ice chemistry such as neutral-neutral (radical) reaction networks, the role of PAH ions as well as other ionized species should be included when modeling these ices. Support for the importance of ions in cosmic ices is provided by the 2165 cm^{-1} interstellar ice absorption band associated with high-mass protostellar regions. After a long controversy in the literature, this band has been assigned to OCN^- (Demyk et al. 1998; Novozamsky et al. 2001; Schutte & Greenberg 1997, and references therein). However, a long-standing problem associated with this is the identity of the counter cation or cations. Given all the evidence, the presence of PAH cations in these ices, in combination with other cations, such as NH_4^+ (Schutte & Khanna 2003), may provide part of the solution to this problem as well. Another important result of this work is that a significant amount of spectral broadening and intensity changes are observed in the optical bands. Beyond the normal matrix induced band broadening and shifting, an electronic state dependent vibronic band intensity increase occurs with respect to the 0-0 transition, as PAH concentration increases. If this effect is a general trend with PAHs and PAH mixtures, this has important implications for the detection and identification of PAHs in interstellar ices with similar concentrations. In such ices, the neutral PAH spectra can be broadened and redshifted by a few nm, effectively smoothing the spectra. Once optical solid state PAH detections have become possible, which currently is not the case but definitely a goal to aim at, this may offer a diagnostic tool to derive also the concentration of a specific PAH. Observationally, this will be difficult as broad features are hard to separate from the underlying continuum. Also, given that many different frozen PAHs are present, spectral blending may further complicate such efforts. The laboratory data to realize this, however, are now (getting) available.

6.6 Conclusions

This work reports the concentration dependent behaviour of the PAHs pyrene and coronene embedded in a H_2O matrix under VUV photolysis at different temperatures (12, 25, 40, 80 and 125 K). The study is based on UV-vis spectroscopic measurements of PAH: H_2O samples with concentrations ranging from 1:30 000 to 1:80 irradiated with a Ly- α light source. Two PAHs are considered in order to obtain a wide overview of the processes influencing the photoionization efficiency. The oscillator strengths of the PAH⁺ electronic transitions have been derived and used in a time dependent study to track the abundance of the respective PAH cations in the ice. The main conclusions from the experiments are:

1. PAH ionization in the water matrix upon VUV irradiation features two very distinct regimes governed by changing concentration. The first is a rapid drop from the lowest concentrations (PAH: H_2O <1:10 000) to about 1:1 000 PAH: H_2O , followed by a much slower (and fractionally smaller) drop with PAH: H_2O above 1:1000. This behavior is observed at different temperatures and with different PAHs suggesting this may be a general effect amongst PAHs.

2. At concentrations expected in interstellar ices, $\sim 10 - 20$ % of the PAH may be present as cations perhaps serving as part of the cation population needed to balance the OCN^- abundance.
3. The spectra of PAHs embedded in H_2O ice at concentrations of $\sim 1:1000$ and higher feature spectral broadening and redshift progressing with increased concentration. This effect is the result of the formation of small PAH clusters inside the ice matrix. In the interstellar medium where a multitude of PAH species are expected to be present, this effect might contribute to smoothing and blending of the optical absorption features, making PAH identification difficult.

Acknowledgments

This research is financially supported by the Netherlands School for Astronomy, NWO-VICI, the Dutch Organisation for Science, and the European Community's 7th Framework Programme (FP7/2007-2013) under grant agreement n.238258. L.J.A. gratefully acknowledges support from NASA's Laboratory Astrophysics and Astrobiology programs, NASA's Laboratory Astrophysics 'Carbon in the Galaxy' Consortium and NASA Ames Research Center's Exchange program with the Netherlands.

Chapter 7

UV photochemistry of solid acetylene: a multispectral approach

Abstract. Gas phase acetylene (C_2H_2) and polyynes ($H(-C\equiv C-)_mH$) are ubiquitous in the interstellar medium. However, astrochemical models systematically underestimate the observed abundances, supporting the idea that enrichment from the solid state takes place. In this laboratory based study, we investigate the role C_2H_2 plays in interstellar ice chemistry and we discuss the way its photoproducts may affect gas phase compositions.

C_2H_2 ice is investigated under vacuum ultra-violet (VUV) irradiation in its pure form as present in the atmosphere of Titan and in a water dominated ice as present on grain mantles in molecular clouds and on comets. In order to disentangle the photochemical network, a unique, complementary combination of infrared (IR) and ultraviolet-visible (UV-vis) spectroscopy is used.

From the experimental results, it can be concluded that the VUV-induced solid state C_2H_2 reaction network is dominated by polymerization resulting in the formation of polyynes at least up to $C_{20}H_2$ and larger polyyne-like molecules. At low temperatures, this process takes place very efficiently and hints for low barriers. When extending this reaction scheme to a water-rich environment, the dominant reaction products are CO and CO_2 but the simultaneous detection of polyyne like molecules is evidence that the reactions as observed in pure C_2H_2 ice persist.

From the spectroscopic evidence as presented in this laboratory study, it is concluded that the formation of polyynes upon VUV irradiation of interstellar ices is a process that may contribute to at least part of the observed gas phase enrichment in space.

Cuyllé, S.H., Zhao, D., Strazzulla, G., Linnartz, H.
Astronomy & Astrophysics, **570**, A83 (2014)

7.1 Introduction

Acetylene, C_2H_2 , has been found to be ubiquitous in the interstellar medium via gas phase detections in both emission and absorption, mostly around young stellar objects (Carr & Najita 2008; Lahuis & van Dishoeck 2000), as well as in molecular clouds (Lacy et al. 1989) and cometary comae (Mumma et al. 2003) indirectly supporting its existence in cometary ice. Pure solid state C_2H_2 has been found on Titan, both on the ground (Lara et al. 1996) and as ice particles in the atmosphere (Gudipati et al. 2011). In observational studies, it is used as a tracer for warm (100-1000 K) molecular gas (Sonnentrucker et al. 2007). Along many lines of sight, C_2H_2 gas phase abundances have been observed to be a few orders of magnitude higher than the predictions of cold-gas steady-state chemical models. Gas phase formation routes towards C_2H_2 are very slow leading to the conclusion that the enhanced abundances of C_2H_2 are likely due to sublimation from interstellar ices (Lahuis & van Dishoeck 2000).

The IR spectral features of solid state C_2H_2 are blended by much stronger features of H_2O , the dominant interstellar ice constituent (Knez et al. 2012). This makes direct observations of C_2H_2 in ices a major challenge, forcing observers to derive solid state abundances based on gas phase observations. Owing to the lack of a permanent dipole moment, gas phase C_2H_2 is radio-silent and therefore, its detection mainly relies on IR observations. From observations of warm gas in Cepheus A east, Sonnentrucker et al. (2007) derive abundances of C_2H_2 in interstellar ices of about 0.02 with respect to water. While in cometary comae (Mumma et al. 2003), fractions of 0.001 to 0.01 with respect to water have been derived. This makes C_2H_2 a small but non-negligible component of interstellar ices.

In chemical models, C_2H_2 is considered to be a starting point of a very complex gas phase photochemistry resulting in polymerization upon UV-induced dehydrogenation and addition reactions (Loison et al. 2014, and references therein). Linear carbon chain radicals have been detected in the surrounding environment of carbon stars (Cernicharo 2004) and are part of the UV haze in Titan's atmosphere (Gudipati et al. 2011, and references therein). The gas phase reaction pathways to the formation of carbon chain species have been studied well, which explains the variety of carbon chain species observed in space (Jolly & Bénilan 2008).

Laboratory research of solid state C_2H_2 is generally limited to its pure form (Compagnini et al. 2009; Strazzulla et al. 2002; Zhou et al. 2009), while in an interstellar environment, C_2H_2 is expected to be present in a water-dominated environment with UV photons as the main chemical trigger. Studies of the VUV-induced solid state C_2H_2 photochemistry, especially when embedded in water ice, therefore, provide vital information on solid state reactions yielding pathways towards molecular complexity in space.

In this paper, we present a systematic laboratory study of the VUV photochemistry of solid state C_2H_2 and C_2H_2 embedded in H_2O ice by a multispectral *in-situ* approach that combines Fourier transform infrared (FTIR) with UV-vis spectroscopy. The photoprocessing of the C_2H_2 ice is performed under conditions as in space, at low temperatures and VUV light that spectrally resembles the radiation field in dark clouds, i.e., light dominated by emissions from cosmic-ray-excited hydrogen.

7.2 Experimental

This study implements a stepwise approach to characterize the VUV photochemistry of C_2H_2 . The first step consists of embedding the C_2H_2 molecules in an inert environment. With increasing complexity, it becomes more challenging to characterize the underlying reaction scheme.

The inert environment is achieved by isolating the C_2H_2 molecules in an argon matrix with 1:100 concentration. Although not astrophysically relevant, this enables us to track the initial reaction products while limiting the chance of reactions with radicals present inside the matrix. The second step consists of irradiating a pure C_2H_2 ice allowing reactions between C_2H_2 molecules and their photoproducts to take place. This results in a more complex reaction scheme since the radicals as detected in the argon matrix can recombine and form new, larger molecules. In the final step, a mixed $C_2H_2:H_2O$ ice is grown and VUV-photoprocessed.

In all these experiments, a multispectral approach is employed to detect the photochemical products, by combining two distinct *in-situ* spectroscopic techniques: UV-vis spectroscopy and FTIR spectroscopy.

UV-vis spectroscopy relies on the observation of electronic transitions in the 220 - 700 nm range. These transitions are typically very strong and molecule specific, facilitating identification of species present in concentrations of 1:10 000 and even lower, thereby enabling the detection of molecular species present in very low abundances. Moreover, matrix material (such as water) does not absorb in this domain and this helps in identifying spectral features of new reaction products. These, however, may overlap, hampering unambiguous identifications.

FTIR absorption spectroscopy enables us to observe the vibrational transitions, leading to a wealth of spectral features guiding identification of a multitude of reaction products present in sufficient abundances. The signal-to-noise ratio typically requires species to be present in a 1:100 fraction in order to identify them. These features may also overlap, specifically because comparable vibrational modes of different species may have rather similar absorption energies. Moreover, matrix material (specifically water) also absorbs in this range. Consequently, typically high concentrations are needed for detection. This is also the case for $C_2H_2:H_2O$ ices. Spectral overlap exists between C-H and O-H stretching and other modes, while the IR intensities of H_2O are orders of magnitude higher than that of C_2H_2 (Knez et al. 2012). As a result, to detect C_2H_2 in a water environment using our setup, a ratio of 1:10 or higher is required. This requirement fixes the concentration used throughout the experiment, but it should be noted that in an astrophysical environment, the C_2H_2 abundances are lower.

In our laboratory, both measurement methodologies are implemented in two distinct setups. The measurements using UV-vis spectroscopy are performed using our optical absorption setup for ice spectroscopy (OASIS), while the infrared absorption spectroscopic data are obtained using a FTIR high vacuum (HV) setup. The ice temperature of 12 K is used throughout all experiments as it is towards the lower limit of temperatures in interstellar ices that are in the range of 10 - 50 K (Boogert et al. 2008, and references therein). Additionally, the desorption temperature of argon is around 35 K requiring the use of temperatures sufficiently below that point to prevent unwanted desorption.

7.2.1 OASIS

OASIS has been described in detail in Chapter 2 and Bouwman et al. (2009). It consists of a high vacuum chamber ($P; 3 \times 10^{-7}$ mbar) inside which a MgF_2 ice deposition window is suspended on the cold finger of a closed cycle helium cryostat. A Lakeshore 330 temperature controller holds the temperature of the deposition window at the desired level in the range of 12 to 325 K with an absolute accuracy of better than 1 K, using a resistive heater.

The ice material is provided in the gas phase from an external glass bulb. It is guided through a 6 mm diameter stainless steel tube ending at a distance of 30 mm perpendicular to the deposition window inside the chamber. Between the bulb and the deposition window, a leak valve is installed and used to control the deposition rate. The thickness of the ice is monitored by measuring the interference pattern of a HeNe laser beam reflected off the ice surface and the deposition window while the ice grows. The ice growth causes a pathlength difference between the two reflections, yielding optical interference and modulating the intensity by $\sim 20\%$ over time. This method of measuring ice thickness is routine, (Romanescu et al. 2010; Bossa et al. 2014) and for our specific case, it has been described by Bouwman et al. (2009). The ice thickness information is used to guarantee reproducible conditions between different measurements. The interstellar UV field is simulated by a microwave-powered H_2 discharge lamp that mainly produces Ly- α photons at 121.6 nm with a broadband emission centred on 160 nm (Chen et al. 2014). This lamp is shared between both experimental setups for optimal consistency between the measurements. The operational pressure of the H_2 lamp is kept constant at 0.4 mbar. The absolute UV photon flux is calibrated using O_2 actinometry as described by Cottin et al. (2003). This mechanism involves the formation of O_3 upon the photoirradiation of O_2 ice for which the yield is known (Cottin et al. 2003). Cottin et al. (2003) propose a correction factor of 3.1 to take the difference in yield between the gas phase values as obtained by Okabe (1978) and the actual solid state value into account. This factor is used in this calibration. The O_3 column density is derived from the strong O_3 absorption feature centered at 259 nm which has an absorption cross section of 6×10^{-17} cm^2 molecule $^{-1}$ (Jones et al. 2014). In the present OASIS experiment, this method yields a VUV photon flux of $7.9 \pm 1.6 \times 10^{12}$ photons cm^{-2} s^{-1} at the sample with a distance of 152 mm from the lamp to the deposition window. It should be noted that this UV flux value is lower than values mentioned earlier by Bouwman et al. (2009) and Chapter 5. This results from a combination of window degradation with time and a possible overestimation of the photon flux in earlier reported studies.

During photoirradiation, the ice is monitored in quasi real time using a UV-vis spectrometer (Andor Shamrock SR-303). The white light (200 - 800 nm) of a Xe arc lamp (LOT-Oriel) passes through two irises and is focused on the deposition window. The transmitted light passes through a third iris and is refocused onto the entrance slit of the spectrometer. With a 150 lines/mm grating the light is dispersed onto a CCD detector with 1024 pixels, providing spectral coverage from about 210 to 700 nm with a spectral resolution of 0.55 nm. The spectral resolution can be improved at the expense of spectral range by using a different grating. During the measurements, multiple

spectra are taken and averaged to improve signal-to-noise. In practice, a spectrum is generated every 10 s and is the result of averaging 112 exposures. The first spectrum is taken as a reference (I_0), with which all subsequent spectra (I) are converted in absorbance scale (absorbance = $\ln(I/I_0)$). The chamber pressure and window temperature are also recorded and stored.

7.2.2 The FTIR HV setup

The FTIR HV setup (Gerakines et al. (1995) and Bouwman et al. (2007)) consists of a high vacuum chamber ($P; 1 \times 10^{-7}$ mbar) inside which a KBr ice deposition window is mounted on the cold head of a closed cycle helium cryostat. The temperature of the deposition window can be controlled between 12 and 325 K with 1 K absolute accuracy by a Lakeshore 330 temperature controller. The temperature is controlled through a wire heater wound around the cryostat cold head and kept at 12 K. The ice matrix is provided from an external glass bulb connected to a stainless steel 6 mm diameter deposition tube ending perpendicular to the deposition window at a distance of ~ 50 mm.

The ice is monitored during deposition and VUV irradiation using a varian FTIR spectrometer with a spectral range of 500 - 4000 cm^{-1} and 0.5 cm^{-1} spectral resolution. During deposition, the spectrometer is operated in direct mode and provides a new spectrum every three to four seconds. During VUV irradiation, 256 scans are added, requiring ~ 15 minutes to generate a spectrum with a substantially improved signal-to-noise ratio.

The interstellar UV field is simulated by the aforementioned H_2 discharge lamp. Its VUV flux is determined on OASIS and the only difference between both setups is the distance from the lamp to the deposition window. The VUV flux can therefore be determined by applying the square law with distance to the deposition window. In this setup, the distance between the lamp and the deposition window is 56 mm yielding a distance ratio of 2.66. This yields a flux of $5.6 \pm 1.1 \times 10^{13}$ photons $\text{cm}^{-2} \text{s}^{-1}$.

7.2.3 C_2H_2 matrix material

Three different gas samples are used to prepare the ice matrices. The first sample is obtained starting from purified welding gas which is C_2H_2 mixed with acetone ($\text{C}_3\text{H}_6\text{O}$). These gas components can be separated by using the difference in sublimation temperatures. The purity of the resulting C_2H_2 is checked in OASIS by a quadrupole mass spectrometer and in the FTIR HV setup from the IR spectrum. In both cases, neither acetone nor any other pollutants are observed, resulting in less than 0.1 % impurities. This sample is the basis for the 1:10 mixture with H_2O . In this mixture, the H_2O (milli-Q) has been subject to three freeze-pump-thaw cycles prior to mixing in a glass mixing line. The second sample of pure C_2H_2 starts from a commercial mixture of C_2H_2 :He (1:100) with purity 99.2 %. Helium does not freeze onto the deposition window at 12 K while C_2H_2 does. This way, a nearly pure C_2H_2 ice can be grown, which is confirmed by the FTIR deposition spectra. Finally, the Ar: C_2H_2 measurements are performed by depositing a commercial 1:100:100 C_2H_2 :He:Ar mixture with purity 99.2 %. In this way a 100:1 Ar: C_2H_2 ice is obtained providing the C_2H_2 isolated in an argon matrix.

7.3 Results and discussion

Fig. 7.1 shows the FTIR deposition spectra for all three samples. In the upper panel, C_2H_2 is embedded in an argon matrix, in the middle panel, pure acetylene is shown and the lower panel shows acetylene in water ice. Consistent with Knez et al. (2012), the spectra of C_2H_2 are dominated by three strong peaks and several weak features. The three strongest features are the ν_3 C-H stretching mode around 3240 cm^{-1} , the ν_5 C-H bending mode around 760 cm^{-1} , and the $\nu_4 + \nu_5$ combination mode around 1370 cm^{-1} . Among the three spectra, the C_2H_2 features shift by a few tens of cm^{-1} owing to the different matrix environments. The lack of water or any other features in the top and middle spectra proves the high purity of the samples. When using the 1:10 mixture, the strong overlap between spectral features of C_2H_2 and H_2O results in water dominating the spectra. The bands related to C_2H_2 appear as a small superposition on the very strong and broad water bands. A summary of the features observed in the deposition spectra can be found in Table 7.1.

Trace amounts of H_2O are present inside the setup and become visible with time when water gradually deposits on top of the ice. This adds a baseline to the IR spectra, and may upon VUV irradiation have a chemical interaction with the top ice layer.

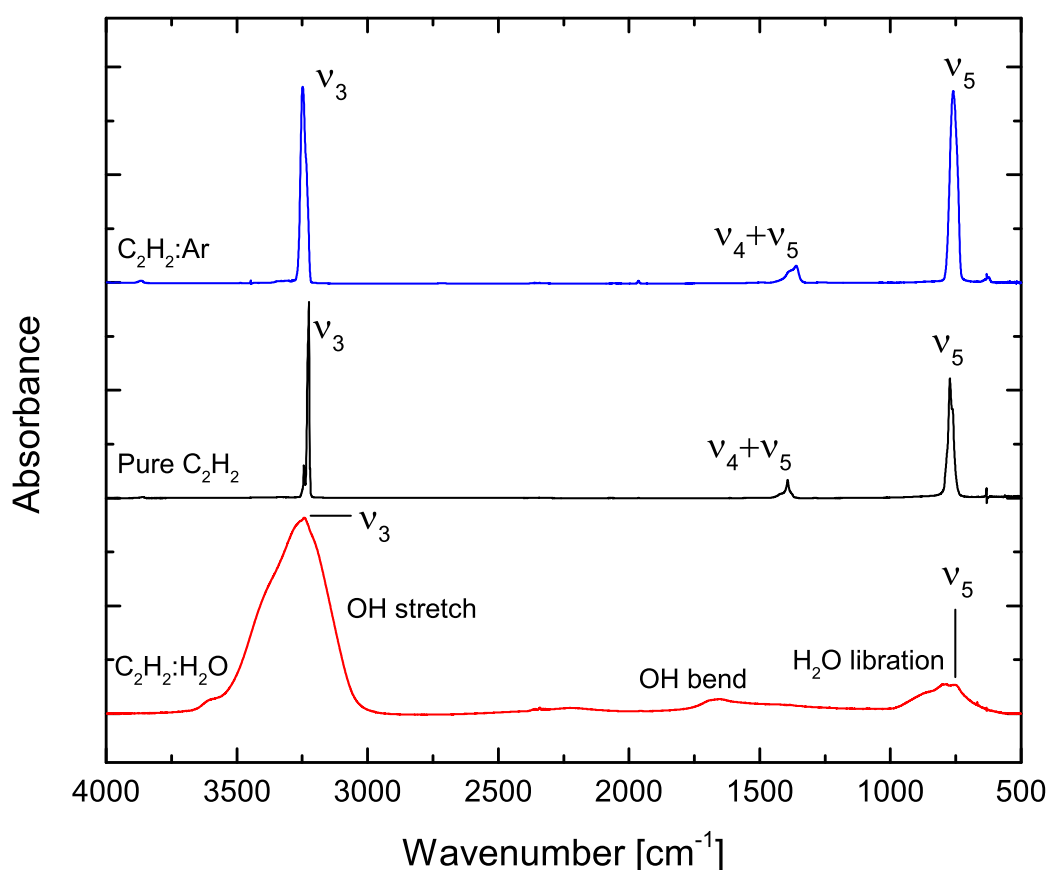


Figure 7.1 — IR spectra from 4000 cm^{-1} to 500 cm^{-1} of Ar: C_2H_2 100:1 (top), pure C_2H_2 (middle) and H_2O : C_2H_2 10:1 (bottom) at 12K. In the bottom panel, a zoom of the OH and CH stretching region is added to reveal the weak CH stretching mode of C_2H_2 .

7.3.1 Ar:C₂H₂ results

Isolating C₂H₂ in an argon matrix is a first step towards understanding the C₂H₂ photochemistry. It restricts chemical interactions to the primary interactions only, because in most cases, there is no other molecule or radical in range that effectively results in the stabilization of the radicals formed inside the matrix. In our case, $\sim 90\%$ of the C₂H₂ molecules are isolated in the matrix, while the rest exist as small clusters (Behringer 1958).

The FTIR spectra of irradiated C₂H₂ in an Ar matrix (Fig. 7.2) reveal only a limited destruction fraction ($\sim 5\%$) of C₂H₂ after a fluence of 1.1×10^{18} photons cm⁻². As mentioned above, a baseline resulting from the background deposition of H₂O appears with time. No obvious IR features attributed to the photodissociation products of C₂H₂ (e.g. CH, C₂H) are found in our spectra, except for two very weak features observed at 3452 cm⁻¹ and 3428 cm⁻¹, which may be due to OH radicals (Acquista et al. 1968) and consistent with observations of OH in the UV-vis spectra that are discussed below.

The corresponding measurements in the UV-vis domain reveal the gradual appearance of four bands upon VUV irradiation (Fig. 7.3). The signal-to-noise level is limited, mainly because of optical interference. A feature at 310.6 nm is accompanied by a second feature at 285.7 nm and a very weak feature at 258.1 nm gradually appearing over time. The first two features are potentially due to C₂H (Graham et al. 1974) or OH (Pellerin et al. 1996) as a photoproduct of background deposited water. The experiment is therefore repeated without deposition of any matrix (and therefore only background deposition). This experiment features both stronger peaks and a hint of the third peak leading to the conclusion that these three peaks are a result of the A²Σ⁺(ν = 0, 1, 2) ← X²Π(ν = 0) transitions of OH. The last peak observed at 237.6 nm does not appear in the blank measurement, showing its origin as a photoproduct of C₂H₂. Based on Milligan et al. (1967), it can be attributed to the (0,0) band of the Mulliken system of C₂ (D¹Σ_u⁺ - X¹Σ_g⁺).

Similar experiments have been performed before by Chang & Graham (1982); Graham et al. (1974), and Milligan et al. (1967). Specifically, the observations of Chang & Graham (1982) provide an intimate view on the photochemistry of C₂H₂ embedded in an argon matrix. Using UV spectroscopy in the range of 130 - 300 nm, C₂, C₂H and C₄H₂ were observed as the main reaction products. Although no photon fluence was given, we note that, the 237.6 nm peak is found to be saturated in their experiment, which is only about 1 % absorption in ours. This indicates that the photon fluence in Chang & Graham (1982) must have been substantially higher. The lower radiation fluence in our experiment is consistent with the non-detection of C₂H and C₄H₂.

7.3.2 Pure C₂H₂ results

Figs. 7.4, 7.5 and 7.6 show the FTIR and UV-vis spectra of irradiated pure C₂H₂ ice. From the partial disappearance of the three strongest IR peaks, it is concluded that the photoirradiation of C₂H₂ with a fluence of 1.1×10^{18} photons cm⁻² leads to destruction of about 50% of the initially deposited C₂H₂. In all spectra, a wealth of new features appears.

Table 7.1 — IR assignments of C₂H₂ and H₂O features in the deposition spectra.

Assignment	Literature value cm ⁻¹	Pure C ₂ H ₂ cm ⁻¹	C ₂ H ₂ :Ar cm ⁻¹	C ₂ H ₂ :H ₂ O cm ⁻¹
C ₂ H ₂ CH stretch ν_3	3239 ^a	3224	3249	3241
C ₂ H ₂ combination mode $\nu_4+\nu_5$	1371 ^a	1393	1361	1388
C ₂ H ₂ CH bending ν_5	743 ^a	773	761	757
H ₂ O OH stretch	3280 ^b	-	-	3253
H ₂ O OH bending	1660 ^b	-	-	1655
H ₂ O OH libration	760 ^b	-	-	801

Notes. ^(a)Knez et al. (2012), ^(b)Gerakines et al. (1995)

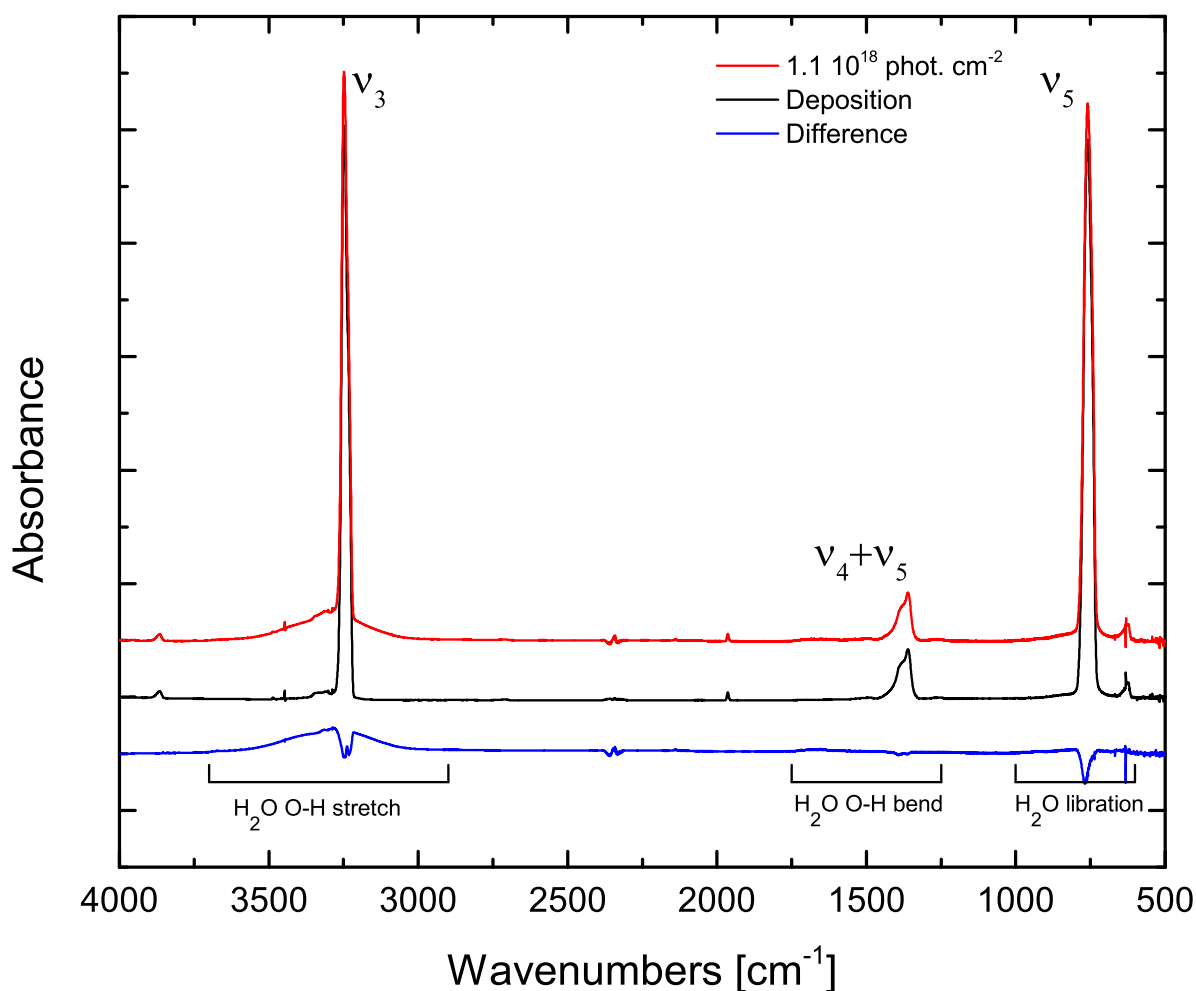


Figure 7.2 — IR spectra from 4000 cm⁻¹ to 500 cm⁻¹ of Ar:C₂H₂ 100:1 under VUV irradiation. The top spectra are the spectra after irradiation with 1.1×10^{18} photons, the middle spectrum is the deposition spectrum while the bottom spectrum is the difference between both. Note the background deposited water and the limited destruction of C₂H₂.

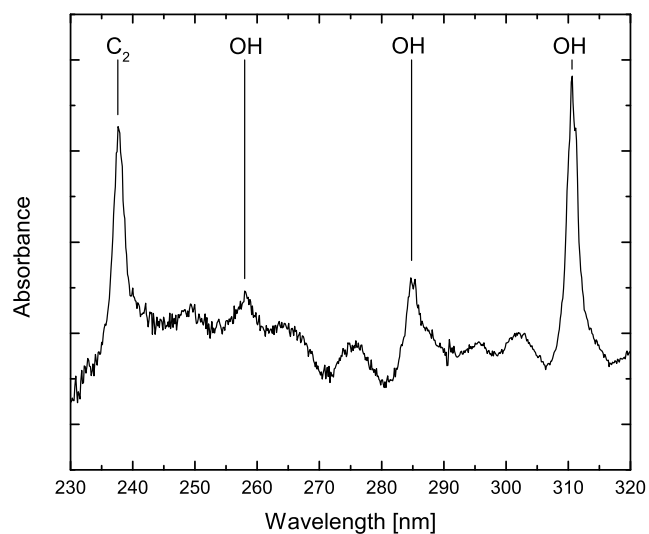


Figure 7.3 — UV-vis spectra of Ar:C₂H₂ 100:1 under VUV irradiation.

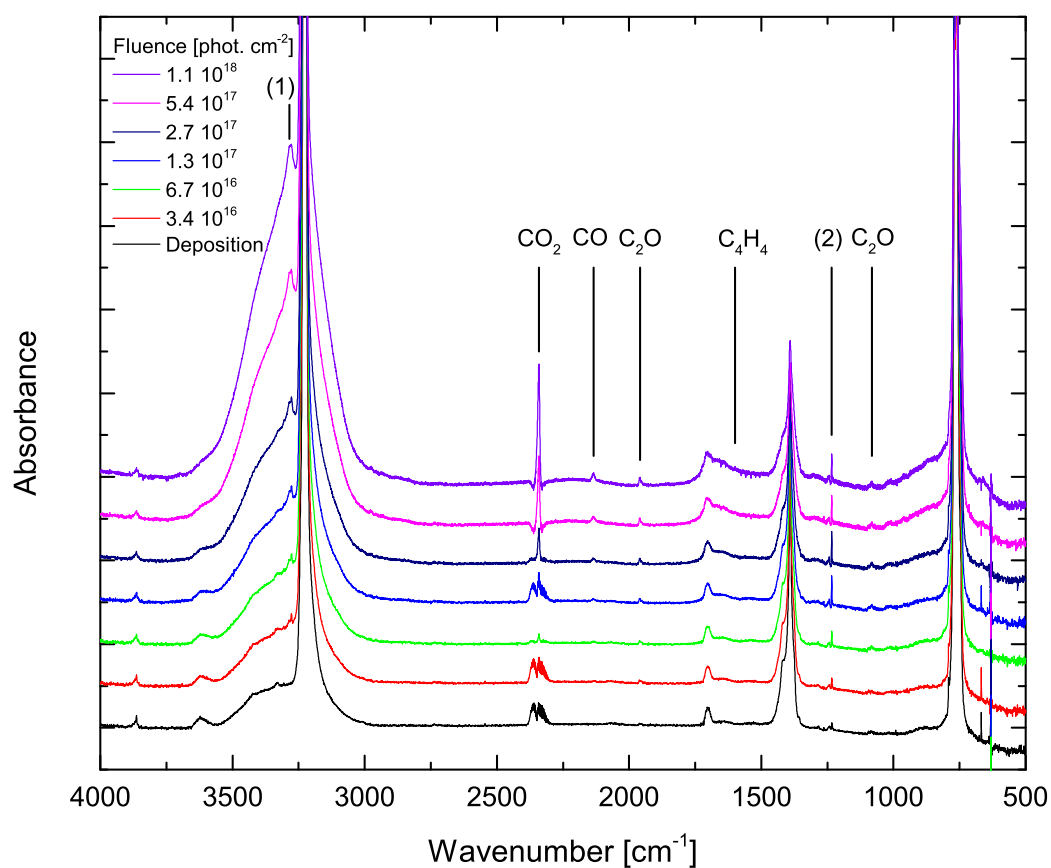


Figure 7.4 — IR spectra from 4000 cm⁻¹ to 500 cm⁻¹ of pure C₂H₂ under VUV irradiation. The strongest photoproduct features are indicated while the features marked (1) and (2) are zoomed in in Fig. 7.5.

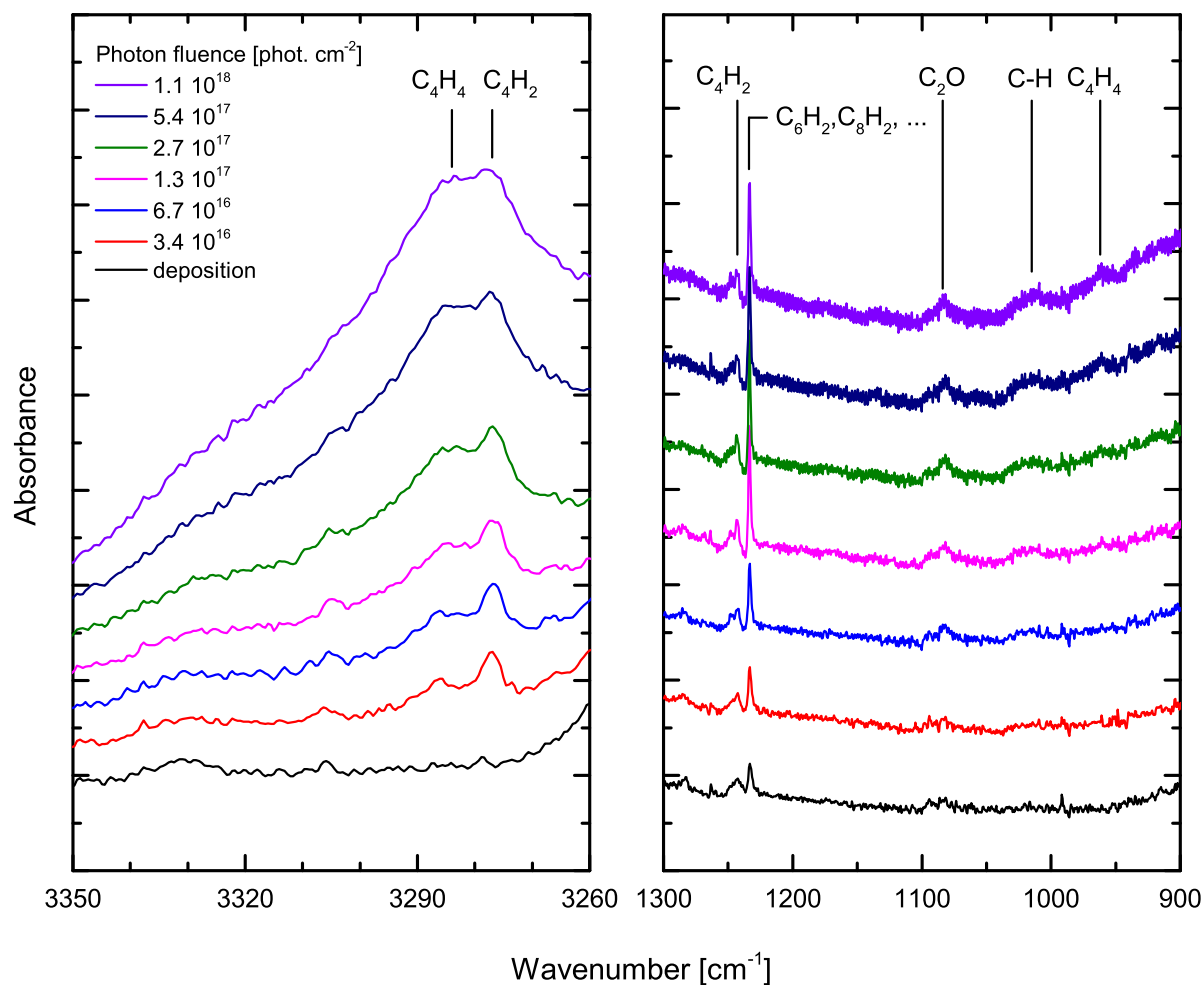


Figure 7.5 — Selected details of the IR spectra of pure C_2H_2 under VUV irradiation.

7.3.2.1 Polymerization

Upon VUV irradiation of pure C_2H_2 ice, the production of short polyynes can be identified in the FTIR spectra. Two IR features at ~ 3277 and 1243 cm^{-1} (Fig. 7.4, marked as (1) and (2)) and tentatively a third one at 1010 cm^{-1} , partially overlapping with other bands are visible. A zoom of these features in Fig. 7.5 reveals their structure in more detail. These features are assigned to C_4H_2 (Khelifi et al. 1995).

Further polymerization can be observed from the feature at 1234 cm^{-1} (Fig. 7.5), which can be identified as C_6H_2 , C_8H_2 or longer (Shindo et al. 2001, 2003). The aforementioned reaction products have known vibrational transitions both in the short wavelength range of the C-H stretching mode and around the C-H bending mode. Shindo et al. (2001, 2003) and Zhou et al. (2009) have observed other stronger features at 600 , ~ 620 , 664 , ~ 3330 , and 3386 cm^{-1} . Owing to a combination of the water baseline and worsened signal-to-noise ratios in these parts of the spectrum, these features are not unambiguously identified in our spectra. Table 7.2 provides a summary of the IR features, assignments and their literature values.

Table 7.2 — IR assignments of VUV photoproducts and comparison with the literature values over all three matrix types. Locations indicated with '-' did not reveal any of the photoproducts.

Feature	Literature cm ⁻¹	Pure C ₂ H ₂ cm ⁻¹	C ₂ H ₂ :Ar cm ⁻¹	C ₂ H ₂ :H ₂ O cm ⁻²
-	-	-	-	-
OH ^a	3452	-	3452	-
C ₄ H ₄ ^b	3284	3284	-	-
C ₄ H ₂ ^c	3277	3277	-	-
OH ^a	3248	-	3248	-
CO ₂ ^d	2347	2341	-	2347
CO ^d	2141	2134	-	2141
C ₂ O ^e	1962	1959	-	-
H ₂ CO ^f	1727 + wing	-	-	1711 - 1680
C ₄ H ₄ ^a	1599	1599	-	-
H ₂ CO ^f	1498	-	-	1496
CH ₃ OH ^g	1452	-	-	1435
CH ₄ ^f	1301	-	-	1303
C ₄ H ₂ ^h	1248 - 1243	1243	-	-
C ₆ H ₂ , C ₈ H ₂ , ... ⁱ	1237 - 1229, 1232 - 1226	1234	-	1233
C ₂ O ^e	1081	1081	-	-
CH ₃ OH ^g	1032	-	-	1019
C ₄ H ₂ ^c	1010	1020 (t.)	-	-
C ₄ H ₄ ^b	962	979	-	-

^(a)Acquista et al. (1968), ^(b)Kim & Kaiser (2009), ^(c)Zhou et al. (2009), ^(d)Gerakines et al. (1995), ^(e)Jacox et al. (1965), ^(f)Öberg et al. (2009), ^(g)Falck & Whalley (1961), ^(h)Khelifi et al. (1995), ⁽ⁱ⁾Shindo et al. (2001, 2003)

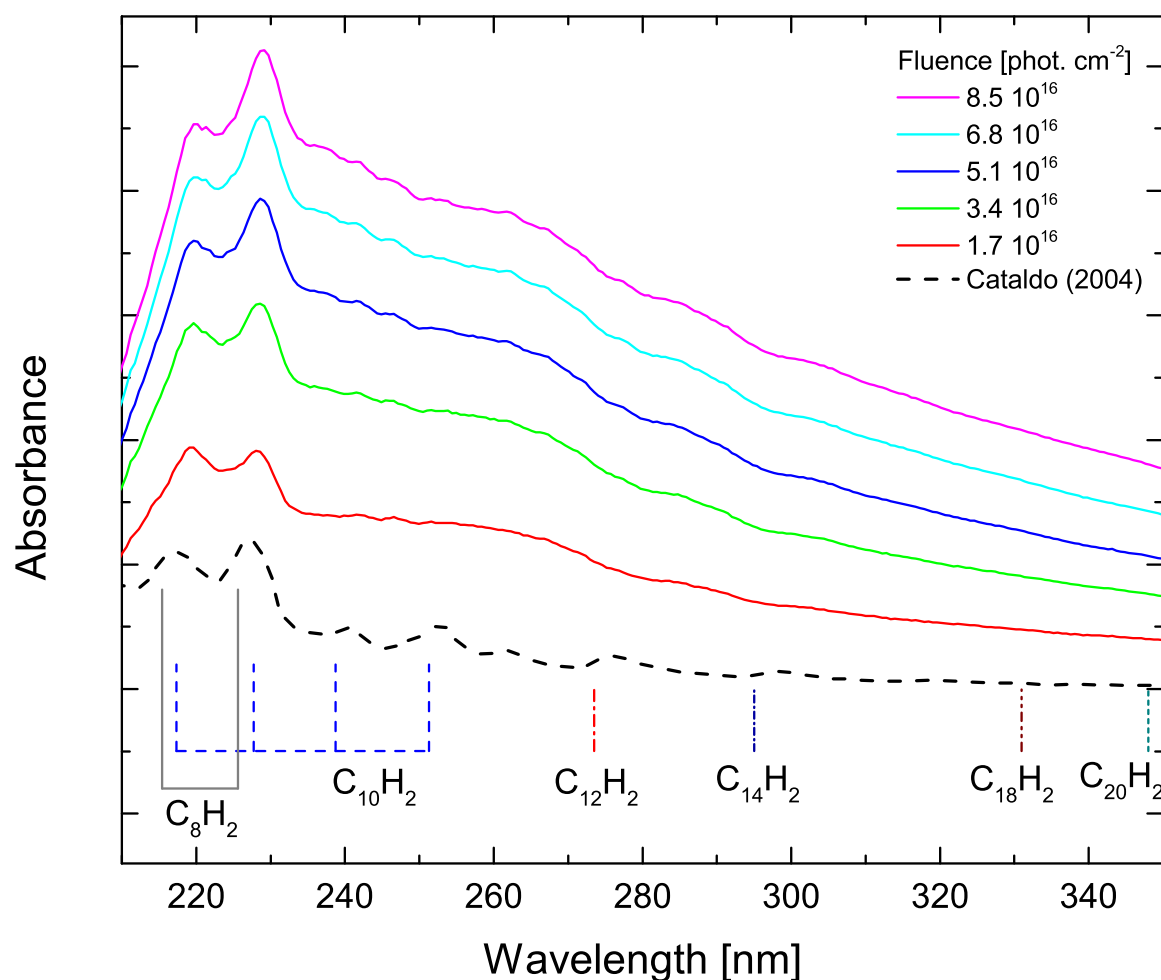


Figure 7.6 — UV-vis spectra of pure C_2H_2 under VUV irradiation, polyne feature values are solution values obtained from Kloster-Jensen et al. (1974). The bottom trace shows the remarkable similar spectra obtained by Cataldo (2004).

A typical aspect of polyynes of C_6H_2 and longer ones is that the IR transitions remain at nearly the same location. This hampers their individual identification (Jolly & Bénilan 2008). Here, the combination of FTIR spectroscopy with UV-vis spectroscopy provides complementary information for identifying photoproducts, since the absorption features in the UV-vis provide better uniqueness, allowing for easier identification (Kloster-Jensen et al. 1974; Grutter et al. 1998).

The UV-vis spectra of the irradiated C_2H_2 ice are dominated by two very strong bands at 219 nm and at 228 nm and a very broad wing with weak, unresolved features up to 400 nm (Fig. 7.6). A third peak at 209.5 nm appears in repeated experiments that are not shown here. The origin of these peaks is not *a priori* clear, although similar studies can provide very useful insight into their identification. VUV irradiation of C_2H_2 embedded in noble gas matrix by Wu & Cheng (2008) yielded polyynes $(H-(C\equiv C)_mH)$ up to C_8H_2 and linear carbon chains (C_m) up to C_8 . From this, one would expect that when a pure C_2H_2 ice is irradiated, polymerization will result in the formation of similar molecules (e.g. $H-(C\equiv C)_mH$, $H-(C\equiv C)_m$ or $(C\equiv C)_m$).

Comparing our UV-vis spectra to spectra obtained by arcing of graphitic electrodes submerged in water (Cataldo 2004), also shown in Fig. 7.6, a remarkable similarity appears. The spectra from Cataldo (2004) are also dominated by two strong peaks associated with a broad, partially resolved wing up to 400 nm. High-performance liquid-chromatography (HPLC) analysis revealed the spectra obtained by Cataldo (2004) to be due to polyynes in the $C_6H_2 - C_{16}H_2$ range, although no spectroscopic assignments were made. The UV-vis spectra of polyynes typically feature the ${}^1\Sigma_u^+ \leftarrow {}^1\Sigma_g^+$ as the strongest transition accompanied by multiple vibronic progressions (Kloster-Jensen et al. 1974) towards the short wavelength side. On the long wavelength side of this system, two overlapping forbidden electronic transitions (${}^1\Sigma_u^- \leftarrow {}^1\Sigma_g^+$ and ${}^1\Delta_u \leftarrow {}^1\Sigma_g^+$) and their vibronic progressions appear albeit with oscillator strengths that are three orders of magnitude smaller. When using the band assignments of liquid matrix polyynes as observed by Kloster-Jensen et al. (1974) to interpret our spectra (Fig. 7.6), the strongest signals are likely due to C_8H_2 , with longer polyyne signals, possibly up to $C_{20}H_2$, hidden in the broad wing extending up to 400 nm. This shows consistency in overall profile with our FTIR data where C_8H_2 is also observed.

A multitude of polyyne species are therefore the most probable explanation for the absorption features observed. Moreover, it has been found by Cataldo et al. (2008) that polyynes are the dominant product of the UV photochemistry of C_2H_2 suspended in liquid at room temperature.

In addition, the broad UV absorption feature is further investigated while slowly warming up the ice (Fig. 7.7). During warmup, separate absorption features in the 230 - 280 nm and in the 290 - 320 nm become visible, but there is no sign of existing features disappearing up to the point where the C_2H_2 matrix desorbs around 50K. This shows that there is further enrichment of the ice with polyynes or polyyne-like species and when cross-referencing the new features with known absorption spectra of polyynes, there are indications of the formation of polyynes in the $C_8H_2 - C_{14}H_2$ range. The exact thermal processing mechanism is unclear.

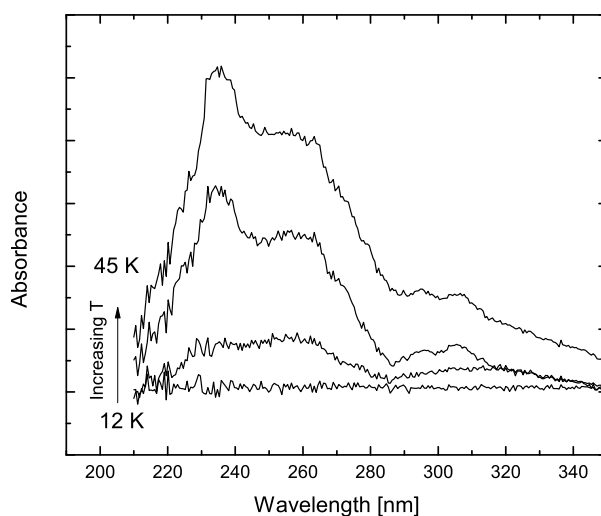


Figure 7.7 — UV-vis spectra of pure C_2H_2 after VUV irradiation, during warmup.

7.3.2.2 Vinylacetylene

During irradiation, features associated to small amounts of vinylacetylene (C_4H_4) appear in the FTIR spectra at 3284 cm^{-1} (Fig. 7.5, left panel), at 1599 cm^{-1} and at 962 cm^{-1} (Fig. 7.5, right panel) (Kim & Kaiser 2009). The remarkable lack of more saturated alkanes in the spectra is different from observations by Strazzulla et al. (2002) after bombardment of C_2H_2 with 15 KeV N^+ ions.

7.3.2.3 Interaction of C_2H_2 with background deposited water

The strongest new features appearing in the FTIR spectra of photoirradiated C_2H_2 (Fig. 7.4) are a result of interaction with the background deposited water. They typically appear in the C=O stretching region ranging from roughly 1800 to 2500 cm^{-1} . The strongest at 2341 cm^{-1} is associated to CO_2 . The 2134 cm^{-1} feature is related to CO. C_2O is identified, based on two features at 1959 cm^{-1} and at 1081 cm^{-1} , and their relative intensities of about 7:1 (Jacox et al. 1965). A summary of the assignments is given in Table 7.2. The appearance of these molecular species shows a complex chemical interaction between C_2H_2 and H_2O besides polymerization.

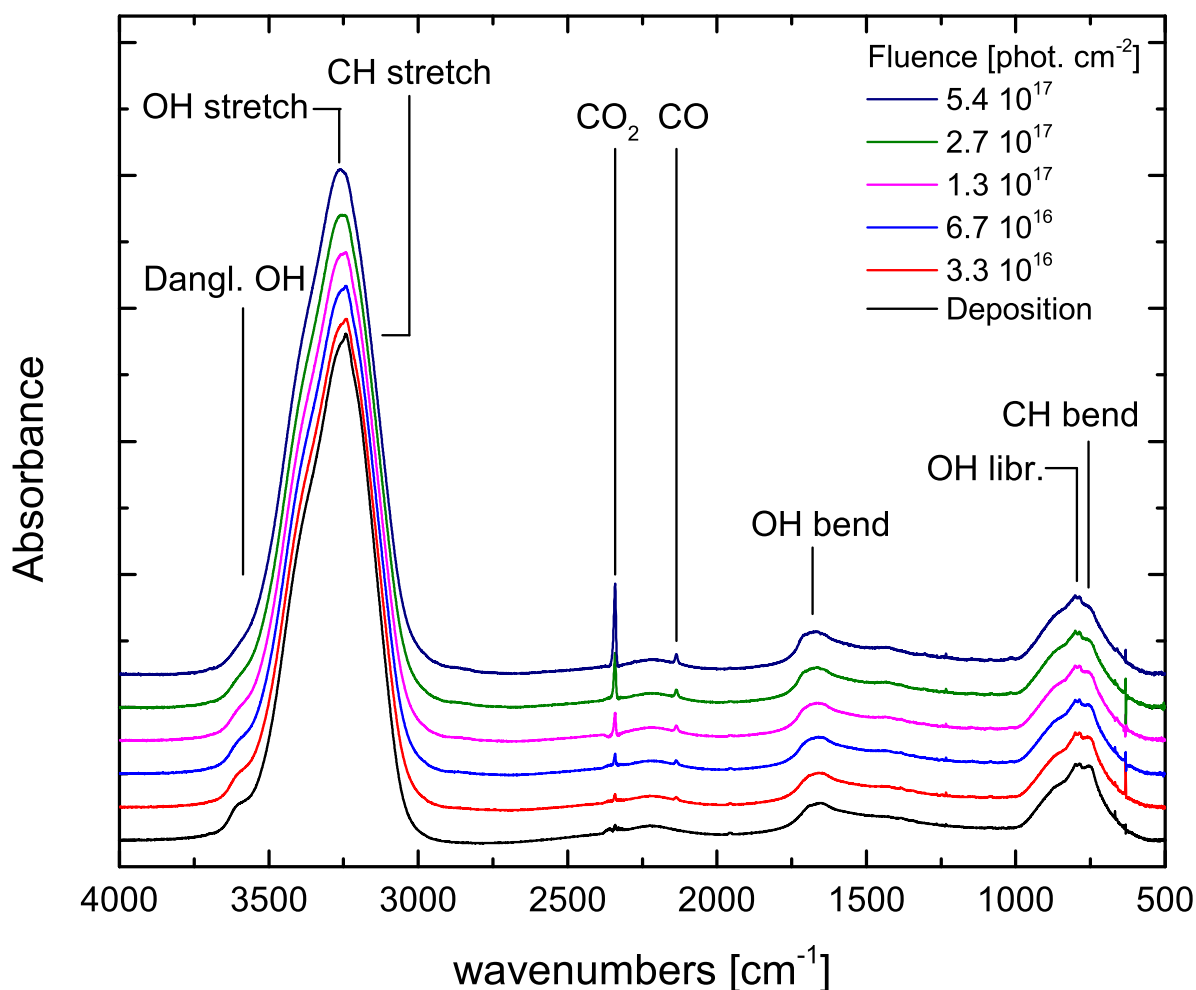


Figure 7.8 — IR spectra from 4000 cm^{-1} to 500 cm^{-1} of $C_2H_2:H_2O$ 1:10 under VUV irradiation.

7.3.3 C₂H₂:H₂O results

The photochemical interaction between C₂H₂ and H₂O can be studied into more detail by embedding C₂H₂ in a H₂O matrix in 1:10 ratio. This system is relevant for the bulk of interstellar solid C₂H₂ which is present in a water-dominated ice environment, although it should be noted that there the abundance is typically lower.

7.3.3.1 Polymerization

When irradiating the ice with VUV photons, some new features gradually appear in the spectra, simultaneously, the C₂H₂ peaks disappear (Fig. 7.8). Most of these features are the result of interaction with the water inside the matrix. The aforementioned feature at 1234 cm⁻¹ can be seen in Fig. 7.9 and is associated to C₆H₂, C₈H₂ and longer polyynes. This feature appears after irradiation with 3.3×10^{16} photons cm⁻¹ and subsequently remains at the same intensity. Its strength is substantially less than in the observations with pure C₂H₂ ice, although its appearance shows that the formation of polyynes persists, even under stiff competition with water-related photoproducts. This observation shows a remarkable consistency with the UV-vis spectra (Fig. 7.10) where the same broad absorption appears as with pure C₂H₂. Two peaks very similar to the ones appearing in irradiated pure C₂H₂ ice (Fig. 7.6) become visible, although significantly widened and slightly red-shifted, which is a typical water-matrix-induced effect. As in the IR, the feature grows to a radiation fluence of 3.4×10^{16} photons cm⁻² and subsequently remains, formally linking both spectral features to the same reaction products. This is consistent with the formation of polyyne-like molecules in the C₈H₂ - C₁₄H₂ range and shows their stability in a water-dominated environment.

7.3.3.2 C₂H₂ photochemical reactions with H₂O

The strongest new features appearing in the FTIR spectra (Fig. 7.8) are at 2347 cm⁻¹ and at 2141 cm⁻¹ and are due to CO₂ and CO, respectively. Besides these strong features, many weaker features appear in the range from 900 to 1800 cm⁻¹ (Fig. 7.9). It should be noted that these spectra are relative to the deposition spectra (with offset); i.e., all features visible in the spectra are likely due to new reaction products.

Most of these can be assigned to reactions between C₂H₂ and water. The feature at 1710 cm⁻¹ and the wing at 1679 cm⁻¹ are typical of formaldehyde (H₂CO) with a second feature at 1498 cm⁻¹ also appearing (Öberg et al. 2009). The features at 1435 and 1019 cm⁻¹ are due to methanol (CH₃OH) (Falck & Whalley 1961), and the feature at 1303 cm⁻¹ is from methane (CH₄) (Öberg et al. 2009). The feature at 1234 cm⁻¹ was discussed above. A similar study by Wu et al. (2002) reports on the photochemistry of a 1:4 C₂H₂:H₂O ice with various wavelengths of vacuum UV radiation that includes Lyman- α . However, assignments were limited to CO and CO₂.

To assess the carbon budget inside the ice, a quantitative analysis of the formation of CO and CO₂ is made based on the IR spectral data. From the integrated area of the OH stretching mode of water in the deposition spectrum, a water column density of $\sim 5.5 \times 10^{17}$ molecules cm⁻² is derived. Knowing the C₂H₂ fraction of 1:10, the amount of carbon is $\sim 1.1 \times 10^{17}$ atoms cm⁻² (2 carbon atoms per C₂H₂ molecule). The amount of CO and CO₂ is interpreted directly from their IR transition intensities and summarized

in Fig. 7.11. After the final radiation fluence of $\sim 5.4 \times 10^{17}$ photons cm^{-2} , about 12 % of the initial carbon budget is stored in CO and CO_2 molecules although all C_2H_2 has disappeared from the spectra. The formation rate of CO_2 is linear with radiation fluence while for CO , although initially dominant, the formation rate decreases with time. This is consistent with a view that, in a water-dominated environment, CO is the precursor for formation of CO_2 , H_2CO and CH_3OH upon VUV irradiation (Watanabe & Kouchi 2002).

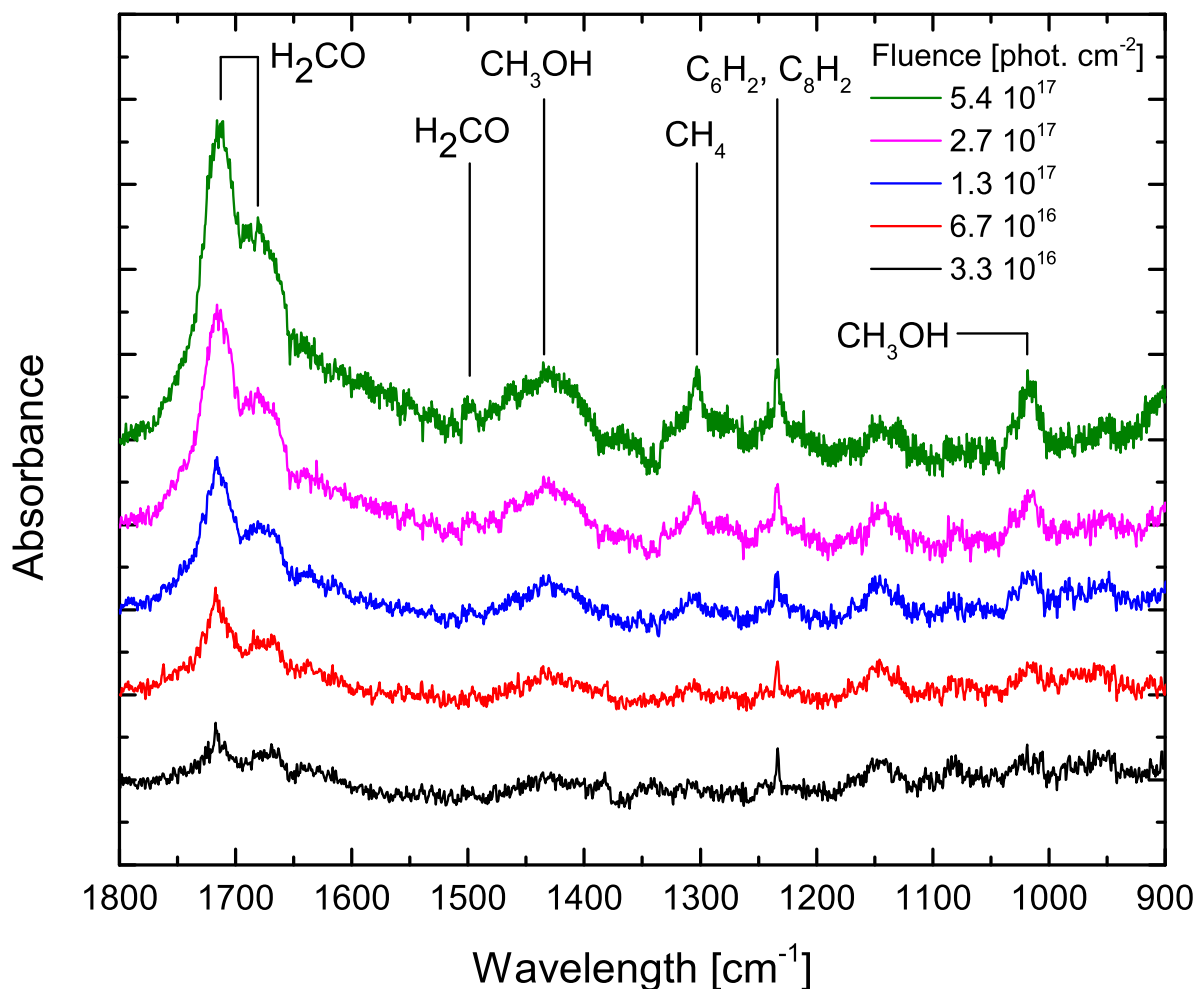


Figure 7.9 — Selected detail of the IR spectra of $\text{C}_2\text{H}_2:\text{H}_2\text{O}$ 1:10 under VUV irradiation. These spectra are difference spectra (with an offset for each spectrum), meaning that all positive peaks appearing are photoproducts.

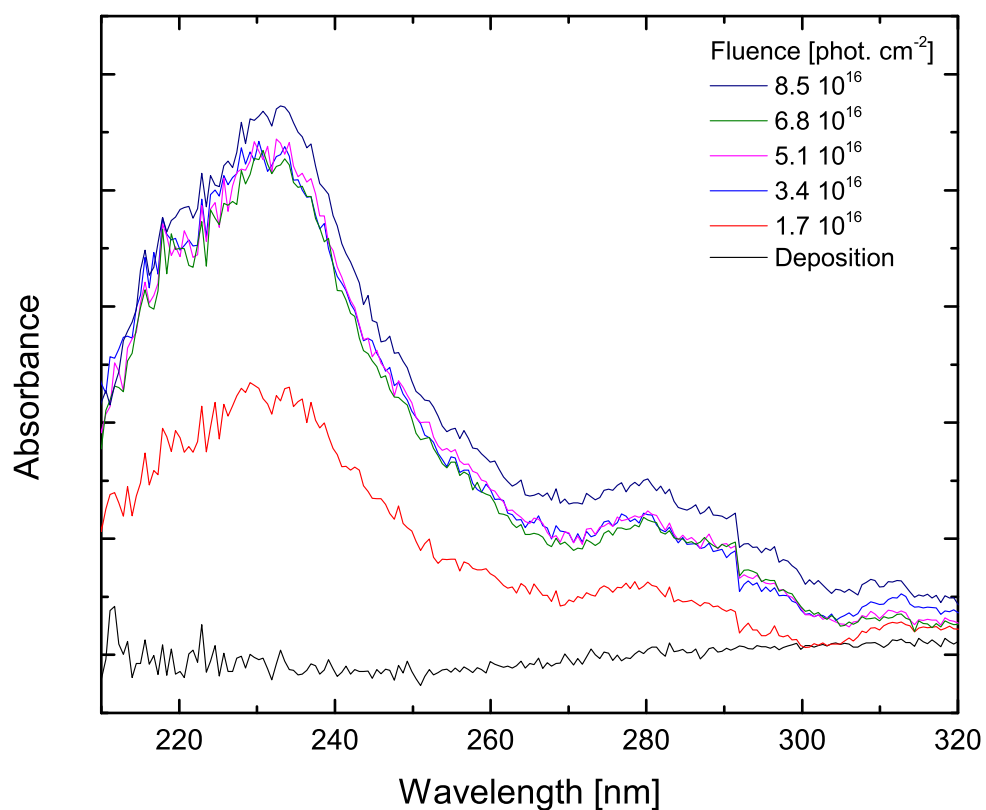


Figure 7.10 — UV-vis spectra of $C_2H_2:H_2O$ 1:10 under VUV irradiation.

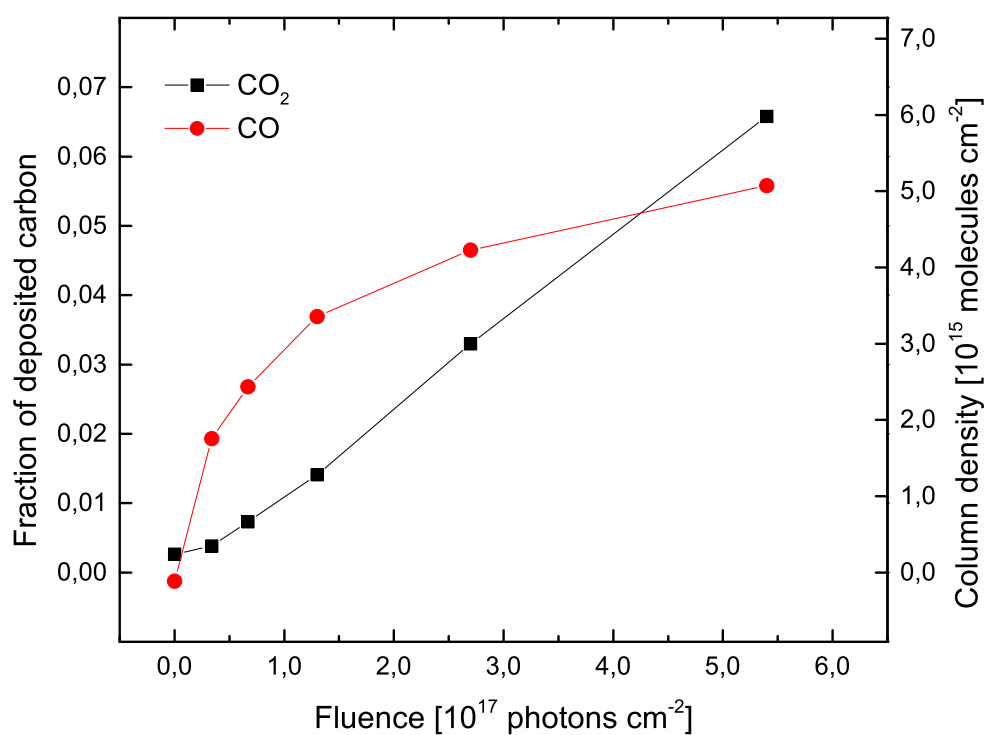


Figure 7.11 — Production of CO and CO_2 upon VUV irradiation of a $C_2H_2:H_2O$ 1:10 ice as a function of total deposited carbon and radiation fluence.

7.3.4 Discussion

The observations with both methods show a very consistent image of the role C_2H_2 plays in ice photochemistry. The photodissociation pathways of C_2H_2 were analyzed by Okabe (1975). The VUV lamp provides enough energy to overcome the threshold of five dissociation pathways:

<i>Reaction</i>	<i>Threshold</i>
$C_2H_2 + h\nu \rightarrow C_2H + H$	230.6nm
$C_2H_2 + h\nu \rightarrow C_2 + H_2$	198.5nm
$C_2H_2 + h\nu \rightarrow C_2(A^3\Pi) + H_2$	142.2nm
$C_2H_2 + h\nu \rightarrow C_2(B)H + H$	130.5nm
$C_2H_2 + h\nu \rightarrow 2 \times CH$	125.3nm

The VUV emission profile comprises Lyman-alpha radiation and a broadband component around 160 nm roughly in a 1:2 intensity ratio (Chapter 3). As dehydrogenation requires less energy than dissociation of the $C\equiv C$ triple bond (for which the broadband at 160 nm does not provide enough energy), dehydrogenation will be the dominant pathway. This is confirmed by our experimental results for detecting C_2 (and not CH) when C_2H_2 is embedded in a noble-gas matrix. This process is also expected to take place when irradiating pure C_2H_2 . Owing to the high reactivity of the C_2 and C_2H radicals, they are readily converted to polyynes, resulting in steady-state column densities that are too low to be observable. The low barrier for polymerization becomes apparent when warming up the ice. During ice warmup, the resulting increase in mobility further enhances the formation of longer polyynes.

When embedding C_2H_2 in a water matrix, the water acts as a source of hydrogen and oxygen in the matrix upon VUV photolysis and their availability has a profound influence on the overall photochemistry observed. It opens a competitive reaction channel to the polymerization observed in water-poor ice. Nevertheless, polymerization can still be observed, although it is less efficient. This is remarkable, given the high abundance of water in the ice. To explain this, the absorption cross section of H_2O and C_2H_2 at 122 and at 160 nm are compared (Mason et al. 2006; Wu et al. 2001). At both wavelengths, the absorption cross section of C_2H_2 is about one order of magnitude larger than the absorption cross section of water. As a consequence, for these settings the dissociation efficiency of C_2H_2 will be higher than for H_2O , explaining the preference for C_2H_2 polymerization over reaction with water-related photoproducts. However, the polymerization is still limited by the availability of C_2H_2 or related radicals present inside the matrix and with increasing fluence, water-related photochemistry takes over. The observation of CO and CO_2 is evidence of the destruction of the $C\equiv C$ triple bond although the reaction pathway is not *a priori* clear. The difference in photoproducts between a water-poor environment and a water-rich environment may hint at possible pathways. In a water-poor environment, the C_2O radical is observed, and is probably the result of a direct oxidation of C_2 . This radical has a significant lifetime inside the matrix, allowing spectroscopic detection, since the abundance of oxygen and other potential reactants is low. It can be expected that a similar process takes place in an

oxygen-rich environment, but owing to the high abundance of oxygen, the C_2O is oxidized further, resulting in the formation of two CO molecules and preventing the detection of C_2O .

When irradiating pure C_2H_2 , small quantities of vinylacetylene (C_4H_4) are observed. The exact reaction pathway for the formation of vinylacetylene is not clear because no intermediates (e.g. vinyl, $-CH=CH_2$, or ethene, C_2H_4) are observed in the spectra. It may well be possible that (excited) C_2H_2 molecules recombine. Vinylacetylene is considered an important precursor molecule in the formation of PAHs (Parker et al. 2012). The strong transitions of benzene at 3095 or 1480 cm^{-1} (Marzocchi et al. 1970) are totally lacking from our spectra, proving that it is absent, and by extension, that no features showing aromatic molecules are observed. This conclusion differs from the observations of Zhou et al. (2010) on the bombardment of C_2H_2 ice with 5 keV electrons - with a similar total energy dose as applied here - where benzene was observed. It also differs from the observations of Strazzulla et al. (2002), where C_2H_2 ice was bombarded with 15 keV N^+ ions with a comparable total energy dose, and higher alkanes could be found. This is in accordance with Muñoz-Caro et al. (2014, and references therein) and illustrates the dependence of solid state chemistry on the type of energy injected into the chemical system.

7.4 Astrophysical implications

Polyynes-like molecules (e.g. polyynes, C_nH) and cyanopolyynes (HC_nN) have been observed, or were said to be present on the basis of theoretical calculations, in a variety of astrophysical environments, such as active galactic nuclei (e.g. Harada et al. 2013), carbon-rich protostellar objects (e.g. Cordiner et al. 2012; Cordiner & Charnley 2014; Gupta et al. 2009; Sakai et al. 2009), interstellar clouds (Duley & Hu 2009; Cernicharo et al. 1984; Herbst & Leung 1989), and objects in the solar system, such as comets (Cordiner & Charnley 2014) and Uranus (Burgdorf et al. 2006). A special mention goes to the atmosphere of Titan where the photolysis of a methane plus hydrogen mixture induces a plethora of chemical reactions that lead to the formation of polyynes (Smith et al. 1998), which are also involved in the formation of the UV haze (Hunten 2006). Diacetylene (C_4H_2), the smallest of the polyynes, has been detected by instruments on board the Huygens probe and simulations predicted the presence of gaseous C_6H_2 and C_8H_2 (Hunten 2006).

The work presented here investigates the formation route of polyynes in grain mantles, namely UV photoprocessing of acetylene-containing ices. The results of this paper along with those obtained after ion bombardment experiments of frozen C_2H_2 (Compagnini et al. 2009) give confidence that energetic processing of ices in astrophysical environments can contribute to the budget of polyynes in the universe. It is also clear that this is only a first qualitative step towards gaining insight into this field.

Subsequent thermal processing of these ices yields formation of longer chains and potentially new carbonaceous species. Further heating expels these molecules to the gas phase as the matrix desorbs. In this way, enrichment of the gas phase with new molecules takes place. The observation of vinylacetylene in the ice potentially yields a formation pathway towards PAHs to which it is known to be a precursor. This is

an interesting finding, because PAHs are ubiquitous in space, and they are generally assumed to form in the outflows of AGB stars, in accordance with the experiments of Geenberg et al. (2000) that analyze gas chromatographically residues obtained after UV photolysis of ice and ice residu. The present results hint at a (complementary) bottom-up formation mechanism.

It is very well known that the photoprocessing of ice mantles in the cold clouds of the interstellar medium plays a dominant role in determining the molecular complexity of the ices. In our experiments we have used photon fluences up to 10^{18} photons cm^{-2} corresponding to exposure times of several 10^7 years, i.e., comparable to time regimes that are covered in dark interstellar clouds. (Cecci-Pestellini & Aiello 1992; Mathis et al. 1983; Prasad & Tarafdar 1983; Mennella et al. 2003). In our experiments we have used photon fluences up to 10^{18} photons cm^{-2} corresponding to an exposure time ranging up to $\sim 2 \times 10^7$ years, perfectly compatible with the lifetime of an interstellar dark cloud. As we observed in our experiments the formation of polyynes under similar conditions, even in a H_2O -dominated ice, it is possible that a certain number of polyynes are formed although it is, at present, impossible to quantify their amount.

These understandings are backed up by recent observations of polyyne-like molecules in Cha-MMS1 (Cordiner et al. 2012). Their abundances are found to be in the range of 10^{-10} with respect to H_2 , are similar to those in the envelope of the older, more luminous class-0/I protostar L1527, and are greater than in another low-luminosity, low-mass class-0 protostellar envelope (Cordiner et al. 2012). This phenomenon has been attributed by the same authors to a combination of factors including the desorption of grain mantle species into the gas phase by e.g. warming by the protostar. It is in fact well known that an important contribution to the gas phase molecules in star forming regions is given by the sublimation of carbon chain and other complex organic molecular species present in icy mantles (Modica & Palumbo 2010; Palumbo et al. 2008b).

Besides this, we provide strong clues to how to detect them inside the ice, both in the IR and in the UV-vis range. In the case of a VUV-irradiated C_2H_2 ice, three peaks at 209.5, 219 and 228 nm are expected to appear in the UV absorption spectra, while in a water-dominated environment, these peaks shift about 3 nm to longer wavelength. They are very distinct from the UV bump at 217.5 nm. Many of the features in the IR spectra of polyyne photoproducts feature a strong overlap with other ice components, mainly water. Therefore, the most distinct features to search for appear at 1234 and 1243 cm^{-1} .

7.5 Conclusions

In this paper, we have reported a systematic laboratory study of the VUV photochemical behaviour of C_2H_2 in interstellar ices. It comprises a combined approach of two *in situ* techniques: FTIR spectroscopy and UV-vis spectroscopy. The main conclusions from the experiments are:

1. The dominating reaction pathway of C_2H_2 in the solid state is polymerization resulting in formation of polyyne-like molecules upon VUV irradiation. From the spectra, polyynes in the C_4H_2 - C_8H_2 are observed while the formation of polyynes up to at least C_{20}H_2 are suggested. The low reaction barrier for poly-

merization is indicated by the observation of polymerization upon the warming up of an irradiated ice. Under competition with water-related photoproducts, polymerization persists and polyynes are observed in a water-dominated C_2H_2 ice. This solid state process may contribute to the observed enhanced abundances of polyynes in the gas phase.

2. The spectra provided here offer a tool to search for solid state polyynes in astronomical spectra. In the IR, absorption features at 1234 cm^{-1} and at 1243 cm^{-1} are expected to appear in absorption spectra free of interaction with water-related bands. In the UV-vis, the spectra of ices containing polyynes are expected to be dominated by absorption C_8H_2 features at 227.0 and 218.0 nm.
3. The detection of vinylacetylene in the photoirradiated ice offers a first step in the pathway towards the formation of PAHs as this molecule is considered to be one of the main precursor molecules. Aromatic features are, however, not observed in our laboratory spectra.

Acknowledgments

This research is financially supported by the Netherlands School for Astronomy, NWO-VICI, the Dutch Organisation for Science, and the European Community's 7th Framework Programme (FP7/2007-2013) under grant agreement n.238258. SHC wants to acknowledge the interesting and stimulating discussions with Dr. G. Rouillé and Dr. C. Jäger from Friedrich Schiller university, Jena. GS is grateful to NWO for the support during his visiting period in Leiden (Apr 30 - July 28, 2012).

Bibliography

- Acquista, N., Schoen, L. J., & Lide, D. R. J. 1968, *J. Chem. Phys.*, 48, 1534
- Al-Zaal, M., Miller, H. C., & Farley, J. W. 1987, *Phys. Rev. A*, 35, 1099
- Allamandola, L. J., Tielens, A. G. G. M., & Barker, J. R. 1989, *ApJ*, 71, 733
- Apostolopoulou, V., Vakros, J., Kordulis, C., & Lycourghiotis, A. 2009, *Coll. Surf. A Phys. Chem. Eng. Aspects*, 349, 189
- Atreya, S. K., Wong, A. S., Baines, K. H., Wong, M. H., & Owen, T. C. 2005, *Planet. Space Sci.*, 53, 498
- Baines, K. H., Carlson, R. W., & Kamp, L. W. 2002, *Icarus*, 159, 74
- Baratta, G. A., Leto, G., & Palumbo, M. E. 2002, *A&A*, 384, 343
- Barnard, E. E. 1910, *ApJ*, 31, 8
- Barnard, E. E. 1927, *Catalogue of 349 dark objects in the sky* (Chicago: University of Chicago press)
- Bauschlicher, C. W., Peeters, E., & Allamandola, L. J. 2008, *ApJ*, 678, 316
- Bauschlicher, C. W., Peeters, E., & Allamandola, L. J. 2009, *ApJ*, 697, 311
- Behringer, R. E. 1958, *J. Chem. Phys.*, 29, 537
- Bénilan, Y., Gazeau, M.-C., Es-Sebbar, E.-T., et al. 2011, *EPSC-DPS Joint Meeting*, 1317, 1
- Bennett, C. J., Jones, B., Knox, E., et al. 2010, *ApJ*, 723, 641
- Berné, O. & Tielens, A. G. G. M. 2012, *Proc. Nat. Acad. Sci. USA*, 109, 401
- Bernstein, M. P., Elsila, J. E., Dworkin, J. P., et al. 2002, *ApJ*, 576, 1115
- Bernstein, M. P., Sandford, S. A., & Allamandola, L. J. 2005, *ApJs*, 161, 53
- Bernstein, M. P., Sandford, S. A., Allamandola, L. J., et al. 1999, *Science*, 283, 1135
- Bernstein, M. P., Sandford, S. A., Mattioda, A. L., & Allamandola, L. J. 2007, *ApJ*, 664, 1264
- Biennier, L., Sabbah, H., Chandrasekaran, V., et al. 2011, *A&A*, 532, 40

- Bito, Y., Shida, N., & Toru, T. 2000, *Chem. Phys. Lett.*, 328, 310
- Bizzarro, M. 2014, *Science*, 345, 620
- Boersma, C., Bregman, J. D., & Allamandola, L. J. 2013, *ApJ*, 769, 117
- Boogert, A. C. A., Huard, T. L., Cook, A. M., et al. 2011, *ApJ*, 729, 92
- Boogert, A. C. A., Pontoppidan, K. M., Knez, C., et al. 2008, *ApJ*, 678, 985
- Boogert, A. C. A., Pontoppidan, K. M., Lahuis, F., et al. 2004, *ApJS*, 154, 359
- Bossa, J.-B., Isokoski, K., de Valois, M. S., & Linnartz, H. 2012, *A&A*, 545, 82
- Bossa, J.-B., Isokoski, K., Paardekooper, D. M., et al. 2014, *A&A*, 561, 136
- Bottinelli, S., Boogert, A. C. A., Bouwman, J., et al. 2010, *ApJ*, 718, 1100
- Bouwman, J., Cuppen, H., Steglich, M., Allamandola, L. J., & Linnartz, H. 2011a, *A&A*, 529, 46
- Bouwman, J., Cuppen, H. M., Bakker, A., Allamandola, L. J., & Linnartz, H. 2010, *A&A*, 511, 33
- Bouwman, J., Ludwig, W., Awad, Z., et al. 2007, *A&A*, 476, 995
- Bouwman, J., Mattioda, A. L., Linnartz, H., & Allamandola, L. J. 2011b, *A&A*, 525, 93
- Bouwman, J., Paardekooper, D. M., Cuppen, H. M., Linnartz, H., & Allamandola, L. J. 2009, *ApJ*, 700, 56
- Brooke, T. Y., Knacke, R. F., Encrenaz, T., et al. 1998, *Icarus*, 136, 1
- Burgdorf, M., Orton, G., van Cleve, J., Meadows, V., & Houck, J. 2006, *Icarus*, 184, 634
- Cami, J., Bernard-Salas, J., Peeters, E., & Malek, S. E. 2010, *Science*, 329, 1180
- Carr, J. S. & Najita, J. R. 2008, *Science*, 319, 1504
- Catalán, J. 1994, *Chem. Phys. Lett.*, 223, 159
- Catalán, J. & Pérez, P. 2000, *Fullerenes, Nanotubes, Carbon nanostruct.*, 10, 171
- Cataldo, F. 2004, *Tetrahedron*, 60, 4265
- Cataldo, F., Strazzulla, G., & Iglesias-Groth, S. 2008, *Int. J. Astrobiol.*, 7, 107
- Cecchi-Pestellini, C. & Aiello, S. 1992, *Mon. Not. R. Astron. Soc.*, 258, 125
- Cernicharo, J. 2004, *ApJ*, 608, 41
- Cernicharo, J., Guelin, M., & Askne, J. 1984, *A&A*, 138, 371

- Cernicharo, J., Heras, A. M., Pardo, J. R., et al. 2001, *ApJ*, 546, 127
- Chang, K. W. & Graham, W. R. M. 1982, *J. Mol. Sp.*, 94, 69
- Chen, Y.-J., Chuang, K.-J., Muñoz-Caro, G. M., et al. 2014, *ApJ*, 781, 15
- Chipman, D. M. 2011, *J. Phys. Chem.*, 115, 1161
- Ciesla, F. J. & Sandford, S. A. 2012, *Science*, 336, 452
- Collings, M. P., Dever, J. W., McCoustra, M. R. S., & Fraser, H. J. 2005, *Highlights of astronomy*, 13, 491
- Compagnini, G., D'Urso, L., Puglisi, O., Baratta, G. A., & Strazzulla, G. 2009, *Carbon*, 47, 1605
- Cordiner, M. A. & Charnley, S. B. 2014, *Meteorit. Planet. Sci.*, 49, 21
- Cordiner, M. A., Charnley, S. B., Wirstm, E. S., & Smith, R. G. 2012, *ApJ*, 744, 131
- Cottin, H., Coll, P., Coscia, D., et al. 2008, *Adv. in sp. res.*, 42, 2019
- Cottin, H., Moore, M. H., & Bénilan, Y. 2003, *ApJ*, 590, 874
- Croswell, K. 1996, *Alchemy of the heavens* (New York: Random house publishers)
- Cuppen, H. M., Ioppolo, S., Romanzin, C., & Linnartz, H. 2010, *Phys. Chem. Chem. Phys.*, 12, 12077
- Dai, S., Toth, L. M., Delcul, G. D., & Metcalf, D. H. 1994, *J. Chem. Phys.*, 101, 4470
- Demyk, K., Dartois, E., D'Hendecourt, L., et al. 1998, *A&A*, 339, 553
- Draine, B. T. & Li, A. 2007, *ApJ*, 657, 810
- Draper, H. 1879, *Degli Spettroscopisti Italiani*, 8, 81
- Duley, W. W. & Hu, A. 2009, *ApJ*, 698, 808
- Eastman, D. E. 1970, *Phys. Rev. B*, 2, 1
- Ehrenfreund, P. 2002, *Highlights of astronomy*, 12, 229
- Ehrenfreund, P., D'Hendecourt, L., Verstraete, L., et al. 1992, *A&A*, 259, 257
- Ehrenfreund, P. & Foing, B. H. 2010, *Science*, 329, 1159
- Elsila, J. E., Glavin, D. P., & Dworkin, J. P. 2009, *Meteorit. Planet. Sci.*, 9, 1323
- Emsley, J. 1998, *The element* (Oxford: Clarendon press)
- Evans, A., van Loon, J. T., Woodward, C. E., et al. 2012, *Mon. Not. R. Astron. Soc.*, 421, 92

- Evans, N. J. 1999, *Annu. Rev. Astron.*, 37, 311
- Falck, M. & Whalley, E. 1961, *J. Chem. Phys.*, 34, 1554
- Fayolle, E., Bertin, M., Romanzin, C., et al. 2011, *ApJL*, 735, 36
- Fehsenfeld, F., Evenson, K., & Broida, H. P. 1965, *Rev. Sci. Instrum.*, 36, 294
- Feuerbacher, B. & Fitton, J. 1972, *J. Appl. Phys.*, 43, 1563
- Fuchs, G. W., Cuppen, H. M., Ioppolo, S., et al. 2009, *A&A*, 505, 629
- Fulvio, D., Raut, U., & Bargiola, R. A. 2012, *ApJL*, 752, 33
- Fulvio, D., Sivaraman, B., Baratta, G. A., Palumbo, M. E., & Mason, N. J. 2009, *Spectrochim. Acta*, 72, 1007
- García-Hernández, D. A., Kameswara Rao, N., & Lambert, D. L. 2011, *ApJ*, 729, 126
- Geenberg, J. M., Gillette, J. S., Muñoz Caro, G. M., et al. 2000, *ApJ*, 531, 71
- Geers, V. C., van Dishoeck, E. F., Pontoppidan, K. M., et al. 2009, *A&A*, 495, 837
- Gerakines, P. A., Moore, M. H., & Hudson, R. L. 2000, *A&A*, 357, 793
- Gerakines, P. A., Schutte, W. A., & Ehrenfreund, P. 1996, *A&A*, 312, 289
- Gerakines, P. A., Schutte, W. A., Greenberg, J. M., & van Dishoeck, E. F. 1995, *A&A*, 296, 810
- Gillett, F. C., Forrest, W. J., & Merrill, K. M. 1973, *ApJ*, 183, 87
- Gillis, H. A. & Quickenden, T. I. 2001, *Canadian J. Chem*, 79, 80
- Graham, W. R. M., Dismuke, K. I., & Weltner, W. 1974, *J. Chem. Phys.*, 60, 3817
- Grutter, M., Wyss, M., Fulara, J., & Maier, J. P. 1998, *J. Phys. Chem. A*, 102, 9785
- Gudipati, M. S. & Allamandola, L. J. 2003, *ApJ*, 596, 195
- Gudipati, M. S. & Allamandola, L. J. 2004, *ApJ*, 615, 177
- Gudipati, M. S. & Allamandola, L. J. 2006a, *ApJ*, 638, 286
- Gudipati, M. S. & Allamandola, L. J. 2006b, *ApJ*, 110, 9020
- Gudipati, M. S., Jacovi, R., Lignell, A., & Couturier, I. 2011, *EPSC-DPS joint meeting*, 6, 644
- Guennoun, Z., Aupetit, C., & Mascetti, J. 2011, *J. Phys. Chem. A*, 115, 1844
- Gupta, H., Gottlieb, C. A., McCarthy, M. C., & Thaddeus, P. 2009, *ApJ*, 691, 1494

- Halasinski, T. M., Salama, F., & Allamandola, L. J. 2005, *ApJ*, 628, 555
- Harada, N., Thompson, T. A., & Herbst, E. 2013, *ApJ*, 765, 108
- Hare, J. P., Kroto, H. W., & Taylor, R. 1991, *Chem. Phys. Lett.*, 177, 394
- Haufler, R. E., Chai, Y., Chibante, L. P. F., et al. 1991, *J. Chem. Phys.*, 95, 2197
- Hawkins, S., Kumi, G., Malyk, S., Reisler, H., & Wittig, C. 2005, *Chem. Phys. Lett.*, 404, 19
- Henning, T. & Salama, F. 1998, *Science*, 282, 2204
- Herbst, E. & Leung, C. M. 1989, *ApJs*, 69, 271
- Hudgins, D. M. & Allamandola, L. J. 1995, *J. Phys. Chem.*, 99, 3033
- Hudgins, D. M. & Allamandola, L. J. 1997, *J. Phys. Chem.*, 101, 3472
- Hudson, R. L., Moore, M. H., & Gerakines, P. A. 2001, *ApJ*, 550, 1140
- Hunten, D. M. 2006, *Nature*, 443, 669
- Ismail, I. M. K. & Rodgers, S. L. 1992, *Carbon*, 30, 229
- Jacox, M. E., Milligan, D. E., Moll, N. G., & Thompson, W. E. 1965, *J. Chem. Phys.*, 43, 3734
- Jäger, C., Mutschke, H., & Henning, T. 1998, *A&A*, 332, 291
- Jenniskens, P., Baratta, G. A., Kouchi, A., et al. 1993, *A&A*, 128, 212
- Jolly, A. & Bénilan, Y. 2008, *J. Quant. Spec. Rad. Transf.*, 109, 963
- Jones, B. M., Kaiser, R. I., & Strazzulla, G. 2014, *ApJ*, 781, 85
- Keane, J. V., Tielens, A. G. G. M., Boogert, A. C. A., Schutte, W. A., & Whittet, D. C. B. 2001, *A&A*, 376, 254
- Khan, A. 2004, *J. Chem. Phys.*, 121, 280
- Khelifi, M., Paillous, P., Delpech, C., et al. 1995, *J. Mol. Sp.*, 174, 116
- Kim, Y. S. & Kaiser, R. I. 2009, *ApJs*, 181, 543
- Kjaergaard, H. G., Robinson, T. W., & Brooking, K. A. 2000, *J. Phys. Chem. A*, 104, 11297
- Kloster-Jensen, E., Haink, H.-J., & Heinz, C. 1974, *Helv. Chim. Acta*, 57, 1731
- Knez, C., Moore, M. H., Ferrante, R. F., & Hudson, R. L. 2012, *ApJ*, 748, 95
- Kroto, H. W., Allaf, A. W., & Balm, S. P. 1991, *Chem. Rev.*, 91, 1213

- Kroto, H. W., Heath, J. R., O'Brien, S. C., Curl, R. F., & Smalley, R. E. 1985, *Nature*, 318, 6042
- Kumi, G., Malyk, S., Hawkins, S., Reisler, H., & Wittig, C. 2006, *J. Phys. Chem. A*, 110, 2097
- Lacy, J. H., Evans, N. J., Achtermann, J. M., et al. 1989, *ApJ*, 342, 43
- Lahuis, F. & van Dishoeck, E. F. 2000, *A&A*, 355, 699
- Langford, V. S. & Williamson, B. E. 1998, *J. Phys. Chem. A*, 102, 2415
- Lara, L. M., Lellouch, E., Lopez-Moreno, J. J., & Rodrigo, R. 1996, *J. Geophys. Res.*, 101, 23261
- Leach, S., Vervloet, M., Desprès, A., et al. 1992, *Chem. Phys.*, 160, 451
- Linnartz, H., Bossa, J. B., Bouwman, J., et al. 2011, *Proceedings IAU symposium*, 280, 290
- Loison, J. C., Wakelam, V., Hickson, K. M., Bergeat, A., & Mereau, R. 2014, *Mon. Not R. Astron. Soc.*, 437, 930
- Lu, Q. & Sanche, L. 2001, *Phys. Rev. B*, 63, 153403
- Mallocci, G., Mulas, G., Cappellini, G., Fiorentini, V., & Porceddu, I. 2005, *A&A*, 432, 585
- Malyk, S., Kumi, G., Reisler, H., & Wittig, C. 2007, *J. Phys. Chem. A*, 111, 13565
- Marsalek, O., Elles, C. G., Pieniasek, P., & et al. 2011, *J. Chem. Phys.*, 135, 224510
- Marzocchi, M. P., Bonadeo, H., & Taddei, G. 1970, *J. Chem. Phys.*, 53, 867
- Mason, N. J., Dawes, A., Holtom, P. D., et al. 2006, *Faraday Discuss.*, 133, 311
- Mathis, J. S., Mezger, P. G., & Panagia, N. 1983, *A&A*, 128, 212
- McCarroll, B. 1970, *Rev. Sci. Instrumentation*, 41, 279
- McCarthy, M. C., Gottlieb, C. A., Gupta, H., & Thaddeus, P. 2006, *ApJ*, 652, 141
- Mennella, V., Baratta, G. A., Esposito, A., Ferini, G., & Pendleton, Y. J. 2003, *ApJ*, 587, 727
- Milligan, E., Jacox, M. E., & Abouaf-Marguin, L. 1967, *J. Chem. Phys.*, 46, 4562
- Modica, P. & Palumbo, M. E. 2010, *A&A*, 519, 22
- Moon, E., Kang, H., Oba, Y., Watanabe, N., & Kouchi, A. 2010, *ApJ*, 713, 906
- Muñoz-Caro, G. M., Dartois, E., Boduch, P., et al. 2014, *A&A*, 566, 93

- Muñoz-Caro, G. M., Jiménez-Escobar, A., Martín-Gago, J., et al. 2010, *A&A*, 522, 108
- Muñoz-Caro, G. M., Meierhenrich, U. J., Schutte, W. A., et al. 2002, *Nature*, 416, 403
- Muñoz-Caro, G. M. & Schutte, W. A. 2003, *A&A*, 412, 121
- Mumma, M. J., DiSanti, M. A., Dello Russo, N., et al. 2003, *Adv. Sp. Res.*, 31, 2563
- Novakovskaya, Y. V. & Stepanov, N. F. 2004, *Structural Chem.*, 15, 65
- Novozamsky, J. H., Schutte, W. A., & Keane, J. V. 2001, *A&A*, 379, 588
- Nuevo, M., Auger, C., Blanot, D., & d'Hendecourt, L. 2008, *Origin of life and evolution of the biosphere*, 38, 37
- Nuevo, M., Meierhenrich, U. J., d'Hendecourt, L., et al. 2007, *Adv. in Sp. Res.*, 39, 400
- Öberg, K. I., Boogert, A. C. A., Pontoppidan, K. M., et al. 2011, *ApJ*, 740, 109
- Öberg, K. I., Garrod, R. T., van Dishoeck, E. F., & Linnartz, H. 2009, *A&A*, 504, 891
- Öberg, K. I., van Dishoeck, E. F., Linnartz, H., & Andersson, S. 2010, *ApJ*, 718, 832
- Okabe, H. 1975, *J. Chem. Phys.*, 65, 2782
- Okabe, H. 1978, *Photochemistry of Small Molecules* (New York: Wiley-Interscience)
- Orlandi, G. & Negri, F. 2002, *Photochem. Photobiol. Sci.*, 1, 289
- Palumbo, M. E., Baratta, G. A., Fulvio, D., et al. 2008a, *Journal of Physics: Conference series*, 101, 12002
- Palumbo, M. E., Leto, P., Siringo, C., & Trigilio, C. 2008b, *ApJ*, 685, 1033
- Park, J. & Woon, D. E. 2004a, *ApJ*, 601, 63
- Park, J. & Woon, D. E. 2004b, *J. Phys. Chem A*, 108, 6589
- Parker, D. S. N., Zhang, F., Kim, Y. S., et al. 2012, *Proc. Natl. Acad. Sci. U.S.A.*, 109, 53
- Pavlovich, V. & Shpilevsky, E. 2010, *J. Appl. Spectrosc.*, 77, 335
- Pellerin, S., Cormier, J. M., Richard, F., Musiol, K., & Chapelle, J. 1996, *J. Phys. D*, 29, 726
- Pontoppidan, K. M. 2004, PhD thesis (Leiden: Leiden university)
- Pontoppidan, K. M., van Dishoeck, E. F., & Dartois, E. 2004, *A&A*, 426, 925
- Prasad, S. S. & Tarafdar, S. P. 1983, *ApJ*, 267, 603
- Roberts, K. R. G., Smith, K. T., & Sarre, P. J. 2012, *Mon. Not. Royal Astron. Soc.*, 421, 3277

- Romanescu, C., Marschall, J., Kim, D., Khatiwada, A., & Kalogerakis, K. S. 2010, *Icarus*, 205, 695
- Romanzin, C., Ioppolo, S., Cuppen, H. M., van Dishoeck, E. F., & Linnartz, H. 2011, *J. Chem. Phys.*, 134, 084504
- Roser, J. E. & Allamandola, L. J. 2010, *ApJ*, 722, 1932
- Sakai, N., Sakai, T., Hirota, T., Burton, M., & Yamamoto, S. 2009, *ApJ*, 697, 769
- Sandford, S. A., Bernstein, M. P., & Allamandola, L. J. 2004, *ApJ*, 607, 346
- Sariciftci, N. S., Braun, D., Zhang, C., et al. 1993, *Appl. Phys. Lett.*, 62, 585
- Sassara, A., Zerza, G., & Chergui, M. 2002, *Phys. Chem. Comm.*, 28, 1
- Sassara, A., Zerza, G., Chergui, M., & Leach, S. 2001, *ApJs*, 135, 263
- Sceats, M. G. & Rice, S. A. 1983, *Water: A Comprehensive Treatise*, Vol. 7 edited by F. Franks (New York: Plenum)
- Schutte, W. A. & Greenberg, J. M. 1997, *A&A*, 317, 43
- Schutte, W. A. & Khanna, R. K. 2003, *A&A*, 398, 1049
- Sellgren, K., Brooke, T. Y., Smith, R. G., & Geballe, T. R. 1995, *ApJ*, 449, 69
- Sellgren, K., Uchida, K. I., & Werner, M. W. 2007, *ApJ*, 659, 1338
- Sellgren, K., Werner, M. W., Ingalls, J. G., et al. 2010, *ApJl*, 722, 54
- Shida, T. 1988, *Electronic Absorption Spectra of Radical Ions* (Amsterdam: Elsevier)
- Shindo, F., Bénilan, Y., Chaquin, P., et al. 2001, *J. Mol. Sp.*, 210, 191
- Shindo, F., Bénilan, Y., Guillemin, J.-C., et al. 2003, *Planet. Space Sci.*, 51, 9
- Simon, F., Peterlik, H., Pfeiffer, R., Bernardi, J., & Kuzmany, J. 2007, *Chem. Phys. Lett.*, 445, 288
- Smith, N. S., Gazeau, M. C., Khlifi, A., & Raulin, F. 1998, *Planet. Space Sci.*, 47, 3
- Snow, T. P. & Witt, A. N. 1995, *Science*, 271, 1455
- Sonnentrucker, P., González-Alfonso, E., & Neufeld, D. A. 2007, *ApJ*, 671, 37
- Šoustek, P., Michl, M., Almonasy, N., et al. 2008, *Dyes and Pigments*, 78, 139
- Steglich, M., Bouwman, J., Huisken, F., & Henning, T. 2011, *ApJ*, 742, 2
- Steglich, M., Carpentier, Y., Jäger, C., et al. 2012, *A&A*, 540, 110

- Strazzulla, G., Baratta, G. A., Domingo, M., & Satorre, M. A. 2002, *Nuclear Instruments and Methods in Physics Research Section B*, 191, 714
- Swings, P. & Rosenfeld, L. 1937, *ApJ*, 86, 483
- Teolis, B. D., Famá, M., & Bargiola, R. A. 2007, *J. Chem. Phys.*, 127, 074507
- Tielens, A. G. G. M. 2008, *Annu. Rev. Astron. Astrophys.*, 46, 289
- Tielens, A. G. G. M. 2013, *Rev. Mod. Phys.*, 85, 1021
- Tielens, A. G. G. M. & Hagen, W. 1982, *A&A*, 114, 245
- Trumpler, R. J. 1930, *Lick observatory bulletin*, 420, 154
- van Dishoeck, E. F. 2008, *IAU Symposium*, 251, 1
- van Dishoeck, E. F., Jonkheid, B., & van Hemert, M. 2006, *Faraday Disc.*, 133, 231
- Verlet, J. R. R., Bragg, A. E., Kammrath, A., Cheshnovsky, O., & Neumark, D. M. 2005, *Science*, 307, 93
- Visser, R. 2009, PhD thesis (Leiden: Leiden university)
- Wakelam, V., Smith, I. W. M., Herbst, E., et al. 2010, *Sp. Sc. Rev.*, 156, 13
- Wang, B. C., Chang, J. C., Tso, H. C., Hsu, H. F., & Cheng, C. Y. 2003, *J. Mol. Struct.*, 629, 11
- Warneck, P. 1962, *Applied Optics*, 1, 721
- Watanabe, N. & Kouchi, A. 2002, *ApJ*, 567, 651
- Weber, P. & Greenberg, J. M. 1985, *Nature*, 316, 403
- Werner, M. W., Uchida, K. I., Sellgren, K., et al. 2004, *ApJs*, 154, 309
- Westley, M. S., Bargiola, R. A., Johnson, R. E., & Baratta, G. A. 1995, *Planet. Sp. Sci.*, 43, 1311
- Wickham-Jones, C., Ervin, K., Ellison, G., & Lineberger, W. 1989, *J. Chem. Phys.*, 91, 2762
- Williams, T. R. 2002, *BAAS*, 34, 1362
- Wong, M. H., Bjoraker, G. L., Smith, M. D., Flasar, F. M., & Nixon, C. A. 2004, *Planet. Space Sci.*, 52, 385
- Woon, D. E. 2004, *Adv. Sp. Res.*, 33, 44
- Woon, D. E. 2006, *AIP Conf. Proc.*, 855, 305

Woon, D. E. & Park, J. 2004, *ApJ*, 607, 342

Wu, C. Y. R., Chen, F. Z., & Judge, D. L. 2001, *J. Geophys. Res.*, 106, 7629

Wu, C. Y. R. & Cheng, B. M. 2008, *Chem. Phys. Lett.*, 461, 53

Wu, C. Y. R., Judge, D. L., Cheng, B. M., et al. 2002, *Icarus*, 156, 456

Zhou, L., Kaiser, R., & Tokunaga, A. T. 2009, *Planet. Space Sci.*, 57, 830

Zhou, L., Zheng, W., Kaiser, R., et al. 2010, *ApJ*, 718, 1243

Samenvatting

Koolstof in het universum

Bij het ontstaan van het universum, kort na de big bang, was het universum bijzonder heet. Zo heet dat materie niet bestond. Dankzij de hierop volgende uitzetting van het universum daalde de temperatuur heel snel waardoor na ongeveer 3 minuten de eerste atoomkernen (zonder electronenwolk) verschenen. Deze eerste atomen waren de vier lichtste elementen van het periodiek systeem: waterstof, helium en een kleine hoeveelheid lithium en beryllium. De zwaardere elementen van het universum, zoals we dat tegenwoordig kennen, verschenen pas nadat ze in de eerste sterren werden gevormd en vervolgens aan het eind van hun leven uitgestoten werden.

Dit proefschrift focust op koolstof, na waterstof, zuurstof en helium het meest voorkomende element in het universum. In combinatie met de specifieke chemische eigenschappen waarbij koolstof vier verschillende atomaire verbindingen aan kan gaan is te verwachten dat koolstof een centrale chemische rol speelt in het universum.

Dit reflecteert zich in de tabel van moleculen die ontdekt zijn in de ruimte, vooral in het interstellaire en circumstellaire medium. Van deze 185 moleculen bevatten er 137 koolstof. Alle moleculen in deze lijst bestaande uit zes of meer atomen bevatten één of meerdere koolstofatomen. Hiernaast zijn vele koolstofdragende moleculen ontdekt als klasse, en zijn dus niet in de lijst van 185 moleculen opgenomen. Hierdoor komen in het universum zowel aromatische (bijvoorbeeld polycyclische aromatische koolwaterstoffen en fullerenen) als alifatische (bijvoorbeeld polyynes, cyanopolyynes en alkanen) moleculen voor.

Interstellair ijs

Interstellair ijs komt voor in koude gebieden van het universum waar vluchtige moleculen vast vriezen op kleine stofdeeltjes. Het betreft hier vooral stofwolken die door hun hogere dichtheid niet transparant zijn voor externe energetische straling. Dit zorgt ervoor dat de temperaturen van de stofdeeltjes kunnen zakken tot onder 150 K en een ijslaag zich kan vormen. Deze ijslaag bestaat vooral uit kleine moleculen zoals H_2O , CO , CO_2 , CH_4 , CH_3OH en NH_3 . Echter, het is de verwachting dat grotere, koolstofdragende, moleculen, waarvan gekend is dat deze aanwezig zijn in deze stofwolken, ook onderdeel worden van het ijs. Hierdoor ontstaat er een chemisch reservoir van moleculen die doordat ze dicht bij elkaar zitten onder invloed van een externe energiebron een rijke chemie kunnen ondergaan. In dit proefschrift wordt onderzoek verricht naar chemische reacties van koolstofhoudende moleculen die zich in ijs bevinden. Als energiebron voor deze reacties wordt gebruik gemaakt van een UV lichtbron die het interstellaire stralingsveld nabootst.

Moleculaire spectroscopie

Overgangen tussen energietoestanden van de atomen en moleculen gaan vaak gepaard met het absorberen of uitstralen van een foton met de specifieke energie (of golflengte) van deze overgang. Waarnemingen van deze overgangen, zowel in absorptie als in emissie is de bron van onze kennis van de chemische samenstelling van het universum. Hierbij zijn verschillende typen overgangen waarneembaar in verschillende gebieden van het elektromagnetisch spectrum.

- De overgang tussen twee rotatietoestanden van een molecule resulteert in fotonen met de laagste energie. In het elektromagnetisch spectrum vallen deze overgangen in het radiogebied. Omdat in de vaste fase de moleculen vast zitten in een matrix zijn deze waarnemingen enkel mogelijk bij gas fase moleculen. In een spectrum zijn deze overgangen bijzonder talrijk, scherp en temperatuursafhankelijk.
- De chemische verbindingen tussen de atomen in een molecule gedragen zich als een massa-veer systeem. De overgang tussen verschillende trillingstoestanden resulteren in fotonen in het infrarood gebied van het elektromagnetisch spectrum. Dit is de meest gebruikte methode om ijs waar te nemen. Echter, bij moleculen met gelijkaardige structuur kunnen overgangen sterk overlappen waardoor identificatie onmogelijk is.
- De overgangen van elektronen tussen verschillende energieniveaus vallen in het zichtbare en het UV gedeelte van het elektromagnetisch spectrum. Deze overgangen zijn heel sterk en molecule-specifiek. Hierdoor is het makkelijker om moleculen te identificeren, echter, wanneer meerdere gelijkaardige moleculen in de matrix aanwezig zijn kan (gedeeltelijke) overlap voorkomen. In deze thesis wordt het meest gebruik gemaakt van deze laatste methode.

Het laboratorium

In het laboratorium worden de omstandigheden van het universum zo goed mogelijk nagebootst. Het doel is om op deze manier chemische en fysische processen te bestuderen zoals ze gebeuren in het universum. Specifieke omstandigheden in het universum zijn quasi-vacuüm, lage (cryogene) temperaturen tot 5 K, sterke UV straling enz. In deze studie wordt hoofdzakelijk gebruik gemaakt van OASIS (zie hoofdstuk 2). In deze opstelling wordt het interstellaire ijs gevormd bestaande uit een matrix en koolstofdragende moleculen (acetyleen, C_{60} en PAKs). Een eerste resultaat is het meten van de spectra van deze moleculen. Hierdoor hebben waarnemers de noodzakelijke informatie om deze moleculen te identificeren. In deze thesis is een analyse van het spectrum van C_{60} in een water matrix opgenomen (hoofdstuk 4).

Vervolgens wordt dit ijs belicht met UV straling zoals deze in interstellaire stofwolken voor komt en de resulterende chemische reacties worden gevolgd. Hierbij dienen alle fysische parameters gemeten te worden. Tijdens het onderzoek werd duidelijk dat dit voor de lamp die de UV straling produceert niet het geval was. Hiervoor is een oplossing gevonden door gebruik te maken van het fotoëlectrisch (zie hoofdstuk 3). Het vervolg van deze thesis bestaat uit een onderzoek naar chemische processen van koolstofdragende moleculen in een interstellar ijs.

PAKs in ijs

Wanneer een PAK in een waterijs matrix opgesloten wordt zal deze specifieke omgeving ervoor zorgen dat wanneer dit ijs belicht wordt met UV fotonen de PAKs geïoniseerd worden tot kationen. In hoofdstuk 5 wordt dieper in gegaan op deze matrix omgeving. Door het water te vervangen door ammoniak (NH_3) wordt de eerder beschreven fotoïonisatie omgekeerd. In plaats van een electron af te staan aan de matrix zal de PAK molecule een electron absorberen uit de matrix. Wanneer een mengsel van water en ammoniak gemaakt wordt zal naargelang de concentratie er een overgang ontstaan van kationisatie naar anionisatie. Bij een 1:1 verhouding van ammoniak en water worden zowel kationen en anionen gelijktijdig waargenomen.

In hoofdstuk 6 wordt in gegaan op de invloed van de PAH concentratie op zowel de spectroscopie van PAKs in water ijs als op de fotochemie. Wanneer de concentratie een punt bereikt waarbij de PAK moleculen clusters beginnen te vormen in het ijs zal het spectrum een duidelijke verbreding en roodverschuiving vertonen ten opzichte van het geïsoleerde spectrum. Hiernaast zal deze verhoogde concentratie ook een negatief effect hebben op de vorming van kationen onder UV straling. Hiermee wordt het mogelijk om te vergelijken tussen experimenten die gebruik maken van zichtbaar-UV spectroscopie en IR spectroscopie.

De rol van acetyleen in ijs

Tenslotte wordt in hoofdstuk 7 dieper in gegaan op de rol die acetyleen (C_2H_2) speelt in een interstellair ijs. Dankzij de unieke combinatie van zichtbaar-UV en IR spectroscopie wordt de volledige fotochemie van acetyleen in de vaste fase ontleed. Deze chemie bestaat hoofdzakelijk uit polymerisatie met vorming van enkele interessante nevenproducten. Deze chemische processen blijken goed stand te houden wanneer acetyleen gemengd wordt met water ondanks dat er enkele competitieve processen de kop op steken. Het onderzoek laat zien dat vaste stof reacties van acetyleen kunnen bijdragen aan de vorming van moleculen die in de gas fase waargenomen zijn.

Conclusie

Het astronomische belang van het onderzoek dat in dit proefschrift wordt beschreven kan in twee punten worden samengevat.

- In dit proefschrift worden vaste stof spectra van relevante moleculen gemeten en beschreven. Deze informatie is belangrijk bij het detecteren van deze moleculen in waargenomen spectra.
- Het chemisch gedrag van deze moleculen na bestraling met UV licht is onderzocht. Tegenwoordige modellen gaan vooral uit van gas fase reacties voor de vorming van deze moleculen, in dit proefschrift voegen we vaste stof reacties toe waardoor we nieuwe informatie aanbieden voor astronomische waarnemingen van interstellair ijs.

Curriculum vitae

Op 27 januari 1983 ben ik geboren in Oostende aan de Belgische kust. Aldaar ben ik opgegroeid en naar de secundaire school geweest in het Sint Lutgardisinstituut van 1995 tot 2001. Mijn interesse in wetenschap en techniek kwam al vroeg tot uiting in de drang om apparaten en machines die ik tegen kwam thuis na te maken en om defecte apparaten uit elkaar te vijzen en te onderzoeken. Met deze ruime wetenschappelijke en technische interesse ben ik in 1997 de plaatselijke sterrenkundige jongerenvereniging (JVS Quasar) binnen gestapt. Kort hierna wist ik zeker dat ik luchtvaart- en ruimtevaarttechniek wou studeren aan de TU Delft. Na mijn afstuderen aan het Sint Lutgardis met een ASO diploma wetenschappen-wiskunde in 2001 ben ik dan ook naar Delft getrokken om me daar verder te verdiepen in mijn interesse voor wetenschap en technologie. Hier ging een nieuwe wereld voor me open en al spoedig maakte ik de keuze om me te specialiseren in mechatronica en satellitsystemen. Ondertussen was ik toegetreten tot het bestuur van JVS Quasar waar ik me in verschillende bestuursfuncties bekommerde om het reilen en zeilen van de vereniging. Ondanks dat ik tijdens mijn studies met mijn neus altijd tussen de boeken zat was het praktische gedeelte van de sterrenkunde mij ook niet vreemd. Van 2000 tot 2006 was ik Waarnemingscoördinator van de vereniging (ook wel WC genoemd) wat erop neer komt dat ik een van de actiefste waarnemers in de vereniging was. In die tijd had ik een telescoop met een opening van 15cm wat mij de mogelijkheid gaf om mij vele avonden te vergapen aan de pracht van de sterrenhemel.

Tijdens mijn master kreeg ik de kans om voor het eerst aan een echt instrument te werken bij TNO TPD in Delft. Hier was ik verantwoordelijk voor het ontwikkelen van een technologie demonstrator voor een metrologie systeem voor het meten van 5 vrijheidsgraden voor formatievliegen van satellieten. In 2007 resulteerde dit in de bouw en het testen van de demonstrator wat mij mijn ingenieursdiploma in de luchtvaart- en ruimtevaarttechniek met specialisatie in ruimtevaartinstrumentatie opleverde.

Met dit diploma op zak ging ik direct hierna aan de slag bij Verhaert space waar ik verantwoordelijk was voor de warmtehuishouding van de systemen en satellieten die daar gebouwd werden. Hier was ik betrokken bij de bouw van 3 satellieten (Proba 2, Proba 3 en Proba V), en talloze instrumenten voor satellieten en het internationaal ruimtestation. Ondanks dat ik enkel verantwoordelijk was voor de technische kant van deze instrumenten had ik altijd interesse voor het wetenschappelijke aspect.

In 2010 heb ik dan de overstap gemaakt van de industrie naar de academische wereld. In de 4 hierop volgende jaren heb ik onderzoek verricht naar fotochemie van interstellair ijs bij het Sackler laboratorium van de universiteit Leiden. In het voorjaar van 2015 volgt dan ook het afleggen van dit doctoraat.

Nawoord

Van deze laatste pagina's had ik graag gebruik gemaakt om een wandeling te maken door mijn eigen leven en mijn dank te betuigen aan de mensen die voor mij een belangrijke positieve invloed gehad hebben.

De eerste mensen die ik leerde kennen kort na mijn geboorte is natuurlijk mijn naaste familie. Ik ben mijn ouders dankbaar voor het leven dat ze mij geschonken hebben. Onmiddellijk na mijn geboorte maakte ik kennis met mijn broer, Stijn. Door de broederlijke competitie hebben we constant elkaar verder gepusht, bedankt daarvoor dus. Vervolgens ben ik ook mijn dankbaarheid verschuldigd aan Hendrik Boeraeve, die mij niet alleen een deel van mijn naam gegeven heeft (de H.), maar ook door zijn eigen nieuwsgierigheid naar de natuur rond ons mij voor het eerst laten zien dat nieuwsgierigheid goed is. Met deze nieuwsgierigheid heb ik altijd een interesse gehad voor wetenschap en techniek.

Het ontwikkelen hiervan is in een stroomversnelling gekomen toen ik Patrick Jacques leerde kennen. Hij heeft me in 1997 geïntroduceerd bij JVS Quasar, de plaatselijke sterrenkundige jongerenvereniging. Door de jaren heen is hij een goede vriend geworden en vandaag hebben we maar een paar woorden nodig om elkaar te verstaan. In JVS Quasar stimuleerden de leden elkaar op sterrenkundig vlak (en ook op andere vlakken), ik zal hier even de die-hards uit deze periode opnoemen: Ken Boedt, Chris Coulier, Wouter Deconinck, Kurt Dequick, Dieter Jansoone, Martijn Lammaing, Mike Rosseel, Stijn Vanderheiden, Bartje Vandewalle, Anja Vanleenhove, Louis Vercamer en Hans Yperman.

Tijdens deze periode besliste ik al heel snel dat ik van wetenschap en techniek mijn leven wilde maken, hierdoor trok in in 2001 naar Delft waar ik mij specialiseerde in ruimtevaartinstrumentatie. Na mijn studie af te ronden deed ik de overstap van de jongeren van JVS Quasar naar de volwassenen van de Astro Event Group, waar veel van de eerdergenoemde Quasarianen ook lid zijn. Hier heb ik in het bijzonder geleerd van Alex Degroote wat gouden handen zijn en waarom dat zo belangrijk is. Daarnaast heb ik van 'meestre' Schuyesmans geleerd wat een kinderlijke benieuwdheid is en dat je dat na je 50^{ste} nog altijd kunt hebben. Van hen heb ik ook geleerd dat een aantal dingen waar ik mee bezig ben niet zo evident zijn voor de niet-technen.

In dezelfde periode begon ik te werken bij Verhaert space, waar ik de meest bijzondere stimulans heb leren kennen, het betreft hier Chunman Fan met wie ik ondertussen getrouwd ben. Bedankt om me te leren de lat hoger te leggen (en er ook over te springen). In 2010 ben ik in het Sackler lab begonnen met mijn doctoraat, als onderdeel van het LASSIE ITN. Deze internationale omgeving van debat en ideeën heeft mij gebracht naar het punt waar ik nu ben. Alle Sackler en LASSIE-collega's opnoemen zou iets te ver reiken, maar toch hier nog enkele speciale vermeldingen met collega's waar ik bijzonder nauw mee samen gewerkt heb. Zij hebben mij een bijzonder duwtje in de rug gegeven.

De eerste personen die ik leerde kennen zijn Jordy Bouwman en Emily Tenenbaum. Jordy bouwde de uitstekende OASIS opstelling, waarvoor dank. Emily is een bijzonder aardige dame die me de kneepjes van de opstelling leerde kennen en jammergenoeg veel te vroeg de overstap naar de 'dark side' (de industrie) gemaakt heeft. In het lab liep toen Joseph Guss rond die een bijzonder mooie opstelling bouwde. Het is niet verwonderlijk dat hij later les is gaan geven, want ik heb door de discussies met hem veel geleerd. Daarnaast kon ik voor technische problemen altijd terecht bij de mensen van de werkplaats, die dankzij hun pragmatische aanpak menig probleem in een handomdraai opgelost hebben.

Na een eerste omzwerping op de 4^{de} verdieping van het Huyghens gebouw ben ik na een aantal maanden verhuisd naar kamer HL502 die ik al snel deelde met Gleb Fedoseev, en later ook met mede-Sacklers Niels ligterink en Ko-Ju Chuang. Alle drie hebben ze op hun eigen manier mijn verblijf aangenamer gemaakt. Gleb door de vele discussies die door zijn vaak tegendraadse meningen mooi gekruid werden (en worden). Nils en KoJu zijn de meest aangename bureaugenoten die je je kunt inbeelden en ik wens hen bij deze veel succes voor de komende jaren.

Een doctoraat is geen doctoraat zonder frustratie en donkere momenten. In deze momenten kon ik altijd terecht bij 'nonkel' Xander Tielens voor goede raad en bij Lou Allamandola voor enkele nieuwe inzichten en peptalk.

Het Sackler laboratorium is een internationaal gezelschap waar verschillende talen gesproken worden. Het was voor mij een mooie tijd om mijn talenkennis op peil te houden, en ik heb hier vooral oefening gehad in de taal van Molière door met Edith Fayolle en Jean-Baptiste Bossa te praten.

Een laatste Sackler die ik hier niet mag vergeten en waarvan ik de deskundigheid bijzonder heb leren appreciëren tijdens mijn laatste jaar in het lab is Dongfeng Zhao, die altijd wel een idee heeft om een piekje in het spectrum te verklaren. Een onderdeel van LASSIE is het uitwisselen van ideeën tussen de verschillende deelnemende universiteiten. In het kader hiervan had ik een bijzonder aangename samenwerking met John Thrower die als super post-doc een maand in Leiden was. Daarnaast hebben we ook bezoek gehad van Ewelyna Szymanska voor wie ik veel respect gekregen heb.

Ik heb zelf mooie herinneringen aan mijn tijd in Jena waar ik op bezoek kwam bij mede LASSIE Tolou Sabri. Dankzij het betere lab.- en denkwerk met Abel Brieva en Daniele Fulvio is daar een mooie publicatie uitgekomen. De discussies met Gaël Rouillé over PAH's en C₂H₂ waren voor mij bijzonder verfrissend. Tenslotte wens ik de mensen die mijn werk verder zetten, Paul en Vincent nog veel succes voor hun verdere carrière.

